ACADEMIC RESEARCH & REVIEWS IN ENGINEERING

EDITOR
ASSOC. PROF. DR. SELAHATTİN BARDAK

SERÜVEN

Genel Yayın Yönetmeni / Editor in Chief • C. Cansın Selin Temana
Kapak & İç Tasarım / Cover & Interior Design • Serüven Yayınevi
Birinci Basım / First Edition • © Aralık 2021
ISBN • 978-625-7721-50-9

Serüven Yayınevi / Serüven Publishing
Türkiye Adres / Turkey Address: Yalı Mahallesi İstikbal Caddesi No:6 Güzelbahçe / İZMİR
Telefon / Phone: 05437675765
web: www.seruvenyayinevi.com
e-mail: seruvenyayinevi@gmail.com

Baskı & Cilt / Printing & Volume
Sertifika / Certificate No: 47083

ACADEMIC RESEARCH & REVIEWS IN ENGINEERING

Editör

Assoc. Prof. Dr. Selahattin BARDAK

CONTENTS

Chapter 1

UTILIZATION OF POWER PLANT WASTE HEAT IN BIOGAS BASED ELECTRICITY PRODUCTION FOR ÇANAKKALE

Can COSKUN[1]
Zuhal OKTAY[2]
Bahadır BİRECİKLİ[3]

1 Izmir Democracy University, Department of Mechanical Engineering, Izmir, Turkey, can.coskun@idu.edu.tr, https://orcid.org/0000-0003-4100-0296
2 Izmir Democracy University, Department of Mechanical Engineering, Izmir, Turkey, zuhal.oktay@idu.edu.tr, https://orcid.org/0000-0001-6167-7048
3 Batman Üniversitesi, Vocational School of Technical Sciences, Electricity and Energy Department, Natural Gas and Installation Technology Program, Bahadir. Birecikli@batman.edu.tr, ORCID:0000-0002-6765-0097

1. INTRODUCTION

The rate of meeting the primary energy supply with domestic production in Turkey was 26% in 2016. In other words, Turkey's foreign dependency in energy is at the level of 74%. The foreign dependency ratio has increased significantly, especially since the beginning of the 1990s, due to the great increase in natural gas consumption. The foreign dependency ratio has started to hover around 70% since the beginning of the 2000s. Nearly half of the electricity production in 2016 was met from natural gas and imported coal. The use of natural gas and coal, in addition to the problems it creates in terms of climate change, causes an economy dependent on neighboring countries. Therefore, in order to get rid of this dependence, it is necessary to turn to domestic and renewable energy sources. Although there has been an increase in the use of renewable energy sources in recent years, it is seen that the rate of use is still at a low level. It will be possible to contribute to the reduction of foreign dependency of the country's economy by making more use of renewable energy sources in order to meet the energy needs (Eleventh Development Plan Energy Supply Security and Efficiency Specialization Commission Report, 2019).

According to the European Biogas Association, the top three countries in biogas production in EU countries are Germany, France and Switzerland, respectively. On the other hand, the world ranking is China, India and Nepal. The biomass waste potential in Turkey is estimated to be approximately 8.6 million tons of petroleum equivalent (MTEP). The amount of biogas that can be produced from biomass waste is considered to be 1.5-2 MTEP. Among the main sources of biomass, there are animal biomass sources, which are defined as the feces of animals such as cattle, sheep, chickens, slaughterhouse wastes and wastes generated during the processing of animal products. By using the biogas potential in Turkey, 2.5-4.8% of Turkey's primary energy need can be met. If the biogas potential in Turkey can be used, natural gas consumption can be reduced by 19.2-37%. If the electricity efficiency is accepted as 40% for biogas facilities, 6% to 12% of Turkey's electrical energy can be obtained from biogas (Ministry of Energy and Natural Resources).

Waste heat can be used for industrial drying, cooling, heating, fermentation, balneological use, distillation and desalination processes, depending on the temperature values. Also, different combinations of these usage methods can be applied. There are many studies available in the literature about waste heat utilization in different perspectives. Oğulata (Oğulata, R. T., 2004) analyzed heat recovery systems using it for the drying process. The variation of fresh air mass, recuperator temperature, heater capacity and recuperator efficiency with dryer-inlet air temperature

has been demonstrated in detail. Tay et al. (Tay et. al.,1996) investigeted the vacuum desalination by using waste heat. A prototype study was conducted in the laboratory to explore the feasibility of using a vacuum desalination process using waste heat from the steam power cycle. It was demonstrated in experiments that water boils at 40-90°C at a corresponding vacuum pressure of 0.1-0.7 bar, respectively. El-Din (El-Din, 1999) analzed optimum utilization condutions of heat engines waste heat. The optimum heat transferred in the system and the optimum heat pump / heat engine operating ratio have been analyzed for heat pumps. Romero and Rodríguez-Martínez (Romero and Rodríguez-Martínez, 2008) showed the wasted heat based rational energy saving amount. The process of water purification from waste heat was described with a mathematical model. Optimal operating conditions were determined for different processes that generate waste heat at low temperatures and require water treatment.

On the other hand, there is limited research (Cohen et al.,2003; Maidment et al., 2006) in literature on utilization of power plant condenser waste heat. Limited application area is available for utilization of power plant condenser waste heat as a result of low temperatures (35-45 °C). One of economical and practical options are given as swimming pool heating, fish farm heating, greenhouse heating, fermentation and distillation units. Also, low temperature amounts can be upgraded to 60 °C by utilizing heat pump system. Then, this energy can be used for district heating systems.

Biogas is one of the important renewable energy sources. The production of biogas can be achieved by using the countries' own potential resources. Different methods, aerobic and anaerobic, are used for the production of biogas from industrial and agricultural wastes (Xinshan et al., 2005). Anaerobic biogas production process has the advantages of lower sludge production, low energy requirement and low initial investment cost for the operation compared to conventional aerobic processes (Kim et al., 2006). The process of obtaining biogas using anaerobic digestion processes is a very good alternative among renewable energy sources (Bouallagui et al., 2003). Turkey has a very good potential for biogas production from agricultural and industrial wastes. However, there are difficulties in using these resources economically and fully (Ulusoy et al., 2009).

In this study, integration of fermentation system to power plant condenser unit for biogas and biogas based electricity is investigated. Also, overall system energy improvement is analyzed.

2. OVERVİEW OF CAN THERMAL POWER PLANT (CTPP)

Can Thermal Power Plant is located in the province of Çanakkale, in the northwest of Turkey and has been in operation since 2005 for electricity generation. It is 12 km away from the Can town. Fluidized bed coal-fired burning system is utilized in the system. Energy input and produced

electricity equal to 410 and 160 MW, respectively. Produced electricity equals to 39% of total input energy. Waste heat from condenser amounts to 195 MW (47% of total input energy) (Oktay, 2009). Energy flow diagram of CTPP is given in Fig. 1.

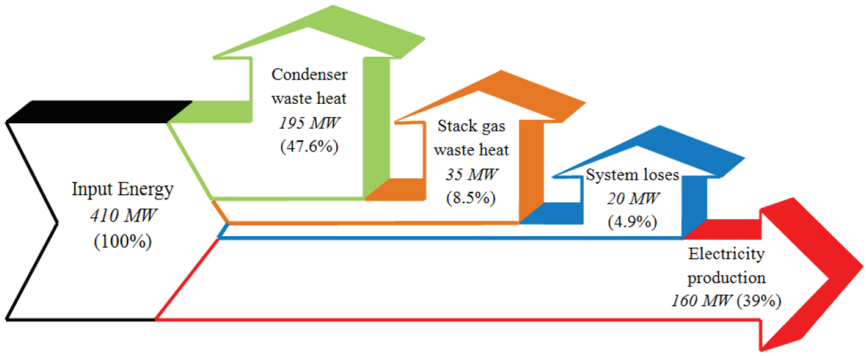

Fig. 1. Energy flow diagram of CTPP

2.1.Waste Heat Potential

Waste heat is released from condenser and chimney in power plants. There is two main parts in power plants for waste heat recovery potential. Waste heat recovery potential for two components is explained below.

2.1.1. Waste Heat from Condenser Unit

Condenser units are utilized in system for condensing steam. Generally, released energy to atmosphere during the condensation process is higher than produced electricity in power plants. High amount of energy is released or absorbed during condensation and evaporation. In CTPP, 195 MW waste heat is rejected to atmosphere with 1.7 °C water temperature difference. Steam leaves the low pressure turbine at 43.4 °C and 0.915 quality. Then, it enters the condenser unit under the vacuum pressure at 8.5 kPa. Condensed water leaves from the condenser unit at 42.7 °C. Released energy equals to 122% of produced electricity.

2.1.2. Waste Heat from Stack Gas

It is known that stack gas temperature is naturally higher than condenser unit. But released energy from chimney is generally lower than condenser unit. The energy released from chimney is about 17% of the energy released from condenser unit in CTPP. There are some limitations for decreasing the stack gas temperature leaving from chimney. First limitation is stack draught. Temperature difference between outdoor and stack gas generates stack draught. If stack gas temperature is reduced, additional fan units

should be constructed to supply enough stack draught. Additional fan units generate incremental cost for both electricity consumption and investment cost. Second limitation is the condensation of corrosive gas like H_2S in the chimney. Condensation of corrosive gas in the chimney causes corrosion, which is a very undesirable situation. So, stack gas temperature is generally higher than 100 °C for coal-fired power plants. New chimney should be constructed before the stack gas temperature decreases. Additional chimney will generate incremental cost, too.

3. THERMODYNAMIC ANALYSIS

The balance equations are stated for mass and energy for both steady-state and steady-flow systems and then applied to the GDHS. In this regard, the mass balance equation for the overall geothermal system can be written as follows:

$$\sum_{i=1}^{n} \dot{m}_{in} = \sum_{i=1}^{n} \dot{m}_{out} \quad (1)$$

The energy efficiency of the system is given as:

$$\eta = \frac{\dot{W}_{tot}}{\dot{E}_{in}} \quad (2)$$

where, denotes the total electricity production. is the energy input for overall system.

$$\dot{W}_{Tot.} = \dot{W}_{Biogas} + \dot{W}_{CTPP} \quad (3)$$

where, indicates biogas based electricty.

4. INTEGRATION OF BIOGAS BASED ELECTRICITY SYSTEM to CTPP

Biogas based electricity system is designed to be integrated in CTPP condenser unit. Waste heat recovery can be supplied from system condenser unit at 40 °C. 195 MW thermal energy can be transferred to fresh water in transmission network. Determination of fresh water input and output temperature to condenser unit is the most important point in system design. If temperature difference increases, required circulating mass flow rate decreases. Circulating mass flow rate directly affects both the required electrical energy for pumping fluid and system design dimensions. To decrease the required electrical energy and system design dimensions, leaving and achieving fluid temperature should be higher. For different operating conditions, required electricity is calculated and given in Fig. 2.

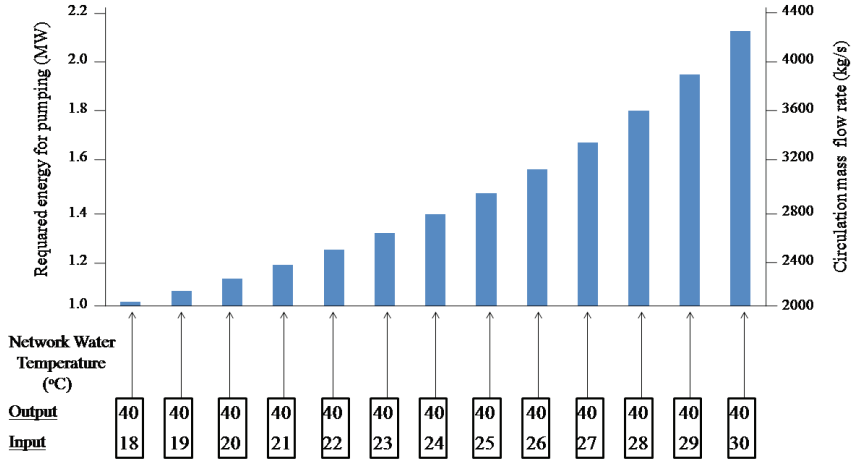

Fig. 2 Circulation mass flow rate and required pumping energy for different fresh water input and output temperature to condenser unit

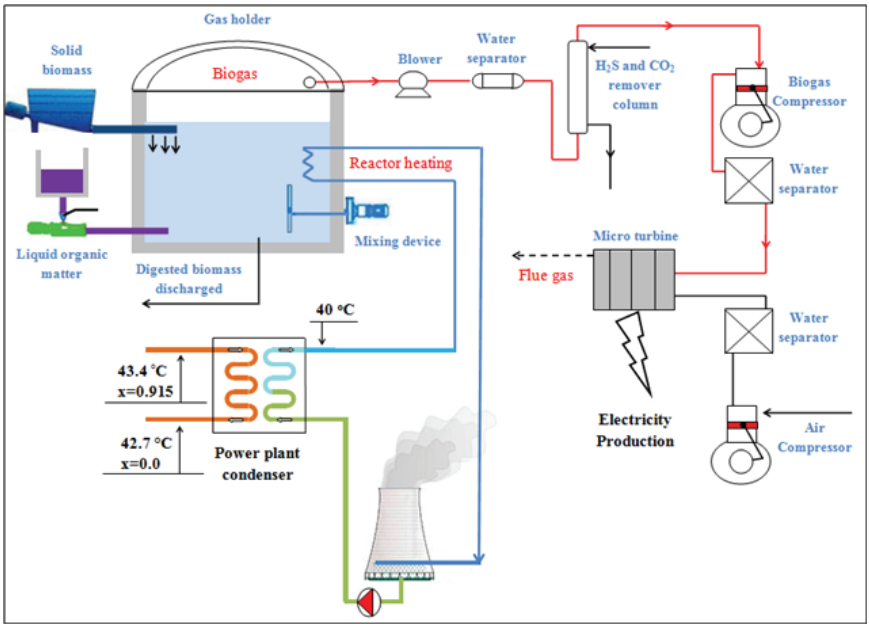

Fig. 3. Schematically demonstration of additional system

The components of the biogas power generation system are, respectively, the biogas reactor, the blower, the water separator unit, the H_2S and CO_2 removal column, the biogas and air compressor, and the micro-turbines. After the biogas is produced in the reactor, it is sent to the blower and water separator unit. Before the biogas is transferred to the

micro turbine, H_2S and CO_2 are sent to the reduction column. The biogas from the separator unit is then transferred to the micro turbines. After reduction of H_2S and CO_2, it is transported to the micro turbine to produce electricity. Schematically, demonstration of biogas based electricity system is given in Figure 3. Coskun et al. (Coskun et al., 2011) performed the energy analyses of hydrogen production with biogas-based electricity. Reference biogas reactor for calculation is taken from Ref. (Coskun et al., 2011) and its volume is accepted as 19600 m^3. The wall components of the reactor are presented in Table 1.

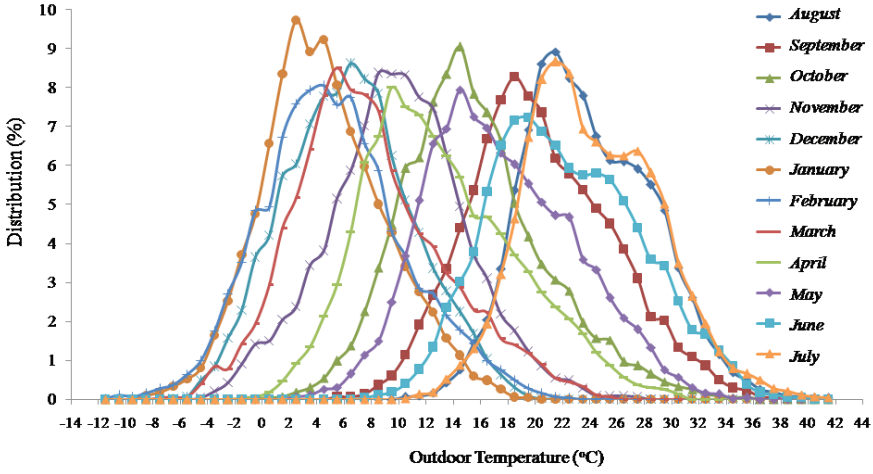

Fig. 4. Outdoor temperature distribution for region

The outdoor temperature distribution was calculated using the technique given in Ref. The outdoor temperature distribution of the region is presented in Figure 4. The reactor temperature is kept from 36 ºC in winter to 38 ºC in summer. The design temperature value for the region was accepted as -2.5 °C. Design heat lose is calculated as 636 kW for a sample biogas reactor and given in Table 1.

Table 1. Some properties for biogas reactor and design heating requirement for 35 °C base temperature

Reactor surface contact	Element type	Area (m^2)	U (W/m^2 °C)	UA (kW/°C)	Design temperature (°C)	Design heat lose (kW)
Air contact	15 cm concrete	3534	3.58	12.65	-2.5	474.4
Ground contact	15 cm concrete	1963	3.58	7.03	12	161.7
					Total	636.1

5. BIOGAS PRODUCTION POTENTIAL IN ÇANAKKALE

The biogas sector is the sector that produces electricity from methane gas, which is produced by fermenting animal and organic wastes in general, compost fertilizer and methane gas. This sector is also an important symbiosis facility, and it is a sector that transforms the wastes of food and livestock enterprises into products in an environmentally friendly manner. Biogas production efficiency and methane ratios from animal wastes are given in Table 2 (Ministry of Energy and Natural Resources). In Turkey, the most important and sustainable input in electricity generation from biogas is animal waste. 1 m^3 of biogas; It is equivalent to 0.62 liters of kerosene, 1.46 kg of charcoal, 3.47 kg of wood, 0.43 kg of butane gas and 4.70 kWh of electrical energy. In Çanakkale province, especially the existence of cattle is increasing rapidly. For Çanakkale, the farms are willing to give the wastes to the facilities for biogas production, but they want the dry manure produced after fermentation to be transported back to the farmers. Both small and large farms in the Çanakkale region are willing to collect waste on a weekly basis. In recent years, many biogas power plants have been put into operation in Turkey due to the increasing investments in livestock and the recovery of their wastes. There is a biogas based electricity facility in Çanakkale. The supports provided to the livestock sector, new large-scale livestock investments, the disposal of wastes generated in these facilities, the wastes of some food production facilities have made the raw material supply easily accessible in the sector. According to Çanakkale agricultural and livestock sectors investment guide, the number of cattle in livestock of Çanakkale is 216,833 (Table 3).

Table 2. Biogas production efficiency and methane ratios from animal wastes

	Biogas Efficiency (liter/kg)	Methane Ratio (% of volume)
Cattle Manure	90-310	65
Poultry Manure	310-620	60
Pig Manure	340-550	65-70

Table 3. Number of cattle and ovine in livestock of Çanakkale

Type	Number
Sheep (Native)	465.834
Sheep (Merino)	23.609
Hair Goat	226.106
Ovine TOTAL	715.876

Beef (Pure Culture)	182.160
Cattle (Cultural Cross)	19.544
Beef (Domestic)	14.601
Mandate	528
Cattle TOTAL	216.833

One of the important inputs of the sector is the intensive consumption of clean water for cooling and cleaning purposes. The biogas industry has two important problems. The first is that it is difficult to obtain technical staff who will work at the facility and have sufficient experience in biogas production. The second is that the plant equipment is imported. This situation brings with it maintenance, warranty, operation and repair problems. Here, the risk factor is the increase in the exchange rate and the fluctuation in the exchange rates, which have a significant impact on the feasibility studies of the investors.

The supports given to the Biogas Sector in Turkey can be grouped under three headings: a) Selling the generated electricity to the grid with a certain price guarantee, b) If the electricity produced is produced with renewable energy equipment, a certain price increase is given to the purchased electricity, c) In the sale of the electricity produced, if the machinery and equipment are domestic production, additional supports are given in kWh. The most important actor in the biogas sector in Turkey is the Energy Market Regulatory Authority. Operating under the Ministry of Energy and Natural Resources, the General Directorate of Renewable Energy operates as an authorized and regulatory agency.

6. RESULTS AND DİSCUSSİON

Walla and Schneeberger (Walla and Schneeberger, 2008) investigated the optimal size for biogas plants. They found the long-run average cost curve (per kWh) for biogas and electricity production in agricultural biogas plants (transport costs are not included) and given in Eq. (4).

$$c = 13.09 + \frac{3545700}{m} \tag{4}$$

where, c is cost in cents per kWh (not included transport). m is electricity production in kWh. Biogas and electricity production potential is calculated for 216,883 cattle manure and given in Table 2. 40 MW of potential biogas based electricity production is available. Total 17 micro turbines (2.425 MW*16+1 MW*1) are chosen by using data from Ref. (Walla and Schneeberger, 2008). Electricity production efficiency is 40.6% for 1001–2425 CHP system. Total cost of 40 MW biogas power plant is determined by using Eq.(1) and about 56 Millions € (excluding transportation cost).

Table 2. Average electricity production potential for Canakkale from cattle manure based biogas

Number of animals in livestock	-	216883
Average biogas production potential	(m^3/sec)	3.343
CH_4 rate in produced biogas	(%)	65
Electricity production efficiency	(%)	40.6
Average electricity production potential	MW	41.9
Number of micro turbines	-	17 (2.425 MWx16+1 MWx1)

Overall energy efficiency of electricity production can be increased by 7.32% and achieved up to 46.34% for CTPP. Economical feasibility and optimal size of biogas power plant should be investigated for such kind of applications. Transportation cost of cattle manure is a very important parameter for this investigation. Also, this parameter should be considered.

This analysis will be a very good example to recover the released high amount of waste heat with low temperature for many power plants. Motivation of authorities about huge size biogas based electricity production can be increased by designing such kind of applications.

7. CONCLUSIONS

In this paper, biogas reactor heating system using power plant waste heat as a heat source is conducted in the first time in literature. The feasibility of utilization of biogas for electricity and increase in efficiency of overall system electricity production are investigated. Can power plant in Çanakkale, Turkey is chosen for the investigation in this case study. Can power plant releases 195 MW thermal energy to air in condenser unit with relatively low temperature (43°C). Given temperature range is ideal for mesophilic bacteria growth in digestion process during the biogas production process. 39.8 MW biogas based electricity production potential is available for Can power plant condenser waste heat. Overall electricity production energy efficiency can be increased by 9.7%. This analysis will provide a very good example to recover the released high amount of waste heat with low temperature for many power plants. Motivation of authorities on huge capacity biogas based electricity production can be increased by designing such kind of applications

In Turkey, 70-80% of power plants are financed by foreign loans for investment cost. It is very difficult to make any change in the system before the repayment of loans. Subsequently, all costs and project changes in the construction of waste heat recovery system. Therefore, it is very difficult to supply heat from power plant condenser unit for running power plant. It

is also very difficult to stop system for any change in practice. So, waste heat supplied system can be applicable for new constructed power plants. Authorities should consider how to use waste heat in tender conditions. The entire power plant project should contain waste heat recovery systems. Authorities should be conditioned to, at least, 5% of condenser waste heat for suitable applications such as biogas reactor or greenhouse heating for new installed power plants. Best practical applications can be different from region to region. But suitable application areas can be found.

REFERENCES

Bouallagui, H., Cheikh, R.B., Marouani, L., Hamdi, M. (2003) *Mesophilic biogas production from fruit and vegetable waste in a tubular digester*, Bioresource Technology, 86:85-89

Cohen M., Ianovici I., Breschi D., (2003) *Power plant residual heat for seawater desalination*, Desalination 152:155-165

Coskun, C., Akyuz, E., Oktay, Z., Dincer, I. (2011) *Energy analysis of hydrogen production using biogas-based electricity*, International Journal of Hydrogen Energy doi:10.1016/j.ijhydene.2010.12.125

Coskun, C. (2010) *A novel approach to degree-hour calculation: indoor and outdoor reference temperature based degree-hour calculation*, Energy, 35:2455-60

Çanakkale Agricultural and Livestock sectors investment guide. https://www.gmka.gov.tr/dokumanlar/yayinlar/Canakkale-Agriculture-and-Animal-Husbandry-Investment-Guide.pdf

Eleventh Development Plan Energy Supply Security and Efficiency Specialization Commission Report, 2019. https://www.sbb.gov.tr/wp-content/uploads/2021/12/Eleventh_Development_Plan_2019-2023.pdf

El-Din, M. M. S., (1999) *Optimal utilization of waste heat from heat engines by use of a heat pump*, Energy Conversion and Management, 40:937-949

Kim, J. K., Oh, B.R., Chun, Y. N., Kim S. W. (2006) *Effects of temperature and hydraulic retention time on anaerobic digestion of food waste*, Journal of Bioscience and Bioengineering 102:328–332

Maidment, G. G., Eames, I. W., Psaltas, M., Lalzad, A., (2006) *Potential application of a flash-type barometric desalination plant powered by waste heat from electric-power stations in Cyprus*, Applied Energy, 83:1089-1100

Ministry of Energy and Natural Resources, Biomass Energy. https://enerji.gov.tr/bilgi-merkezi-enerji-biyokutle

Romero, R. J., Rodríguez-Martínez, A. (2008) *Optimal water purification using low grade waste heat in an absorption heat transformer*, Desalination, 220:506-513

Tay, J. H., Low, S. C., Jeyaseelan, S., (1996) *Vacuum desalination for water purification using waste heat*, Desalination,106:131-135

Ulusoy, Y. A., Ulukardeler, H., Ünal, H., Aliba, K. (2009) *Analysis of biogas production in Turkey utilizing three different materials and two scenarios*, African Journal of Agricultural Research, 4(10):996-1003

Oğulata, R. T., (2004) *Utilization of waste-heat recovery in textile drying*, Applied Energy, 79:41-49

Oktay, Z. (2009) *Investigation of coal-fired power plants in Turkey and a case study: Can plant*, Applied Thermal Engineering, 29(2-3):550-557

Xinshan, Q., Zhang, S., Wang, Y., Wang, R. (2005) *Advantages of the integrated pig-biogas-vegetable greenhouse system in North China*, Ecological Engineering, 24:175–183

Walla, C., Schneeberger, W. (2008) The optimal size for biogas plants, Biomass and Bioenergy 32:551–557

Chapter 2

GREENHOUSE MONITORING AND CONTROLLING SYSTEMS USING IMAGE PROCESSING AND SENSORY TECHNIQUES

Abdalrazg BENNASER[1]

Necmi Serkan TEZEL[2]

1 M.Sc. Abdalrazg BENNASER, Department of Electrical-Electronics Engineering, Faculty of Engineering, Karabük University, 78050, Karabük, Turkey.

2 Prof. Dr. Necmi Serkan TEZEL, Department of Electrical-Electronics Engineering, Faculty of Engineering, Karabük University, 78050, Karabük, Turkey, ORCID ID: 0000-0002-9452-677X

1. INTRODUCTION

The design of smart greenhouse system has been a subject of interest for several years, which is attributed to the scalability drive of agriculture to meet demands [1]. Current greenhouse techniques require high workmanship in monitoring and control that consume a lot of manhours and require competitive skills. These factors add several challenges to scalable agriculture such as costs and lack of enough human skills that can identify and control issues in crops [2]. Due to the development in electronics technology, it became possible to replace these skills with automized systems to identify issues and allow the control of affecting conditions [3]. Furthermore, the current technologies in agriculture allow farmers to automate several recurring activities, including pesticide spraying, supporting soil with fertilizer, weeding unwanted growth, and plant irrigation [4]. These systems are mainly based on a pre-scheduled program and are more action oriented rather than comprehensive systems that can provide reliable data feedback. Additionally, the current research trend is developing and implementing a full diagnosis and control system that can identify issues within greenhouses and allow their owners to take decisions accordingly, despite the view of it being a very unrealistic based on the current achievements in research and practice [5].

Image processing is a rapidly developing technique that allows the identification of non-conforming samples and assigning a specific value to each condition based on machine learning methods. Agriculture has high potential to benefit from this technology as crops are highly identifiable by their appearance, which makes image sensory and processing a key solution that can replace or support skills in the greenhouse [6]. Moreover, greenhouses are used to provide controlled conditions to the crops based on needs and for growing them in severe outdoor conditions. The currently used techniques are conventional systems that require manpower presence in the facility. The availability of suitable sensory technology and action tools allow the control of these conditions remotely through a mobile application. Therefore, such a solution allows to sensor and controls the conditions within the greenhouse, or multiple greenhouses, instantly without the need for physical human presence [7].

Designs and simulations for greenhouse system is significant research subject due to critical need of systems that can bridge the gaps in manpower and scalability. Therefore, monitoring and control system are necessary to achieve agricultural production goals and cost control. Image processing is a rapidly developing technique that allows the identification of non-conforming samples and assigning a specific value to each condition based on machine learning methods. Moreover, Control system depending on

microcontrollers, sensors, and intervention tools were found effective in the greenhouse context. The aim of the current research is to design a monitoring system for the conditions of plantations in greenhouses using image processing techniques and allow for controlled conditions based on automation, as well as human judgement, through a controlling system with sensory techniques adjusted using an android phone application. A monitoring system was designed through using image processing and CNN machine learning techniques. The system was developed through the use of Raspberry Pi 4 Model B as a microprocessor, a Raspberry Camera rev 1.0, and a machine learning code. The outcomes of image processing were judged on a binary system of 1 = wanted and 0 = unwanted for image classification. The accuracy of the system was tested through three arrangements: 60% training/ 40% testing with an accuracy of 96.32%, 70% training/ 30% testing with an accuracy of 98.43%, and 80% training/ 20% testing with an accuracy of 99.14%. The greenhouse setting was put to test and the system was able to correctly identify all samples according to their true classification. A comparison with the literature showed that the designed system is superior based on the complexity of criteria through an RGB classification. The control system was designed to monitor vital greenhouse parameters: temperature and humidity, rain, and soil moisture. An Arduino UNO microcontroller was used to control the system. Control components included ventilation fans, infrared lamp, water pump, side and top louvers, and spectrum LED light. A mobile application was designed as a user interface to monitor changes in the environment, in addition to functions of system components in response to changes in the vital greenhouse parameters. A simulation of the setup was performed through forced testing modes: increase in temperature (mode 1), decrease in temperature (mode 2), decrease in soil moisture level (mode 3), decrease in humidity level (mode 4). The efficiency of the system is proven through the testing modes and the comparison to similar systems in the literature showed the extensivity and dependability of the designed control system.

2. RESEARCH AIM AND OBJECTIVES

The main aim of the research is to design a monitoring system for the conditions of plantations in greenhouses using image processing techniques and allow for controlled conditions based on automation, as well as human judgement, through a controlling system with sensory techniques adjusted using an android phone application. The achievement of the targeted systems requires the fulfilment of the following objectives:

- Understand the needs of automated greenhouse systems and the critical criteria that need to be addressed in functional electronics design.

- Design a diagnostic monitoring system that provides an educated judgment of plant conditions based on database information collected from the field and image processing techniques.

- Design a diagnostic and interventive controlling system that provides greenhouse conditions to the user, including heating and humidity, which are critical for plant growth and development. Information is fed to the system through sensory techniques into an interactive android application, where the user can adjust these conditions accordingly.

- Demonstrate the functions of the systems through an actual greenhouse set up, where the two systems function to achieve their design intents.

- Investigate the potential benefits of the systems and compare them to similar systems suggested in the literature to comprehend opportunities and limitations.

3. SCOPE, METHODS AND RESEARCH SIGNIFICANCE

The designed systems use different techniques according to the capabilities and needs of the intended functions. The monitoring system use image processing techniques with a reasonable database for daisy flowers. The system uses Raspberry Pi as a microcontroller for the system and provides feedback on plant conditions according to implemented algorithms. The controlling system uses sensory techniques for temperature and humidity conditions that is fed to an android mobile application, where the user can interact with these conditions by increasing them or decreasing them using an infrared light and a water tank. The system is operated using an Arduino microcontroller.

The designs targeted by the current research allows for alarming farmers of their plant conditions, monitoring greenhouse environment, and adjusting this environment to enhance plant conditions. Furthermore, these systems allow the remote interaction with these systems through a mobile application, which facilitates the scalability factor that forms a challenge in agriculture. This means that instead of designating a technician to each greenhouse, a single technician can monitor those systems and assign the necessary actions, which reduces costs, efficiency, and productivity in greenhouses. The image processing technique used in the monitoring system has been identified as a modern and promising research field by several journals [8-9], while research shows that such systems can be highly efficient in terms of performance and quality. The targeted monitoring system in the current research aims to exceed the 96% accuracy threshold that had been demonstrated in most previous research of agricultural grading systems [10]. Additionally, the controlling system

added in this research allows for remote interaction that solves another issue in agriculture in regards with costs and scalability. The designs that are presented in this research form a key stepping point into technology implementation for wider range of plants and crops that are placed greenhouses.

4. SYSTEM DESIGN

The designed system is formed by two main modules: the monitoring system using image processing technique, and the control system for vital environment control through sensor techniques. The following sections discuss the design of each module in terms of their components, integration, mechanisms, and expected outcomes.

4.1. Monitoring system

The system for monitoring is an image processing assembly that is formed by the image acquisition components and the machine learning algorithm that performs judgements based on database patterns. The hardware of the system contains two main components, as shown in Figure 1: a microprocessor: Raspberry Pi 4 Model B, a camera (Raspberry Camera Rev 1.0), and power supply through the USB port. The Raspberry camera is connected to the CSI port in order to feed the Raspberry Pi 4 Model B microprocessor with images from the greenhouse simulator. The camera has a still resolution of 5 Megapixels and have video modes reaching up to 1080p30. Sensor on the camera is OmniVision OV5647 and images have a pixel size of 1.4 x 1.4 microns. The camera supports different picture formats, including RGB888, YUV420, PNG, BMP, and JPEG. Several features are added to the camera, such as OpenCV integration, motion detection, DRC and HDR customizations, and user-definability image effect. It has obvious compatibility with Raspberry microprocessors and all camera tuning aspects can be altered, which provides high flexibility in image processing applications.

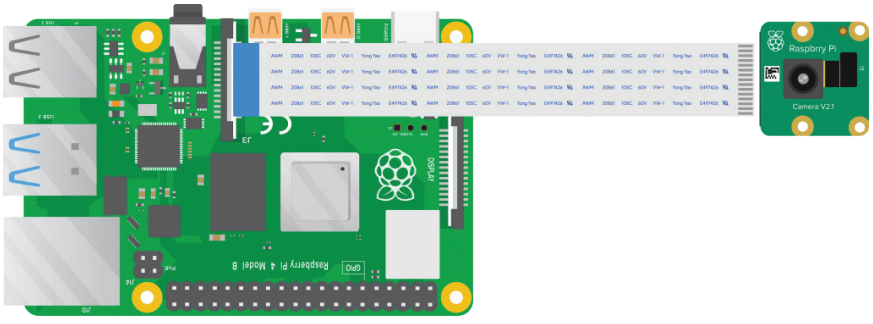

Figure 1. Monitoring system schematic setup.

A machine learning algorithm is designed to identify the compliance of plant samples based on their color compatibility. Coding is performed

on Python3 and the code with the used algorithm is provided in appendix A. A database of 607 samples was used to train and test the database with a CNN technique using the following steps:

- Creation of convolutional filter through feature maps with equation (1):

$$(f * g) \overset{def}{=} \int_{-\infty}^{\infty} f(\tau) g(t-\tau)\, d\tau \tag{1}$$

- Add Rectified Linear Unit layer (ReLU) with the function shown in equation (2):

$$\phi(x) = \begin{cases} 0 & for \quad x<0 \\ x & for \quad x\geq 0 \end{cases} \tag{2}$$

- Use max pooling to create pooled feature maps
- Creation of flattened layer
- Merge to create connection
- Output layer and class recognition
- Use Sigmoid function (3):

$$S(x) = \frac{1}{1+e^{-x}} \tag{3}$$

- Distances from true values are measured using crossed-entropy function shown in equation (4):

$$H(p,q) = -\sum_{x} p(x) \log q(x) \tag{4}$$

The algorithm and results on the accuracy of fault detection was calculated. The code is tested for image processing from the greenhouse environment, which filters database pictures for unusable images. Finalized images are divided through the algorithm into smaller sections for pattern comparison with the training set. Through this process, the code was able incompatibilities in other characteristics, besides color, such as shapes, angles, and orientations in order to help the machine learning algorithm identify unconformities. Each pixel is then assigned to a number (either 1 or 0).

4.2. Control system

An Arduino UNO microcontroller is used as the heart of an agricultural control system, which is designed to control the environment within the greenhouse through vital indicators and intervention measures, as shown in the schematic in Figure 2. Three sensor types are used for the system: temperature and humidity sensor (DHT11), rain sensor, and soil moisture sensor. Based on the sensor types that are used in the design, it is evident that the main controlled parameters are temperature, humidity, and soil moisture. Lighting is also controlled by the system through simulating daylight. Subsequently, these parameters are controlled using:

- Louvers that open to the side and at the top of the greenhouse for ventilation, reduction of temperature, when needed, connected to the system with a servo motor.
- Infrared lamp to heat air within greenhouse if temperature drops below the minimum limit.
- Fans that circulate air and their speed is controlled through an L298N (U1) controller, which supplies the fans with power according to the needed speed.
- A Spectrum led that generates UV lights with 220-volt power to simulate sunlight. Since the greenhouse is not exposed to sunlight, the microcontroller is programmed to provide a steady rate of UV rays for certain hours per day.
- A water pump with a reservoir to supply soil with water as needed by the system.

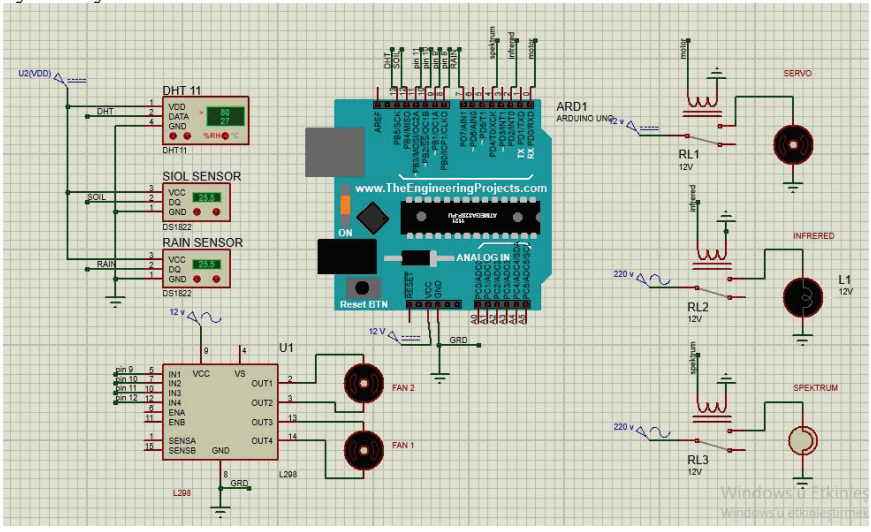

Figure 2. Schematic diagram of the designed greenhouse control system.

The control of the system is performed through an Arduino UNO code provided in Appendix B. The code provides the control of all sensor and intervention components connected to the microcontroller. Feedback is sent by the microcontroller to an android application, as shown in Figure 3. The modes of control are implemented into the code; however, the mobile application allows the operator to monitor the conditions of the greenhouse and overwrite changes as judged suitable. The final greenhouse setup is presented in Figure 4.

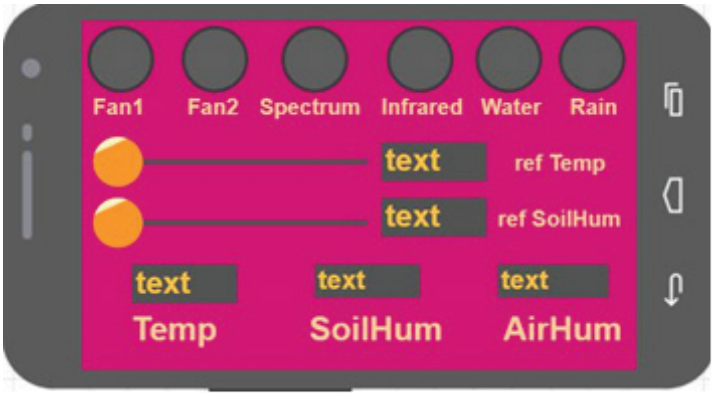

Figure 3. Interface screen of greenhouse control system.

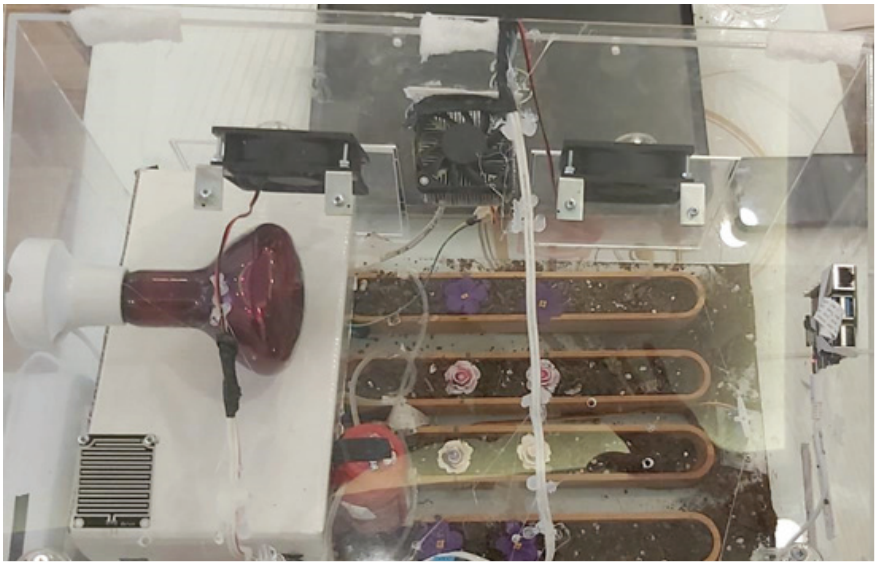

Figure 4. Greenhouse simulation setup.

5. RESULTS

5.1. Accuracy and Precision of Monitoring System

A total of 772daisy flower samples were used, where the set was divided into three train-test splits: 60-40, 70-30, and 80-20. The maximum epoch number was set to 5 and the model accuracy reached for the three splits were 96.32%, 98.43%, and 99.14%, respectively (Figure 5). The model losses were recorded at epoch 5 for the three models as 0.153, 0.072, and 0.056, respectively.

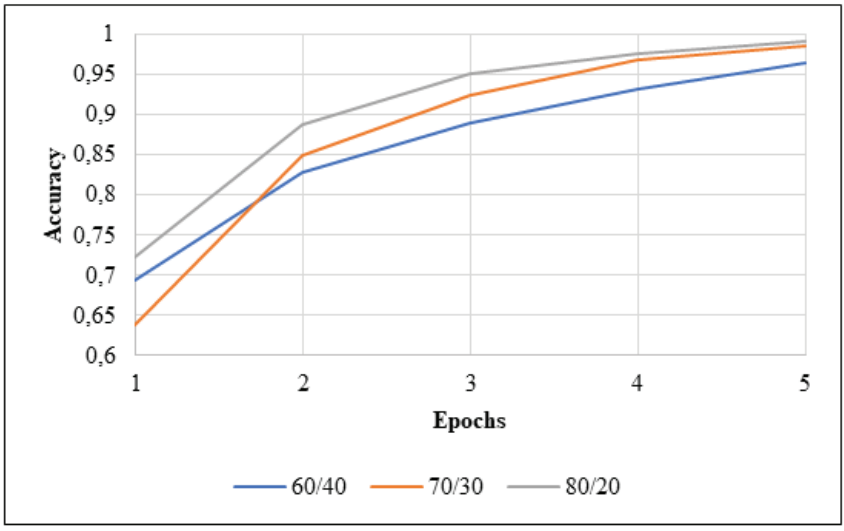

Figure 5. Machine learning model accuracy for daisy flowers.

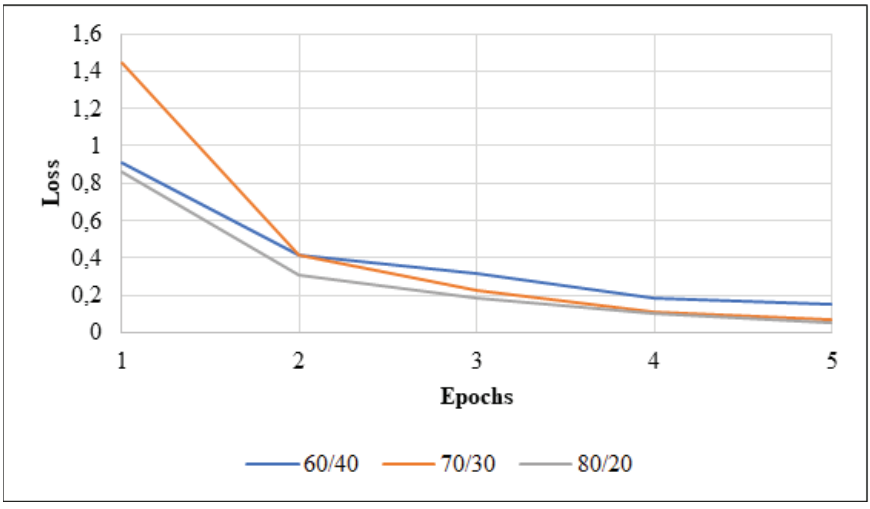

Figure 6. Machine learning model loss for daisy flowers.

5.2. Performance of Control System

The control system functionality and performance were tested through four modes of change forced through manually manipulating the values of the indicators on the mobile application. The control system has a manual and automatic modes, where in the latter values were fixed, as shown in Table 1. The four testing modes are:

- Mode 1: increasing the temperature in the greenhouse to 30°C. The system responded to user order after switching it to manual mode and the infrared lamp heated the closed greenhouse to the set temperature.
- Mode 2: decreasing the temperature in the greenhouse after switching off the control system by using a block of ice and leaving the environment to cool to 18°C.
- Mode 3: Drying the soil using a hair dryer after switching off the system to reduce the soil moisture level to below 20%.
- Mode 4: Drying greenhouse environment with hot airflow from hair dryer while system is off until humidity is below 20%.

Table 1. Set of parameter values built in the control system for the greenhouse

Parameter	Set range
Temperature	22 – 22.5 °C
Humidity	60% - 80%
Soil moisture	85% to 100%

After applying testing mode 1, the temperature inside the greenhouse was recorded as 30.2 °C. The control system was returned back to the automatic mode and started, where the fans started operating and side ventilation louvers were open. The system response was recorded 6 seconds after the change to the automatic mode. As shown in Figure 7, the temperature in the greenhouse set up started decreasing in response to testing mode 1 and achieved in the range in 83 seconds.

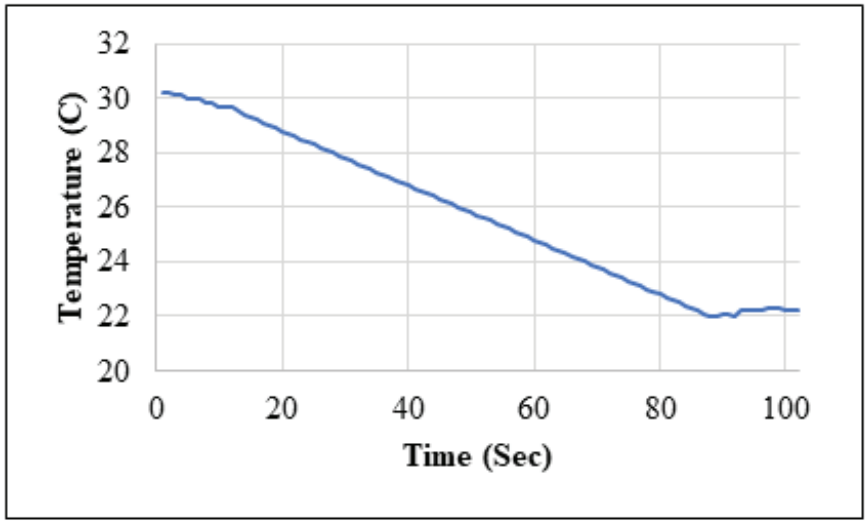

Figure 7. Temperature adjustment by control system in response to testing mode 1

After applying testing mode 2, the temperature inside the greenhouse was recorded as 18.1 °C. The ice block was kept in the greenhouse and the control system was returned back to the automatic mode and started, where the louvers were completely closed, and the infrared lamp started working. The system response was recorded 2 seconds after the change to the automatic mode. As shown in Figure 8, the temperature in the greenhouse set up started increasing in response to testing mode 2 and achieved in the range in 57 seconds.

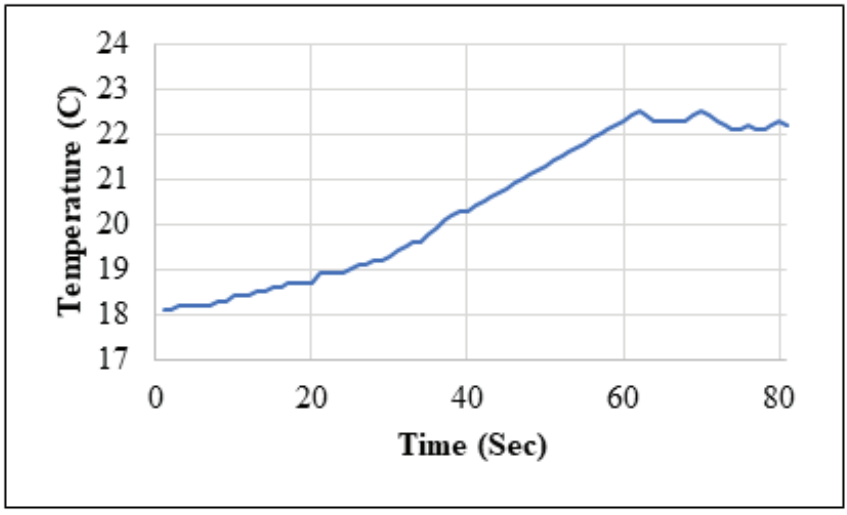

Figure 8. Temperature adjustment by control system in response to testing mode 2

After applying testing mode 3, the soil moisture level was reduced to 19.4% while the control system was set to manual mode. The automatic mode was switched on, where the water pump started working to adjust moisture level after 5 seconds. As shown in Figure 9, water started flowing into the planters in the greenhouse, which increased the soil moisture level to the 85% minimum and continued increasing after 30 seconds.

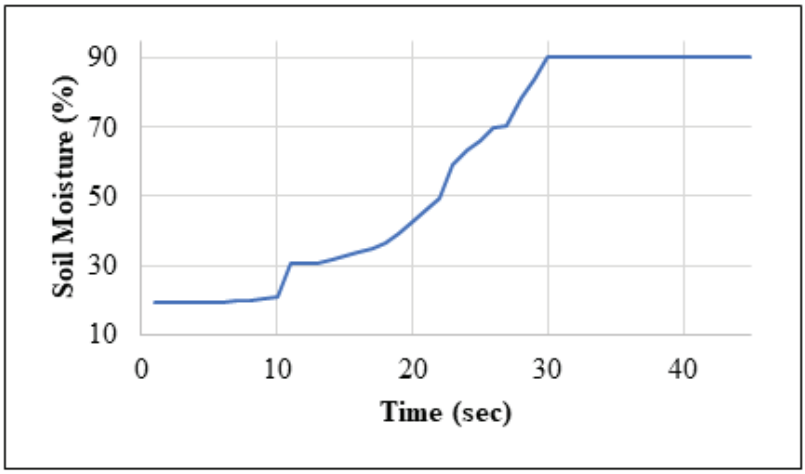

Figure 9. Soil moisture adjustment by control system as a response to testing mode 3

After applying testing mode 4, the humidity inside the greenhouse was reduced to 18.3% while the control system was set to manual mode/ switched off. The automatic mode was switched on, where the water pump started working to remoisturize the soil planters and infrared lamp worked to increase temperature to simulate more water evaporation. The system responded to the initial humidity reduction in 7 seconds after it was switched on. As shown in Figure 10, water started flowing into the planters in the greenhouse and the increased heat assisted evaporation, which increased humidity level to the 60% minimum threshold after 326 seconds and continued increasing up to 65%, when system switched to adjust other parameters.

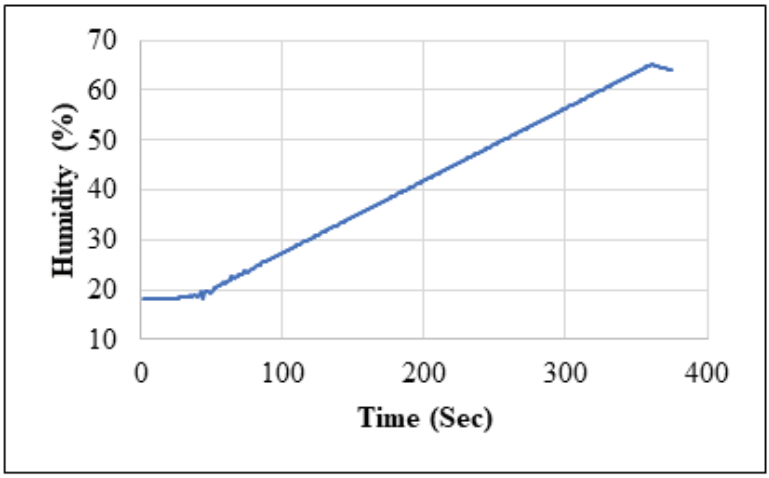

Figure 10. Humidity adjustment by control system as a response to testing mode 4

6. DISCUSSION

The current research designed and implemented a monitoring system and a control system for greenhouse agriculture with the coordination of several complex components. The monitoring system used a Raspberry Pi 4 Model B microprocessor to empower a machine learning algorithm. The accuracy of the system was calculated as 96.32% with a 60% training set, 98.43% with a 70% training set, and 99.14% with a 80% training set. The system was able to identify all samples presented within the greenhouse, which demonstrates the potential of the created solution. The implemented solution identified the healthiness of the plant sample through analyzing pictures acquired through a camera and provided a binary result of the qualification or disqualification of the plant sample based on its appearance. The accuracy rate obtained in both cases exceed the 96% achieved by Pixia and Xiangdong[11] in detecting disease pigmentations in cucumber grown in a greenhouse simulation. Zhou et al.[12] developed a similar system to the one implemented in the current research for the detection of ripening of three species of strawberry. The accuracy measure used the same methods through a training and testing sets, where the highest accuracy was calculated as 89.6%. Table 5.1 shows a comparison of accuracy rates between the monitoring system in the current research and similar systems in the literature.

Table 5. 1. Comparison of accuracy for image processing and machine learning studies

Study	Technique	Best Accuracy
Current Monitoring System	CNN Technique	99.14%
Pixia and Xiangdong [11]	Supervised learning	96%
Zhou et al. [12]	Unsupervised learning	89.6%

The accuracy of a monitoring system dependent on anmachine learning technique is dependent mainly on two factors: the size of the training set and the complexity of the criteria that are identified through the system. Zhang and Xu [13] tested an unsupervised algorithm similar to the one implemented in the current research in enhancing analysis techniques based on an image database. The system was tested on tomato and used ten picture images to analyze the image. The best accuracy value of 94.09% was achieved on one of the images using the machine learning technique. An accuracy reaching to 98.24% was achieved using the same technique on the increase of the size of the training set. Similarly, Xu et al. [14] claimed the achievement of a high accuracy using the same technique that exceeded the achieved 97.4% in the current research. Nonetheless, the authors of the research designed their system to recognize the existence of the crop in a certain position. Thus, the intent of their design was to locate the plant rather than analyze its characteristics. The monitoring system implemented in the current research demonstrated higher complexity through analyzing the RGB patterns on the acquired plant images from the greenhouse, which is considered a more complex task to be fulfilled through CNN machine learning techniques. Therefore, the accuracy level that was achieved by the system can be deemed high in comparison with similar systems and it exceeds the accuracy levels of systems with the same level of complexity.

The control system presented in the current research expanded this approach to a user interface and interventive control system that is able to adjust greenhouse environmental parameters based on ideal set of values. The efficiency of the system was tested through forced testing modes in order to understand the system's response to extreme change conditions. Wudneh and Vanitha [15] developed a monitoring system with the use of Raspberry Pi 3 as a microcontroller. The system had an architecture that included a monitoring camera, soil humidity sensor, and a DHT11 sensor. The study included graphs of temperature changes and soil moisture changes over a twenty-minute period. The picture acquisition through the camera did not serve a real function other than providing pictures to the system to save. It is evident that the system was solely designed for monitoring purposes, which makes the control system developed in this research more superior.Lakhiar et al. [16] presented an architecture of a

control system that implements IoT for the control irrigation, humidity, temperature, and carbon dioxide levels. The research developed a similar design to the control system presented in the current research. However, the system was not implemented nor tested for performance. Additionally, the proposed architecture did not indicate an automated mode but only a manual control using a mobile application. A similar system was designed by Osama et al. [17], where the system demonstration used LED lights to simulate growth for tomatoes in a greenhouse. Other sensors were added to the system for temperature, humidity, and soil pH level. However, these systems were for monitoring purposes without any intervention frameworks like the one imposed for LED lights. The system was also dependent on user controls without automation.

7. CONCLUSION

The problem addressed in the current research is the development of a smart greenhouse monitoring and control systems that enable agricultural applications for image classification using processing techniques, as well as monitor vital parameters within the greenhouse environment with an automated mode with the ability for user intervention. The current systems presented in the literature lack the ability to develop such systems with adequate application that can be used in greenhouse settings. Therefore, the current study aimed for designing a monitoring system for the conditions of plantations in greenhouses using image processing techniques and allowing for controlled conditions based on human judgement through a controlling system with sensory techniques adjusted using an android phone application.

The designs targeted by the current research allows for alarming farmers of their plant conditions, monitoring greenhouse environment, and adjusting this environment to enhance plant conditions. Furthermore, these systems allow the remote interaction with these systems through a mobile application, which facilitates the scalability factor that forms a challenge in agriculture. This means that instead of designating a technician to each greenhouse, a single technician can monitor those systems and assign the necessary actions, which reduces costs, efficiency, and productivity in greenhouses.

A monitoring system was designed through using image processing and machine learning techniques. The system was developed through the use of Raspberry Pi 4 Model B as a microprocessor, a Raspberry Camera rev 1.0, and a machine learning code. The outcomes of image processing were judged on a binary system of 1 = wanted and 0 = unwanted for image classification. The accuracy of the system was tested through two arrangements: 60% training/ 40% testing with an accuracy of 96.32%,70% training/ 30% testing with an accuracy of 98.43%, and 80% training/ 30% testing with an accuracy of 99.14%. The greenhouse setting was put to

test and the system was able to correctly identify all samples according to their true classification. A comparison with the literature showed that the designed system is superior based on the complexity of criteria through an RGB classification.

The control system was designed to monitor vital greenhouse parameters: temperature and humidity, rain, and soil moisture. An Arduino UNO microcontroller was used to control the system. Control components included ventilation fans, infrared lamp, water pump, side and top louvers, and spectrum LED light. A mobile application was designed as a user interface to monitor changes in the environment, in addition to functions of system components in response to changes in the vital greenhouse parameters. A simulation of the setup was performed through forced testing modes: increase in temperature (mode 1), decrease in temperature (mode 2), decrease in soil moisture level (mode 3), decrease in humidity (mode 4). Response to mode 1 decreased temperature in greenhouse from 30.2 °C to the allowable range of 22 – 22.5 °C in 83 seconds through activating the fans and opening the side louvers. System responded to the change in 6 seconds. Response to mode 2 increased temperature in greenhouse from 18.1 °C to the same allowable range in 57 seconds through the activation of the LED lamp. System was activated in 2 seconds. Response to mode 3 increased soil moisture level from 19.4% to the allowable range of 85% to 100% in 30 seconds. System was activated in 5 seconds. The efficiency of the system is proven through the testing modes and the comparison to similar systems in the literature showed the extensivity and dependability of the designed control system. Response to mode 4 increased humidity from 18.3% to 60% in 326 seconds, while system was activated in 7 seconds.

The current systems can be altered to test its efficiency with different types of crops and plants. Changes in the machine learning code seem to be necessary in order to adjust the system to changes in attributes. The accuracy and precision of the system can be obtained and compared with the results of the research.Moreover, the current designed systems can be enhanced in future research through several additions. It would be significant to integrate the monitoring and control system into one system in order to turn the monitoring system into a sensor that allows for intervention using the control system. However, such an integration requires major development for the monitoring system to communicate with the control system for a suitable intervention through the available components. Actions such as removal of plant, fertilization, and pest control is required to be added to the control system in order for it to become effective. The adequacy of the used microprocessor (Raspberry Pi 4 Model B) and microcontroller (Arduino UNO) need to be re-evaluated in such as system.

9. References

[1]	K. Jha, A. Doshi, P. Patel and M. Shah, "A comprehensive review on automation in agriculture using artificial intelligence," Artificial Intelligence in Agriculture, vol. 2, pp. 1-12, 2019.
[2]	C. Lunner-Kolstrup, T. Horndahl and J. P. Karttunen, "Farm operators' experiences of advanced technology and automation in Swedish agriculture: a pilot study," Journal of Agromedicine, vol. 23, no. 3, pp. 215-226, 2018.
[3]	S. Rotz, E. Gravely, I. Mosby, E. Duncan, E. Finnis, M. Horgan, J. LeBlanc, R. Martin, H. T. Neufeld, A. Nixon, L. Pant, V. Shalla and E. Fraser, "Automated pastures and the digital divide: How agricultural technologies are shaping labour and rural communities," Journal of Rural Studies, vol. 68, pp. 112-122, 2019.
[4]	T. Talaviya, D. Shah, N. Patel, H. Yagnik and M. Shah, "Implementation of artificial intelligence in agriculture for optimisation of irrigation and application of pesticides and herbicides," Artificial Intelligence in Agriculture, vol. 4, pp. 58-73, 2020.
[5]	R. R. Shamshiri, C. Weltzien, I. A. Hameed, I. J. Yule, T. E. Grift, S. K. Balasundram, L. Pitonakova, D. Ahmad and G. Chowdhary, "Research and development in agricultural robotics: A perspective of digital farming," International Journal of Agricultura and Biological Engineering, vol. 11, no. 4, pp. 1-14, 2018.
[6]	H. Tian, T. Wang, Y. Liu, X. Qiao and Y. Li, "Computer vision technology in agricultural automation —A review," Information Processing in Agriculture, vol. 7, no. 1, pp. 1-19, 2020.
[7]	U. Shafi, R. Mumtaz, J. Garcia-Nieto, S. A. Hassan, S. A. R. Zaidi and N. Iqbal, "Precision Agriculture Techniques and Practices: From Considerations to Applications," Sensors (Basel), vol. 19, no. 17, 2019.
[8]	S. Rasti, C. J. Bleakley, N. M. Holden, R. Whetton, D. Langton and G. O'Hare, "A survey of high resolution image processing techniques for cereal crop growth monitoring," Information Processing in Agriculture, 2021.
[9]	I. H. Syeda, M. M. Alam, U. Illahi and M. M. Su'ud, "Advance control strategies using image processing, UAV and AI in agriculture: a review," World Journal of Engineering, vol. 18, no. 4, 2021.
[10]	A. Vibhute and S. K. Bodhe, "Applications of Image Processing in Agriculture: A Survey," International Journal of Computer Applications, vol. 52, no. 2, pp. 34-40, 2012.
[11]	D. Pixia and W. Xiangdong, "Recognition of Greenhouse Cucumber Disease Based on Image Processing Technology," Open Journal of Applied Sciences, vol. 3, no. 1B, pp. 27-31, 2013.
[12]	C. Zhou, J. Hu, Z. Xu, J. Yue, H. Ye and G. Yang, "A Novel Greenhouse-Based System for the Detection and Plumpness Assessment of Strawberry Using an Improved Deep Learning Technique," Frontiers in Plant Science, 2020.
[13]	P. Zhang and L. Xu, "Unsupervised Segmentation of Greenhouse Plant Images Based on Statistical Method," Scientific Reports , vol. 8, 2018.

[14]	Z. Xu, X. Shi, H. Ye and S. Hua, “Geometric Positioning and Color Recognition of Greenhouse Electric Work Robot Based on Visual Processing,” International Journal of Pattern Recognition and Artificial Intelligence, vol. 35, no. 2, 2021.
[15]	T. B. Wudneh and V. Vanitha, “Implementation of IoT With Image Processing in Greenhouse Monitoring System,” International Journal of Innovative Technology and Exploring Engineering, vol. 8, no. 9, pp. 509-514, 2019.
[16]	I. A. Lakhiar, G. Jianmin, T. N. Syed, F. A. Chandio, N. A. Buttar and W. A. Qureshi, “Monitoring and Control Systems in Agriculture Using Intelligent Sensor Techniques: A Review of the Aeroponic System,” Journal of Sensors, 2018.
[17]	R. Osama, N. Ashraf, A. Yasser, S. AbdelFatah, N. El Masry and A. AbdelRaouf, “Greenhouse Plant Growth Supervision with the LED Lights using Machine Learning,” in ICSIE 2020: Proceedings of the 2020 9th International Conference on Software and Information Engineering (ICSIE), Cairo, 2020.

Chapter 3

DETERMINATION OF THE EFFECT OF PI AND CONFINING PRESSURE ON THE SHEAR MODULUS OF UNDISTURBED SATURATED CLAYS AT SMALL STRAINS

Ersin GÜLER[1]

Kamil Bekir AFACAN[2]

1 Department of Civil Engineering, Faculty of Engineering and Architecture, Eskişehir Osmangazi University, Eskişehir, Turkey

2 https://orcid.org/0000-0002-5679-8838, https://orcid.org/0000-0002-3667-4432

1. Introduction

In earthquake prone zones, the behavior of soils under dynamic loads is of great importance in geotechnical and structural practice. Stress-strain characteristics and strength properties of soils change under cyclic loads caused by earthquakes. Correspondingly, excessive deformations occur on the ground surface resulting structural damage.

In order to know the stress-strain properties of soils under cyclic loads, both field and laboratory tests should be performed and their dynamic properties should be examined. Calculation of the parameters that make up the dynamic behavior of the soils will help in the prediction of earthquake waves to be transmitted to the surface. Therefore, the seismic loads that the structures will be exposed to can be modeled more realistically and the building elements will be dimensioned more securely.

These parameters are:

1) Maximum (initial) shear modulus-G_{max};

2) Normalized dynamic shift modulus G/G_{max} at different strain levels; and

3) The damping ratio turns out to be D and represents the dynamic behavior of the ground (Dobry and Vucetic, 1987; Darendeli, 2001; Okur and Ansal, 2007).

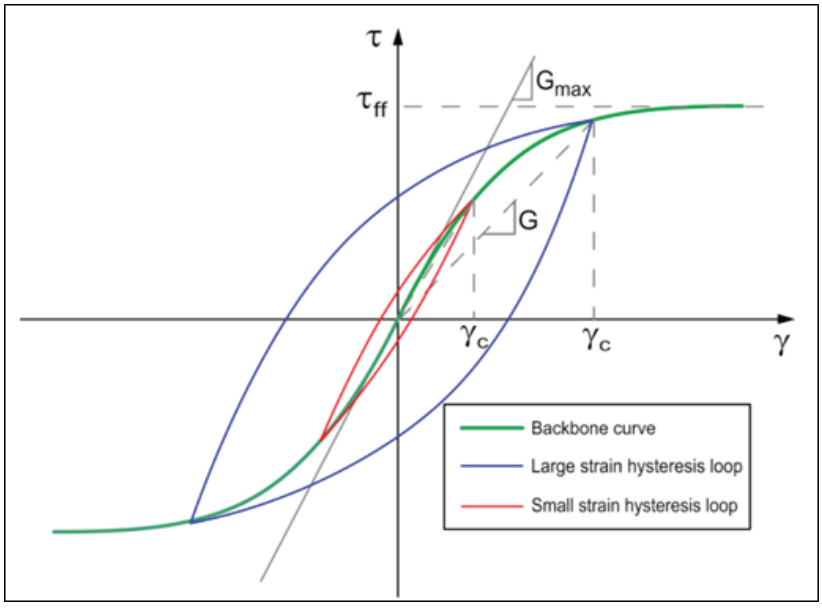

Figure 1. Stress-strain curve of the soils taken from Stewart et al. (Stewart vd., 2014)

Figure 1 shows the characteristics of soil under cyclic loading. As seen in the figure, the initial rigidty changes cycle by cycle and it reaches to the lowest value at failure.

Different test systems are used to determine the dynamic properties of soils. In the literature, it is seen that many studies have been carried out to evaluate the small deformation levels of sand and clay samples (Baziar et. al. 2009; Subramaniam and Banerjee 2016; Dutta et. al. 2017; Li and Senetakis 2018; Im et. al. 2017; Kahn et. al. 2011). Resonant Column (RC) test system is widely used in order to calculate the shear modulus or varying stiffness of soils at small deformation values in the laboratory as presented in Figure 2. With the tests carried out according to ASTM D 4015 standards, calculations of the dynamic properties of soils with unit deformation amplitudes between 0.1% - 0.001% can be made (Houbrechts et. al. 2011).

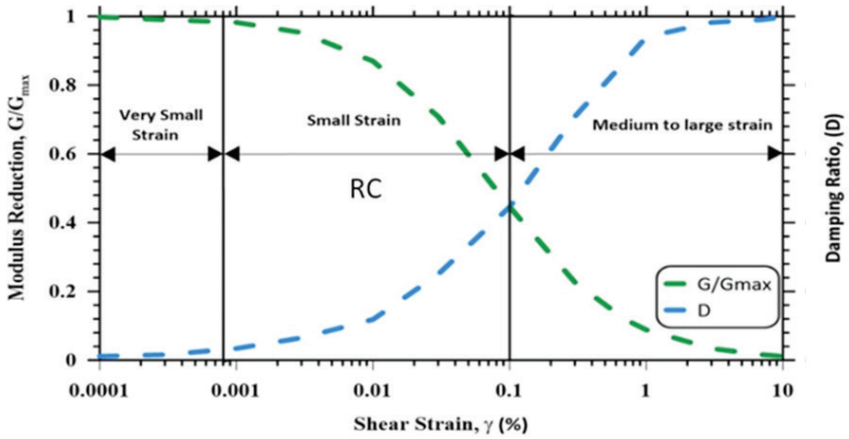

Figure 2. The modulus reduction and damping ratio curves

In their studies on RC experiments, Saxena and Reddy (1989) obtained shear modulus and damping ratio curves by using Monterey sand with a resonant column test system in their study. A formulation is proposed between Young's modulus and Poisson's ratio, and shear modulus and damping value.

Dutta et al. (2017) determined the dynamic properties of clay samples with a resonant column test system. The effect of saturation on shear modulus and the effect of poisson's ratio on dynamic parameters were investigated. As a result of the calculations made with the resonant column experiments on the sand samples, Li and Senetakis (2018) compared the test results with the reference model and a model was proposed using new

parameters.

Morsy et al. (2019) resonant column tests were carried out on sand samples under different tightness, saturation conditions and ambient pressure, and the shear modulus and damping ratio values of the samples were obtained. Dynamic properties of different sands and other comparisons were made.

Güler and Afacan (2020) examined the dynamic properties of samples with different properties using the RC experiment system in their study. The obtained data were compared with the reference models in the literature and evaluated.

2. Material and Method

2.1. Resonant Column System Test Apparatuses

Resonant column test system works based on wave propagation theory. The test system makes wave velocity measurements by applying vibration or torsional vibration to the sample in the longitudinal direction (Wilson and Dietrich, 1960; Hardin and Richart, 1963).

In the test system, one side of the sample is fixed and the other side is used as a free system. As seen in Figure 3, in the system where the lower head is fixed and the upper head is free, it generally consists of a cell and a pressure unit.

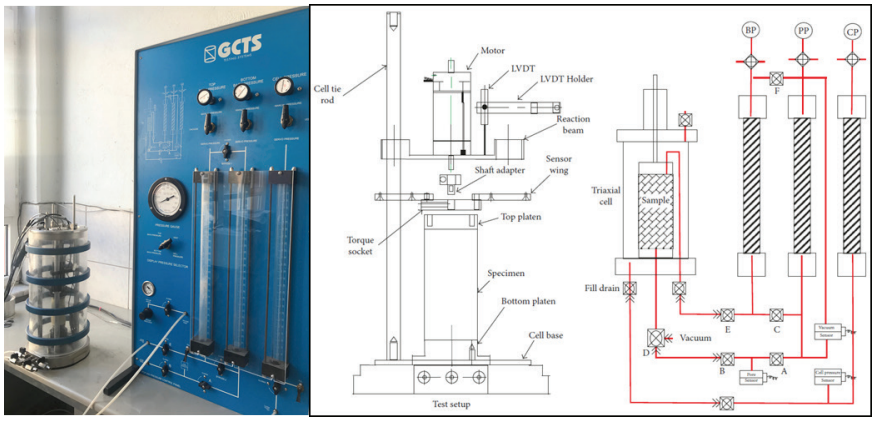

Figure 3. Resonant column test system

Torsional force is applied with the cylinder sample placed in the resonant column test system (Figure 3). The sample is twisted with dynamic torque at different frequencies and amplitudes applied from the sample

head. The resonance frequency and shear wave velocity are calculated by applying wave propagation theory. At this stage, the polar moment of inertia is also calculated and the shift to the shear modulus is made.

By keeping one side of the soil sample fixed and the torque applied by the other side, the sample is elastically rotated with a certain angle of rotation and returned to its original state. Applied torque (T);

$$T = GJ\frac{d_\theta}{d_z} \tag{2.1}$$

Torsional force is applied with the cylinder sample placed in the resonant column test system (Figure 5.19). The sample is twisted with dynamic torque at different frequencies and amplitudes applied from the sample head. The resonance frequency and shear wave velocity are calculated by applying wave propagation theory. At this stage, the polar moment of inertia is also calculated and the shift to the shear modulus is made.

By keeping one side of the soil sample fixed and the torque applied by the other side, the sample is elastically rotated with a certain angle of rotation and returned to its original state. Applied torque (T);

$$V_s = \sqrt{G/\rho} \tag{2.2}$$

Expressed. At the same time, the unit deformation amplitude (γ);

$$\gamma = \frac{r\theta_{max}}{h} \tag{2.3}$$

The distance from the axis of the ground (r) is expressed by the maximum angle of rotation (θ_{max}) and the height of the sample (h).

2.2. **Undisturbed Soils and Test Program**

Site conditions are important in determining the dynamic parameters of soils. With undisturbed samples, the conditions at the depth of the soils are met. Therefore, the presence of undisturbed samples will better reflect the site condition when determining the shear modulus and damping ratio values of soils.

Information on the samples made in the earthquake zone and obtained from different depths are shown in Table 1.

Table 1. Test Program and Soil Characteristics

Sample No	Depth (m)	w(%)	PI(%)	Test	Conf.Pres. (kPa)	Sample size(mm)
1	2.00	44.4	8	RC-1	50,100,200	50*100
2	6.50	43.8	12	RC-2	50,100,200	50*100
3	13.00	45.8	20	RC-3	50,100,200	50*100
4	16.50	49.5	24	RC-4	50,100,200	50*100

First of all, identification experiments were carried out on the undisturbed samples obtained after drilling. Then, the sample was trimmed to the dimensions of 50*100mm corresponding to the fit resonant column test system as shown in Figure 4.

Figure 4. *Trimming the size of the sample*

The sample and cell placed in the test system are shown in Figure 5. After the test system is prepared and its connections are made, the system becomes ready for the other stages.

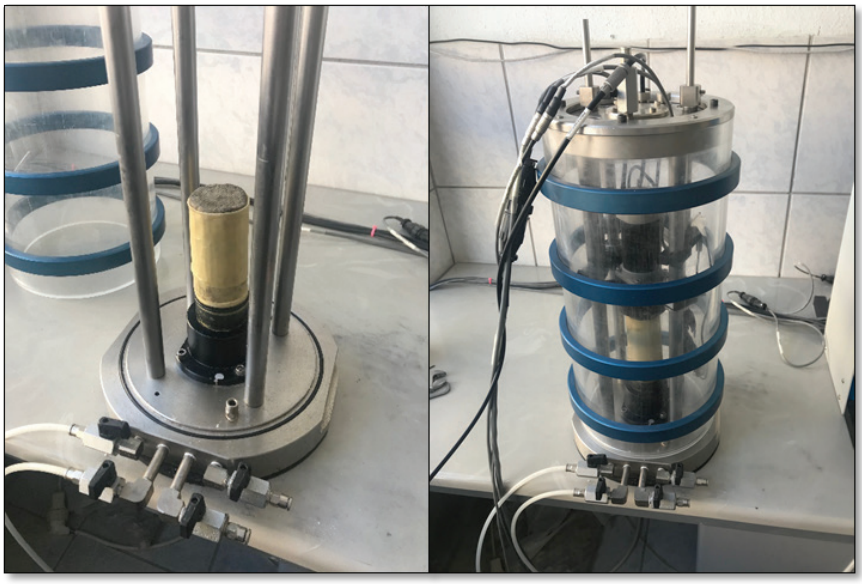

Figure 5. *Resonant column test system*

The experiment consists of the following stages:

• Preparation of the sample,

• Placement of the sample,

• Placement of the cell,

• Saturation of the sample,

• Consolidation of the sample and

• Applying force to the sample.

In the RC test system prepared for the experiment, all connections should be checked first. In the stage of placing the sample into the cell, the membrane is placed first of all. Here, the membrane is then placed into the membrane with the help of the sample placement tool. It is fixed to the bottom cap with silicone grease and 0-ring,

After the upper head is placed and connected with the o-ring, the motor part is connected. After the strain gauge and all other connections are made, the cell is placed. After the connections made on the cell, the sample is in the saturation phase. At the saturation stage, the B value is checked again and it is completed above 0.95. In the consolidation process, air is supplied to the system for the required ambient pressure, and it is consolidated. After this stage, the resonance frequency is controlled at

the required frequency and amplitude by applying residual force and the torque force is gradually increased.

The amplitude value corresponding to the resonant frequency is expressed as A_{max}. An example graphic obtained from the experiments is shown in Figure 6. The damping values can be calculated using the data obtained from the experiments. The damping values can be estimated using the formula in Equation 2.4 with the help of the frequencies corresponding to the half power band points, which are the frequencies corresponding to the point where A is the %70.7 of maximum amplitude (Morsy et. al 2018; Banerjee and Balaji, 2018; Bedr et. al. 2019).

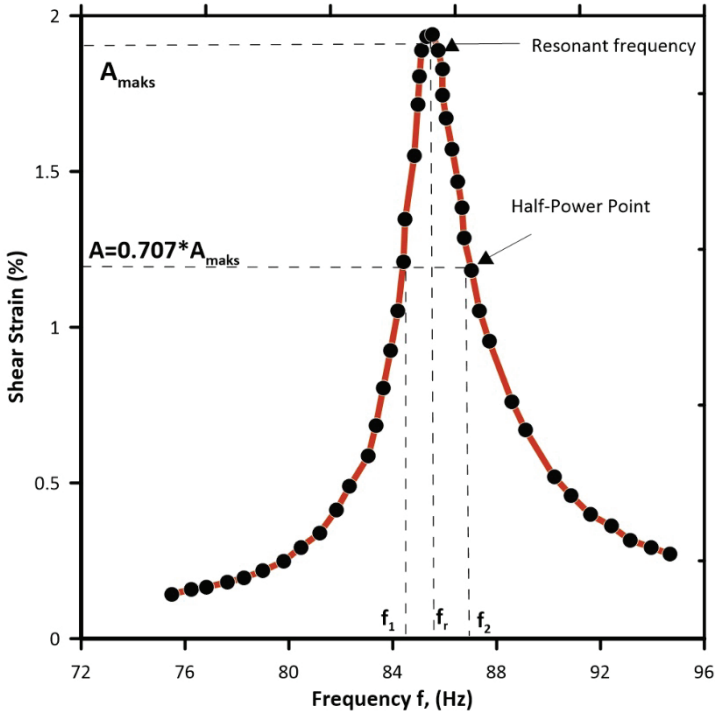

Figure 6. *Half power frequency curve*

3. Results and Discussion

As a result of the experiments and data evaluation, the shear modules and damping ratios of the different soil samples were obtained. In the experiments performed at small deformation levels, shear modulus-unit shear strain and damping ratio-unit shear deformation curves were obtained. Shear modulus-unit shear strain values for different loading levels for different undisturbed clayey soil samples are demonstrated in

Figure 7.

It was observed that initial shear modulus increased with the depth for all the cases although the change varies sample by sample. The test results show that the initial shear modulus values in sample 1 varied between 12-14 MPa resulting rough 17% change. Considering the confining pressure effect, it was determined that there was a difference up to 0.01% strain value, but then the gap was closed having similar results. Another important observation is that the G_{max} value in the 2nd sample varied between 12-14 MPa as well. Having similar water content of the soil sample, the PI effect was not clearly seen from the observations since samples have PI's of 8% and 12%, respectively. However, regarding the 3rd sample and 4th sample initial shear modulus varied between 16-24 MPa and 16-28 MPa correspondingly. The depth of the soil becomes more apparent with the increase of PI with almost 50% from 50 kPa confining pressure to 150 kPa. The increase in G_{max} value in samples 3 and can be explained by a combination effect of confining pressure and PI. Thus, overburden pressure and plasticity characteristics of soil are influential on the initial soil stiffness. It should also be noted that there were similar shear modulus values (having a narrow band) in all of the samples after the strain value of 0.01%.

The damping ratio curves obtained from the experiments are shown in Figure 8. As the depth of the samples increased and they became more rigid, damping ratio values decreased. In addition, the confining pressure effect is also seen in each sample although the effect is not super clear for sample 1 compared to the others. It also matches the outcomes from the shear modulus curves. Regarding the damping ratios at varying shear strain, the sample number 1 reached maximum damping values of 7%, the sample number 2 8%, the sample number 3 12%, and the sample number 4 16%, respectively. The plasticity is also eminently effective on the small strain damping as seen in the figure.

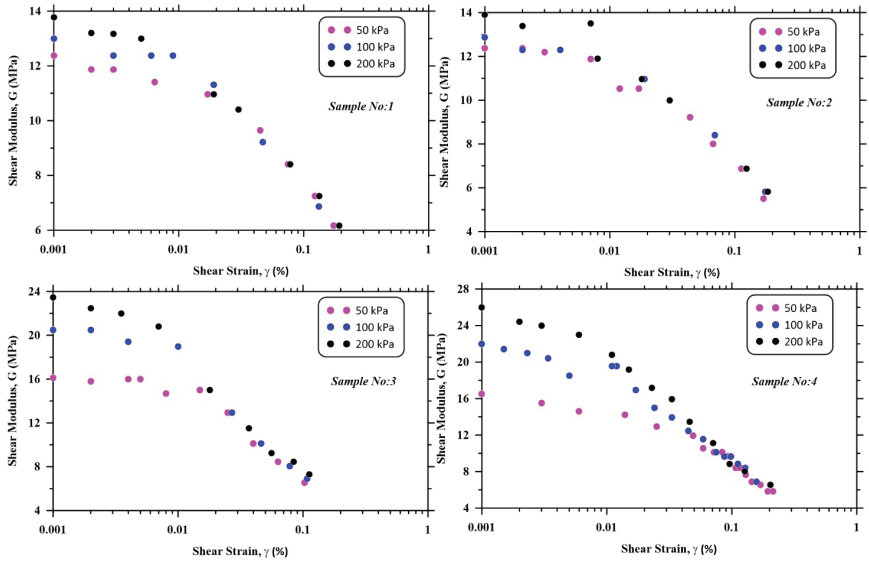

Figure 7. *Shear modulus-shear strain curves*

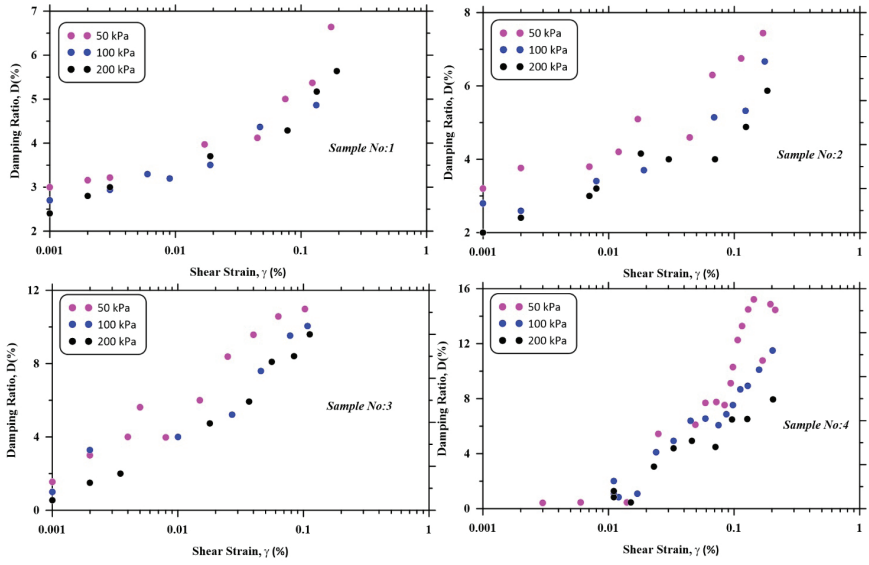

Figure 8. *Damping ratio-shear strain curves*

4. Conclusion

The behavior of soils under dynamic loads is of great importance in the design of structures. The behavior of the structures at small deformation levels is important for the safer and more economical design of the

structures. In this context, the dynamic properties at low shear deformation levels were obtained by performing a resonant column test on samples with different soil properties. As a result of the analysis, the following results were obtained.

As a result of 12 resonant column experiments performed on different samples and confining pressures;

• The shear modulus value of the clayey soils increases as the elevation that the soil sample is taken gets deeper.

• Secant modulus or shear modulus of the soils at different strain levels are very similar after 0.1% shear strain level even with the increase in confining pressure.

• PI is another crucial parameter that effects the initial shear modulus. The variation of shear modulus by increasing confining pressure alters with the change in PI resulting in couple significance on the rigidity of soil.

• It should also be added that these two parameters are also influential on the damping ratio values behavior of soils.

It was obviously concluded that it is important to determine the dynamic parameters of the soils in the design of the structures in the earthquake zones and estimating the initial soil modulus and its variation at small strain levels alter a lot with the plasticity and the depth of the soil.

References

Baziar, MH., Ghorbani, A., Katzenbach, R. Small-scale Model Test and Three-Dimensional Analysis of Pile-Raft Foundation on Medium-Dense Sand. Int J Civ Eng, 2009, 7, 170–5.

Banerjee, S., Balaji, P., Effect of Anisotropy on Cyclic Properties of Chennai Marine Clay. Int J Geosynth Gr Eng, 2018, 4, 1–11.

Bedr, S., Mezouar, N., Verrucci, L., Lanzo, G., Investigation on Shear Modulus and Damping Ratio of Algiers Marls Under Cyclic and Dynamic Loading Conditions. Bull Eng Geol Environ, 2019, 78, 2473–93.

Darendeli, MB., Development of a New Family of Normalized Modulus, 2001.

Dutta, TT., Saride, S., Jallu, M., Effect of Saturation on Dynamic Properties of Compacted Clay in a Resonant Column Test. Geomech Geoeng, 2017, 12, 181–90.

Dobry, R., Vucetic, M., Dynamic Properties and Seismic Response of Soft Clay Deposits. Int Symp Geotech Eng Soft Soils, Ciudad México 1987, 51–87.

Güler, E., Afacan, K.B., "Evaluation of Dynamic Properties of Soils with Low Deformation Levels Determined by Resonant Column Test" El-Cezerî Journal of Science and Engineering, 2020, 7 (2); 572-580.

Houbrechts, J., Schevenels, M., Lombaert, G., Degrande, G., Rucker, W., Cuellar, V., et al. RIVAS WP1.1 Test Procedures for the Determination of the Dynamic Soil Characteristics, 2011, 1–107.

Im, J., Tran, A.T.P., Chang, I., Cho, G.C., Dynamic Properties of Gel-Type Biopolymer-Treated Sands Evaluated by Resonant Column (RC) Tests. Geomech Eng, 2017, 12, 815–30.

Khan, Z., El Naggar, M.H., Cascante, G., Frequency Dependent Dynamic Properties from Resonant Column and Cyclic Triaxial Tests. J Franklin Inst, 2011, 348, 1363–76.

Li, H., Senetakis, K., Effects of Particle Grading and Stress State on Strain-Nonlinearity of Shear Modulus and Damping Ratio of Sand Evaluated by Resonant-Column Testing. J Earthq Eng, 2018, 1–27.

Morsy, A.M., Salem, M., Elmamlouk, H.H., 2019, Evaluation of dynamic properties of calcareous sands in Egypt at small and medium shear strain ranges. Soil Dynamics and Earthquake Engineering. 116. 692-708.

Okur, D.V., Ansal, A., Stiffness Degradation of Natural Fine Grained Soils During Cyclic Loading, Soil Dyn Earthq Eng, 2007, 27, 843–54.

Subramaniam, P., Banerjee, S., Torsional Shear and Resonant Column Tests on Cement Treated Marine Clay. Indian Geotech J, 2016, 46, 183–91.

Sexena, S.K., Reddy, K.R. 1989, Dynamic Moduli and damping ratios for monterey no.0 sand by resonant column tests. Soils and Foundations. 29, 37-51.

Stewart, JP., Afshari, K., Hashash, YMA., 2014, Guidelines for performing hazard-consistent one-dimensional ground response analysis for ground motion prediction Report PEER. 2014(16), 152.

Chapter 4

SYNTHESIS AND CHARACTERIZATION OF $SN_3SB_2S_6$ THIN FILM SUPERCAPACITOR ELECTRODES: THE EFFECT OF DEPOSITION TEMPERATURE

Necmi Serkan TEZEL[1],
Satiye KORKMAZ[1],
Fatma MEYDANERİ TEZEL[2]
İ. Afşin KARİPER[3,4]

1 Prof. Dr. Necmi Serkan TEZEL, Department of Electrical-Electronics Engineering, Faculty of Engineering, Karabük University, 78050, Karabük, Turkey, ORCID ID: 0000-0002-9452-677X

[1] Assist. Prof. Dr. Satiye KORKMAZ, Department of Electrical-Electronics Engineering, Faculty of Engineering, Karabük University, 78050, Karabük, Turkey, ORCID ID: 0000-0002-7592-3366

[2] Prof. Dr. Fatma MEYDANERİ TEZEL, Department of Metallurgy and Materials Engineering, Faculty of Engineering, Karabük University, 78050, Karabük, Turkey, ORCID ID: 0000-0003-1546-875X

[3,4] Assoc. Prof. Dr. İ. Afşin KARİPER, [3] Department of Science Educations, Faculty of Education, Erciyes University, 38039, Kayseri, Turkey; [4]Erciyes Teknopark, Building Number 1, No. 41, 38039, Kayseri, Turkey, ORCID ID: 0000-0001-9127-301X

1. INTRODUCTION

Sulfosalts are formed from a complex sulfide mineral. Their chemical form is $A_mB_nX_p$, where A is a metal, B is a semi-metallic material, X may be sulfur (S) or Selenium (Se) [1]. They are prepared using various methods, including RF sputtering, sputtering, pulsed laser deposition, vacuum evaporation, sonochemical synthesis, electron beam, chemical vapor deposition, thermal evaporation, and chemical bath deposition. Many properties of these materials have been the subject of numerous studies [2-5]. Thin-film form may work better in single and polycrystalline solar cells because a small amount of material can meet their requirement. Thin-film solar cells reached an efficiency of 19%. However, the researchers continue to look for inexpensive, non-toxic, plentiful, and less complex materials with an appropriate bandgap for thin-film absorbents [6]. $SnSb_2S_4$ thin films seem to be potential candidates for preparing new ternary compounds as alternatives to relatively more element-based materials such as Sb, sulfosalt, and new semiconductors. However, they have not been widely studied [7]. The SnSbS system has been recently explored in photovoltaics. The research aims to develop non-toxic materials, synthesized with simple technology and in a cost-effective way for solar cell production [8]. SnSbS attracts attention as a semiconductor with a low and direct bandgap, which can be applied in many technological fields, including photovoltaics, thermoelectric energy conversion, X-ray detectors, optics, and various sensor types, optical fibers thin-film solar films [1, 9].

Renewable energy sources are critical because of the adverse environmental conditions resulting from dependency on fossil fuels. Hence, energy storage technologies like supercapacitors and lithium-ion batteries attract attention due to the high performance expected in portable electronic and electric vehicles.

Fan et al. produced PVDF-HFP/BMIMI/CNTs IGE supercapacitor, an all-solid-state supercapacitor (ASSC), to overcome problems due to liquid electrolyte of the supercapacitors, i.e., electrolyte leakage. They used carbon nanotubes (CNTs) and ion gel electrolyte (IGE) based on redox-active ionic liquid containing 1-butyl-3-methylimidazolium iodide (BMIMI) IL, poly(vinylidene fluoride-co-hexafluoropropylene) (PVDF-HFP), achieving 50.1 $Whkg^{-1}$ energy density [10]. Gu et al. produced asymmetric supercapacitor with N-doped rGO/NiSe2 composites by two-step process; the specific capacitance they reported at 1 A g^{-1} was 2451.4 F g^{-1} [11]. The hybrid micro supercapacitor's (MSC) power and energy densities are high; Li et al. designed the anode as a $Ti_3C_2T_x$ MXene-based electrode and battery-type cathode as a vanadium pentoxide (V_2O_5)-based electrode, then produced a hybrid micro supercapacitor of zinc-ion (ZIHMSC). The efficiency was ~77% after 10,000 cycles, specific

capacitance under 0.34 mA cm^{-2} was 129 mF cm^{-2}, and the energy density at 673 μW cm^{-2} was 48.9 μWh cm^{-2} [12]. He et al. achieved a specific capacitance of 3490 mF cm^{-2} at 2 mA cm^{-2} with the supercapacitor they produced from C/NiMn-LDH/Ni_3S_2 on nickel foam (NF) by using the superior properties of double-layer hydroxide (LDH) [13]. For the Ni/Co-MOF electrode obtained by hydrothermal treatment, the capacitance conservation that Zhang et al. achieved with a specific capacitance of 568 C g^{-1} was 82.6% after 6000 charge/discharge cycles [14]. The Ni_3S_4/CuS_2 nanocomposite supercapacitor electrode He et al. produced using transition metal sulfides had 888 Fg^{-1} specific capacitance and 49.68 Wh kg^{-1} energy density at 1 A g^{-1} [15]. Again, Zhang et al. achieved 583 and 365.7 Cg^{-1} at 1 and 30 Ag^{-1}, with the supercapacitor produced with Ni-Co-P/PO_x/C nanolayers having an advantage of using transition metal phosphates in energy storage devices with their high electrical conductivity. The study is remarkable with the reported 37.59 Wh kg^{-1} as energy density [16]. The critical factors for new electrode materials are long life, extended capacity, and high cycling. Being metal-based, Sn, Sb, and SnSb are the best candidates for lithium-ion batteries (LIBs) [9,17-20]. For LIBs, the theoretical capacity of Sn-based materials is 990 $mAhg^{-1}$, quite promising for anode materials [21,23].

Nevertheless, the very high volume change experienced during charge-discharge causes material deterioration, negatively affecting the cycle life and application potential [24]. However, Sn-based intermetallic alloys, i.e., Sn-Sb, overcome these problems [25-27]. Sn and Sb's ability to store lithium ions and their cascade lithium docking mechanism, which contributes to the specific capacity, may prevent volume expansion. It also increases the electrode's mechanical stability so that the electrochemical performance of SnSb alloy is better than Sn or Sb alone [28-33]. Many factors may change these materials' structural, optical, and morphological properties, including substrate temperature, preparation method, film thickness, and annealing temperature.

As reported in the literature, no attempt has been made so far to provide a detailed analysis of the impact of the deposition temperature on SnSbS thin films' capacitance properties using in-plane time-dependent I-V measurements. In the current study, SnSbS (sulfosalt) thin films were formed on glass at 20°C, 40°C, 60°C, and 80°C via CBD. The structural features of the final products were investigated with XRD, the surface morphologies with AFM and FESEM, and EDX was used for composition analysis. Capacitance properties were based on time-dependent I-V measurements.

2. EXPERIMENTAL PROCEDURE

0.0456 g ($2x10^{-4}$ mole) Antimony Chloride ($SbCl_3$) solid was dissolved in 20 ml methanol (CH_3OH). 0.048 g ($2x10^{-4}$ mole) of Sodium Sulfide (Na_2S) solid was dissolved in 20 ml methanol (CH_3OH) in a second beaker. 0.0379 g ($2x10^{-4}$ mole) of Tin Chloride ($SnCl_2$) solid was dissolved in 20 ml methanol (CH_3OH). These baths were held in separate beakers. The process was performed to shorten the dissolution time. SnSbS solution was made ready by mixing the solutions in these three beakers. The substrates were cleaned and dried substrates were weighed on a precision balance. A different bath was prepared for each deposition temperature. Glass substrates were immersed in chemical baths and separately put in ovens at 20°C, 40°C, 60°C, and 80°C, for 1 hour. Afterward, we removed the samples from the bath, left them to dry, then weighed on the precision balance to note the weight of the coated films.

X-ray figures were obtained by X-ray diffraction (XRD) with a $CuK\alpha_1$ radiation source (Rigaku Ultima IV model, λ=1.5406 Å) over the range of $10°<2\theta<90°$ at a speed of 3° min^{-1} with a step size of 0.02°. The samples' 2D surface morphology was determined by FESEM (Carl Zeiss Ultra Plus Gemini), and an EDX attached to FESEM was used for composition analysis. The films' thickness, surface roughness, and 3-D surface morphology were determined with AFM (Veeco Multimode 8). Time-dependent I-V characterizations were performed with Keithley 2400 Sourcemeter apparatus, at -0.3 and 0.9 V range, and scanning ratios of 10 mV/s, 25 mV/s, and 50 mV/s. The probes having a radius of 0.5 mm were used in the measurements; the distance between them was 1 mm. The specific capacitance of each sample was computed using the in-plane time-dependent I-V method.

3. RESULTS AND DISCUSSION

3.1. Structural & Surface Properties and Composition of $Sn_3Sb_2S_6$ Thin-Film Electrodes

XRD diffraction peaks obtained at 2q=10°-90° of SnSbS thin-film electrodes deposited at 20°C, 40°C, 60°C and 80°C are given in Figure 1. At room temperature (~20°C), XRD diffraction patterns of SnSbS structures deposited at 20°C, 40°C, 60°C and 80°C showed homogeneous $Sn_3Sb_2S_6$ (JCPDS, card no. 38-0826) crystal structures with Miller index (4 1 6) at 2q=31.80°. This $Sn_3Sb_2S_6$ crystal structure did not undergo any phase change at different temperatures. Although the thermal energy of the atoms increased with the temperature increase, they continued to be oriented in a stable position. Surprisingly, $Sn_3Sb_2S_6$ crystals were also formed at low temperatures (20°C-40°C), even though semiconductor materials produced by the chemical bath deposition show a dominant amorphous structure.

Similar to the $Sn_2Sb_2S_5$ crystals belonging to the same sulfosalt family, $Sn_3Sb_2S_6$ crystals crystallized at low temperature, which is an exception. Larbi et al. [34] investigated the impact of substrate temperature on the formation of $Sn_3Sb_2S_6$ thin films on the glass substrate. The results are similar to the crystal structures in this study.

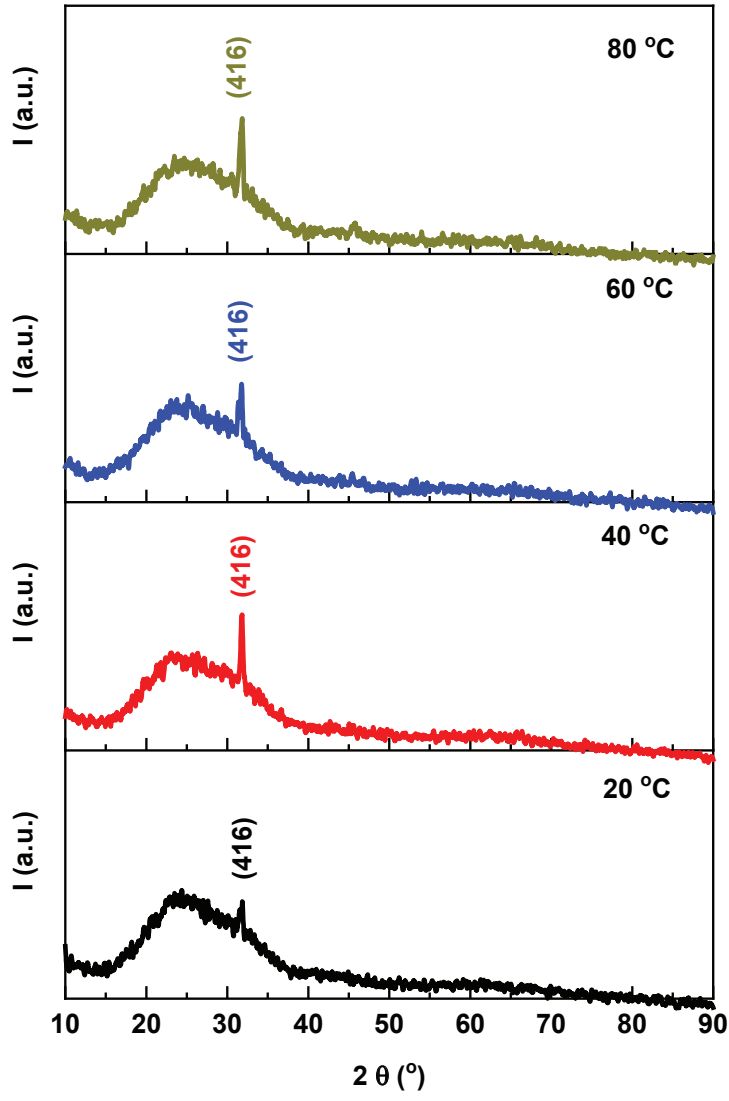

Figure 1. *XRD diffraction patterns of $Sn_3Sb_2S_6$ thin films.*

In addition, deposition temperatures affect the crystals' average grain size (D), which is calculated from Scherrer's equation [35].

$$D = \frac{0.9\lambda}{\beta \cos\theta} \tag{1}$$

D is the mean grain size, l X-ray wavelength, b half-width of the most intense peak, and θ Bragg diffraction angle. The dislocation intensity (δ) is given below in equation 2 [35].

$$\delta = \frac{1}{D^2}(4)\delta = \frac{1}{D^2}(4)\delta = \frac{1}{D^2} \tag{2}$$

Crystallization per unit area is given by equation 3 below [35].

$$N = \frac{t}{D^3} \tag{3}$$

N is the crystallization/unit area, t film thickness, and D average grain size. Structural features of $Sn_3Sb_2S_6$ thin-film structures are shown in Figure 2 and Table 1.

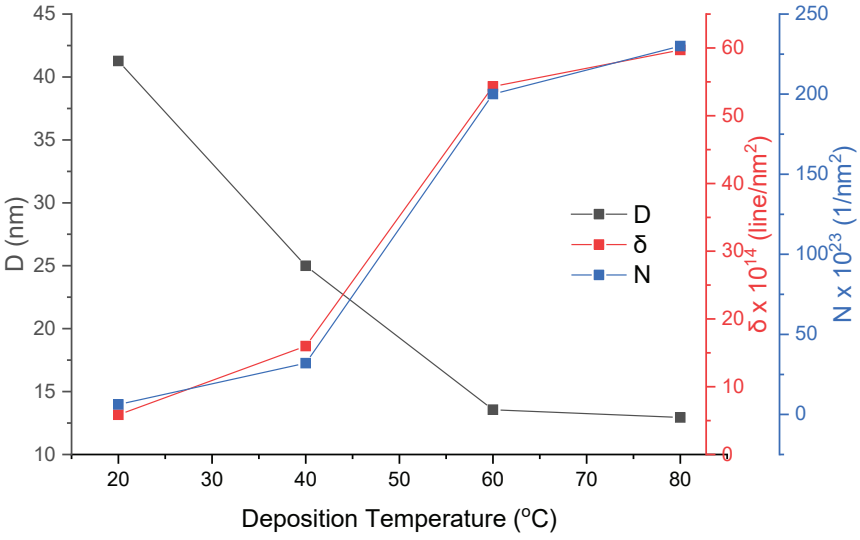

Figure 2. *Structural properties of $Sn_3Sb_2S_6$ crystals.*

Table 1. Structural properties of $Sn_3Sb_2S_6$ crystals formed at 20°C, 40°C, 60°C, and 80°C.

Deposition Temperature (°C)	D (nm)	δ (line/nm^2)	N (1/nm^2)
20	41.27	5.86 X 10^{14}	6.25 x 10^{23}
40	24.99	16.0 x 10^{14}	32.0 x 10^{23}
60	13.56	54.3 x 10^{14}	200 x 10^{23}
80	12.94	59.7 x 10^{14}	230 x 10^{23}

Accordingly, $Sn_3Sb_2S_6$ crystals' average grain size (D) decreased as temperature increased. In contrast, dislocation intensity (δ) and crystallization per unit area (N) increased. With temperature increase, the dislocations in the grain climb towards the grain boundaries, and some impurities leave the distorted lattice structure and move towards the grain boundaries, which are high-energy zones. As a result, the average grain size decreases.

Regarding the two-dimensional surface morphology of $Sn_3Sb_2S_6$ thin-film electrodes at 30.000x and 150.000x magnification, a homogeneous crystallization in the form of a network of small spherical balls or the appearance of pumice was observed at 20 °C. After 40 °C, crystallization in the form of sugar cubes also appeared in the small spherical ball network. The films were densely packed/clustered without cracks on the surface and formed porous structures similar to pumice stone. Besides, regarding structural features in Table 1 and Fig.2, the grain size decreases, and crystallization per unit area increases with deposition temperature.

FESEM images and EDX characterization of $Sn_3Sb_2S_6$ thin-film electrodes formed at 20°C, 40°C, 60°C, and 80°C are shown in Fig.3.

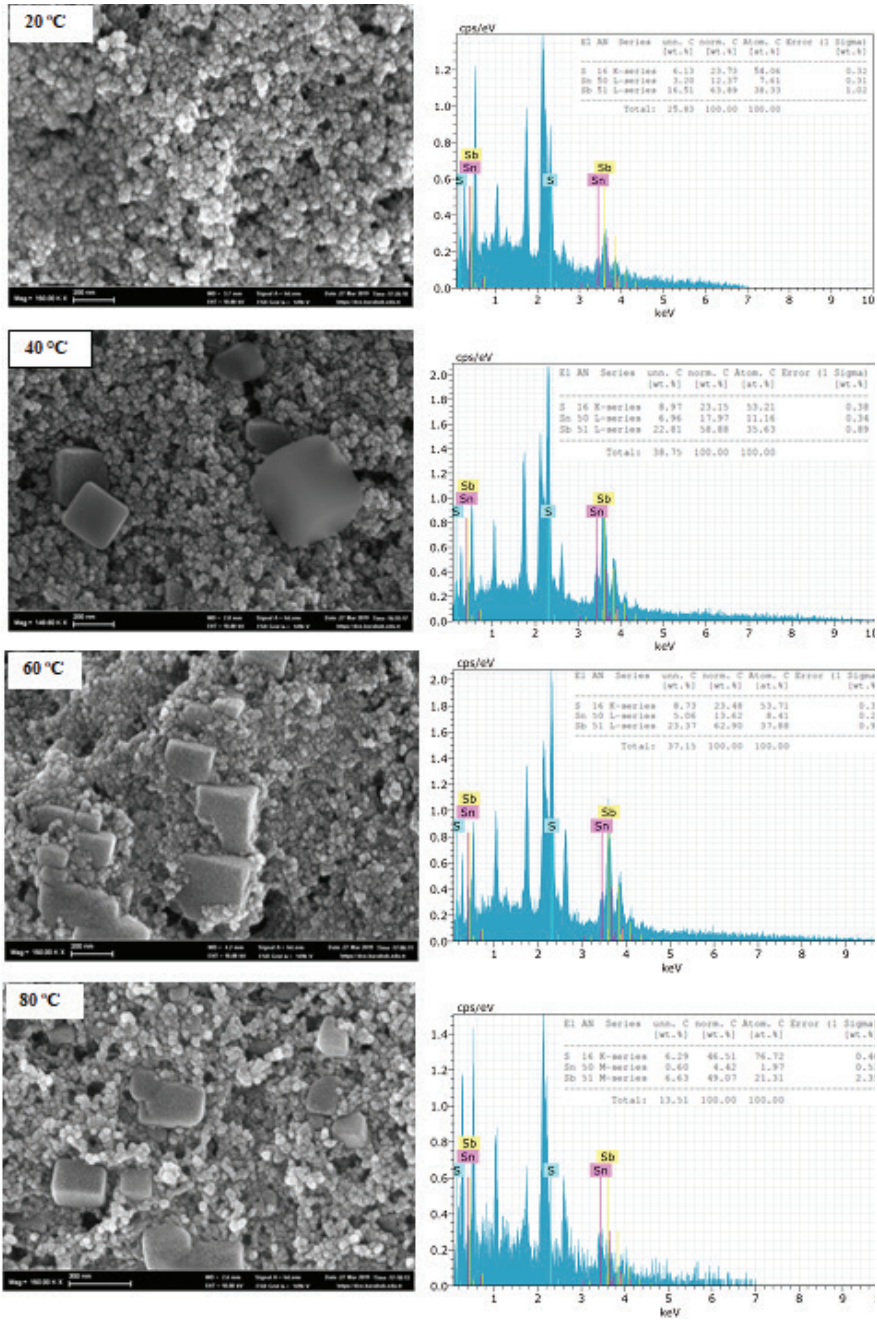

Figure 3. *FESEM images and EDX characterization of $Sn_3Sb_2S_6$ thin-film electrodes.*

Surface roughness of $Sn_3Sb_2S_6$ thin-film electrodes occured at 20°C, 40°C, 60°C and 80°C were measured as 67.82; 91.34; 102.50 and 194.05 nm, and their film thicknesses as 126.51, 132.95, 189.02, and 278.65 nm, respectively. Accordingly, both surface roughness and film thickness increased with deposition temperature.

3-D AFM images and 2-D surface roughness of $Sn_3Sb_2S_6$ thin-film electrodes formed at 20°C, 40°C, 60°C, and 80°C are shown in Fig.4.

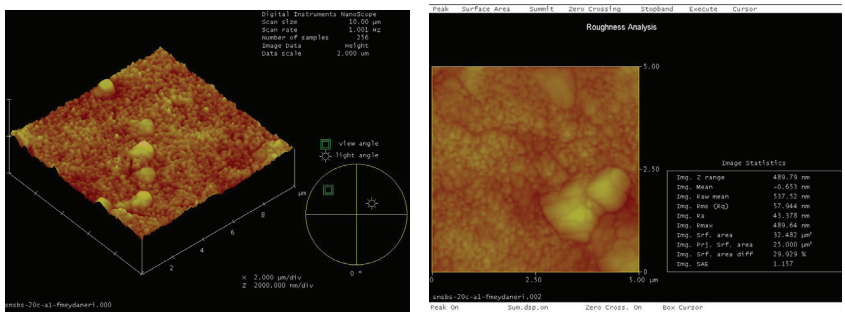

(a)

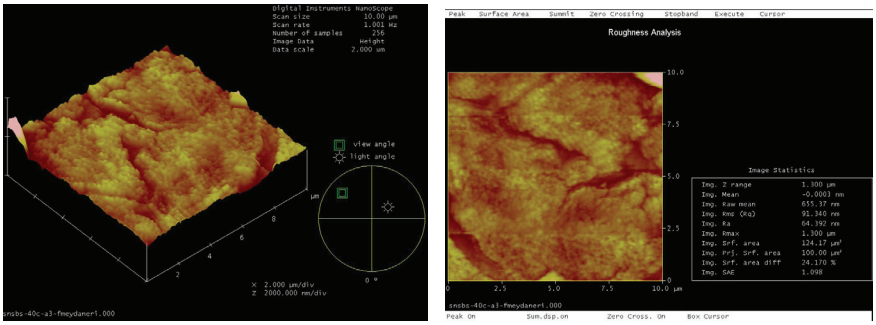

(b)

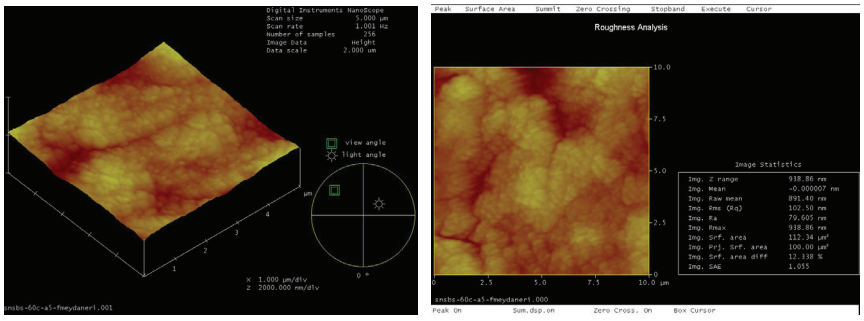

(c)

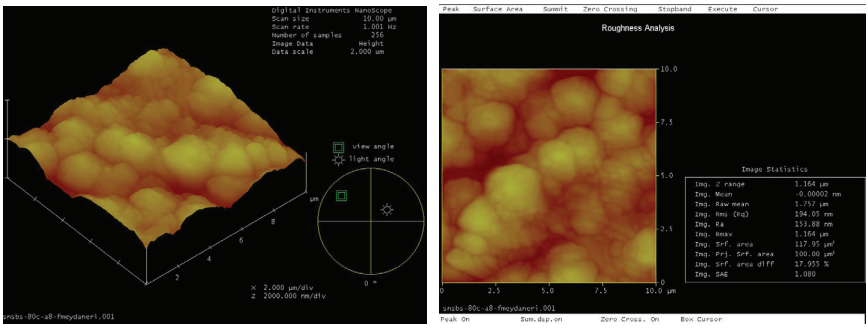

(d)

Figure 4. *AFM Analysis of $Sn_3Sb_2S_6$ thin-film electrodes;* **a)***20°C* **b)***40°C* **c)***60 °C* **d)***80 °C.*

3.2. Capacitance Properties of $Sn_3Sb_2S_6$ Thin Film Electrodes

Capacitances of $Sn_3Sb_2S_6$ thin-film electrodes were recorded with Keithley 2400 SourceMeter and Kickstart program using in-plane time-dependent I-V method; it only allows the calculation of the electrode's capacitance. The probe's radius was 0.5 mm, the distance between them was 1 mm, and the seal was taken gently. All measurements were performed between -0.3 to 0.9 volts, at scanning rates of 10, 25, and 50 mV/s, at room temperature, and in the dark. The amounts of $Sn_3Sb_2S_6$ thin film coated on glass substrates at different temperatures were measured with a precision balance and used to calculate capacitances from Equation 4 from time-dependent I-V measurements and the weight of the coated film. Cyclic voltammetry curves of $Sn_3Sb_2S_6$ thin-film electrodes are shown in Fig. 5 for each scanning rate, and their specific capacitances are shown in Table 2.

$$C_S = \frac{I}{m.\frac{dV}{dt}} \tag{4}$$

C_S is the capacitance (F/g), I the current (A), and m mass of coated film (g). The masses of $Sn_3Sb_2S_6$ films coated at 20°C, 40°C, 60°C, and 80°C are $4.02x10^{-05}$, $2.68x10^{-04}$, $7.02x10^{-06}$ and $2.33x10^{-05}$, respectively. The capacitance of $Sn_3Sb_2S_6$ thin-film is not available in the literature; thus, no comparison could be performed.

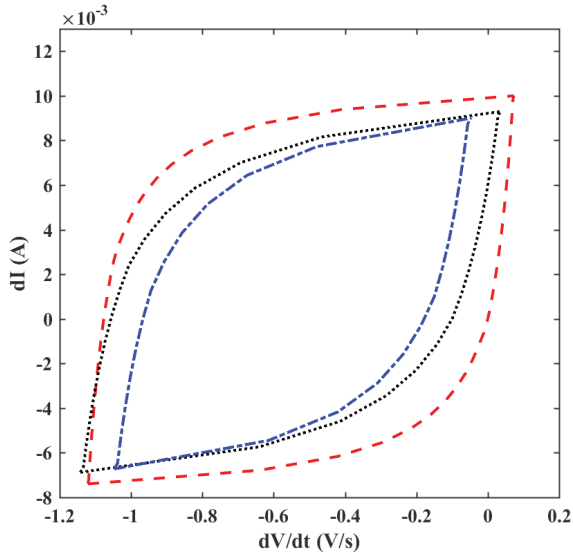
×10-3
12
10
8
6
4
2
0
-2
-4
-6
-8
dI (A)
-1.2
-1
-0.8
-0.6
-0.4
-0.2
0
0.2
dV/dt (V/s)

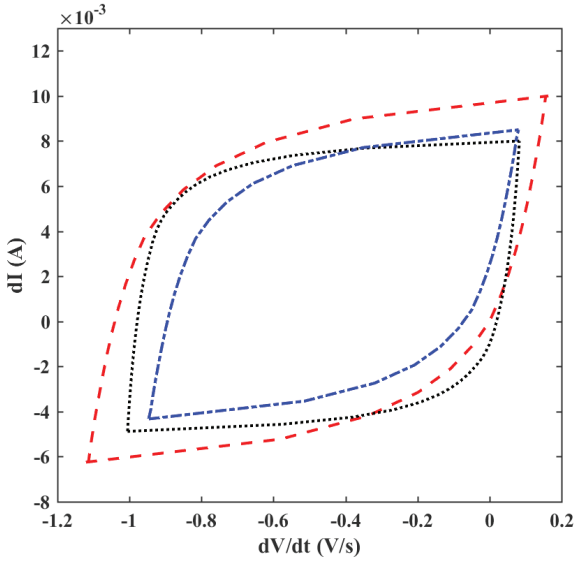
×10-3
12
10
8
6
4
2
0
-2
-4
-6
-8
dI (A)
-1.2
-1
-0.8
-0.6
-0.4
-0.2
0
0.2
dV/dt (V/s)

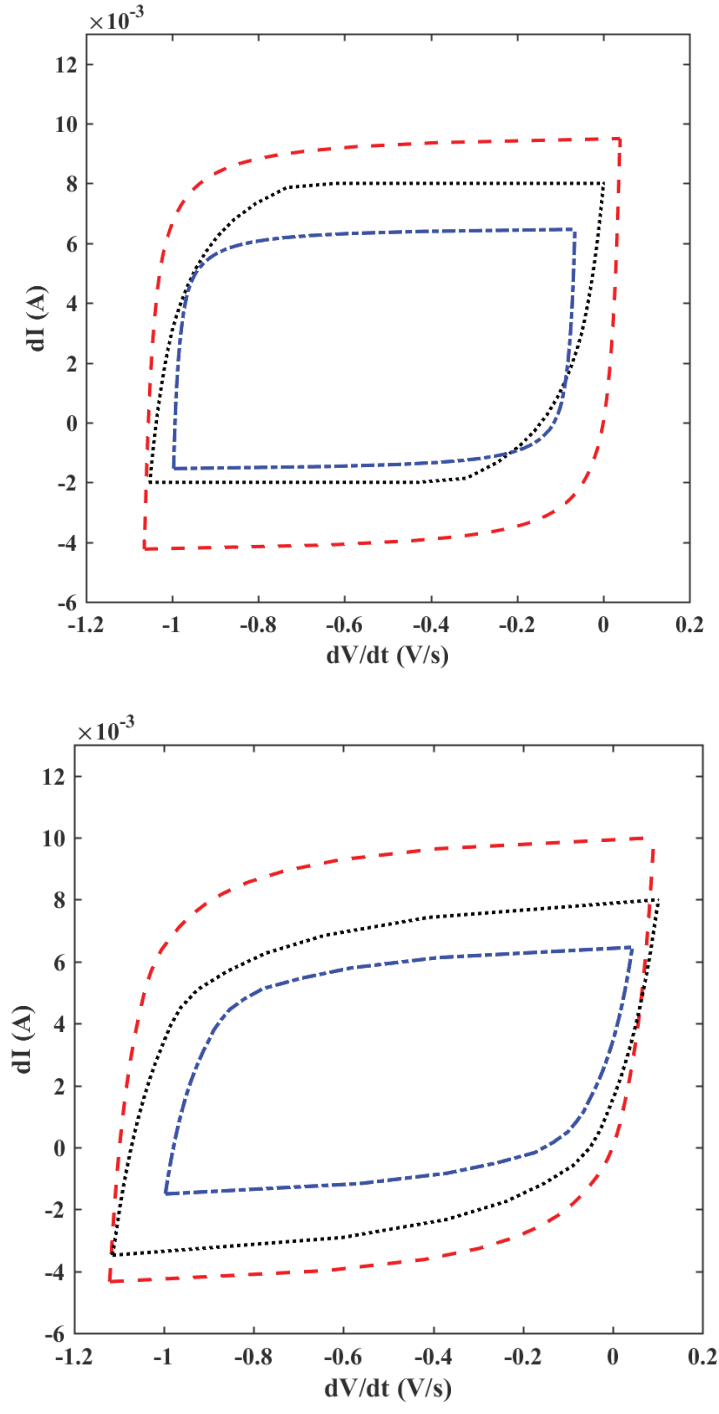

Figure 5. *Cyclic voltammetry curves of $Sn_3Sb_2S_6$ thin-film electrodes at 20°C ; 40°C ; 60°C ; 80°C.*

Table 2. *Specific capacitances of $Sn_3Sb_2S_6$ thin-film electrodes deposited at 20°C, 40°C, 60°C, and 80°C according to the scanning rates.*

	Scan Rate (mV/s)	C, Specific Capacitance (F/g)		Scan Rate (mV/s)	C, Specific Capacitance (F/g)
20 °C	10	367	60 °C	10	208
	25	202		25	148
	50	148		50	79.1
40 °C	Scan Rate (mV/s)	C, Specific Capacitance (F/g)	80 °C	**Scan Rate (mV/s)**	**C, Specific Capacitance (F/g)**
	10	335		10	16 2
	25	195		25	95
	50	117		50	50.2

3.3. Optical Properties

Regarding thin films' optical properties, their absorption (A) and transmittance (T) were measured in a UV-VIS spectrometer, and their reflectance (R%) and transmittance (T%) were calculated from equation (5). The graphs of T% and R% at different deposition temperatures are given in Figure 6.

$$T = (1-R)^2 e^{-A} \tag{5}$$

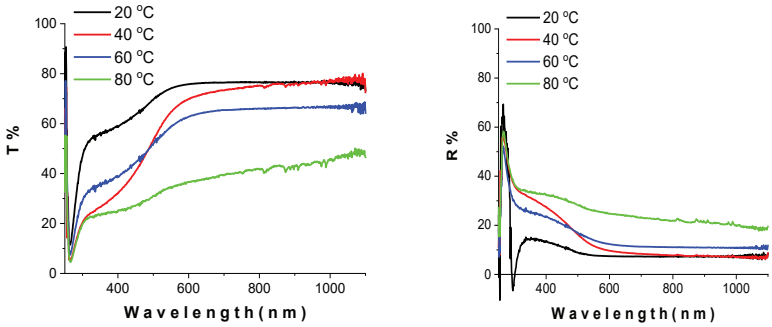

(a) *(b)*

Figure 6. *$Sn_3Sb_2S_6$ thin-film electrodes'* **a)** *T% and* **b)** *R% according to the wavelength.*

According to Fig. 6, a severe decrease was observed after 592 nm wavelength. The transmittance of the films formed at 20°C and 40°C was the same up to this wavelength and above 870 nm wavelengths. Below 870 nm, the transmittance of the films deposited at 40 °C was lower. In general, the transmittance decreases as deposition temperature increases due to the increase in film thickness as the deposition temperature increases (126.51; 132.95; 189.02 and 278.65 nm for 20°C, 40°C, 60°C and 80°C, respectively). The film absorbs more light as the thickness increases.

A proportional increase was observed in transmittance with the deposition temperature (see equation 5). A high reflectance value of 69% was achieved at 264 nm wavelength. These highly reflective films can be used as reflective materials in optoelectronics. Viruses and microbes in the UV-C region can be purified from the desired areas with the LEDs produced with such reflective materials [36].

The absorption of the films is given in Fig. 7. As expected, the thickest film produced at 80°C had the highest absorbance (1.33). Interestingly, an absorption peak was observed at 295 nm in the film deposited at 20 °C. This is because of lower crystallization and larger particles than other films; and most importantly, cubic structures are observed in other films, whereas the films deposited at 20°C have a spherical particle structure.

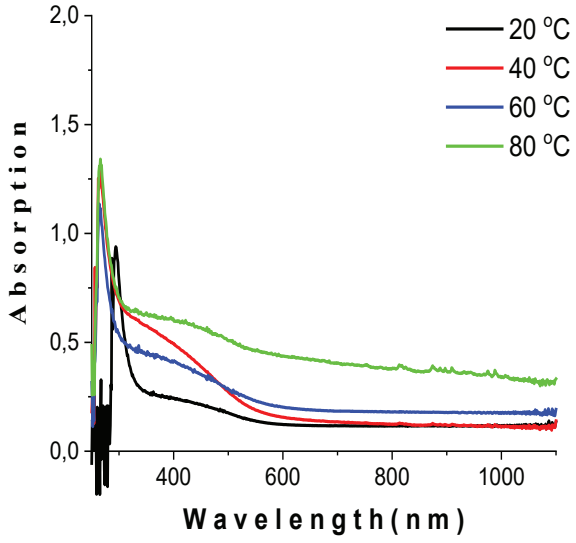

Figure 7. *Absorption variation of $Sn_3Sb_2S_6$ thin-film electrodes according to wavelength.*

The films' refractive index and extinction coefficient were determined from equations 6 and 7.

$$n = \frac{1+R}{(1-R)} + \sqrt{\frac{4R}{(1-R)^2} - k^2} \qquad n = \frac{(1+R)}{(1-R)} + \sqrt{\frac{4R}{(1-R)^2} - k^2} \quad (6)$$

$$k = \frac{\hat{\alpha}}{4\pi} \quad (7)$$

Here, $\alpha\alpha$ is the absorption coefficient, λ wavelength, n refractive index, and k extinction coefficient. In Figure 8, the films' refractive index and extinction coefficient are shown. Again, the most exciting result was found in the refractive index due to absorption. The film deposited at 20°C had a maximum refractive index of around 11 at the wavelength of 264 nm, a noticeable difference compared to the films deposited at different temperatures. According to the literature, the films with such a high refractive index at these wavelengths are very suitable for high-sensitivity refractive index sensors [37] and used in excimer lasers [38].

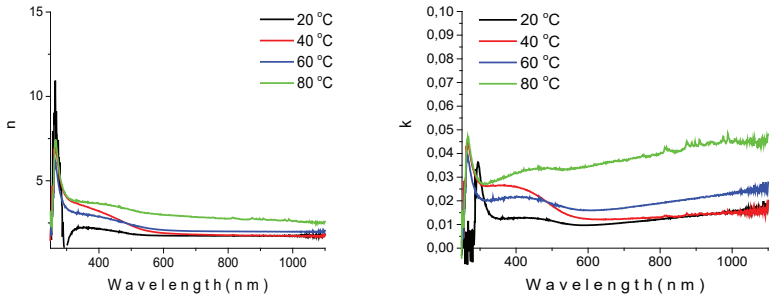

(a) *(b)*

Figure 8. Change of **a)** refractive index (n) and **b)** extinction coefficient (k) of $Sn_3Sb_2S_6$ thin-film electrodes according to wavelength.

The optical parameters ε_1 and ε_2, which show how the films are affected by electromagnetic waves, were calculated with the following equations.

$$\varepsilon = \varepsilon_1 + i\varepsilon_2 \quad (8)$$

$$\varepsilon_1 = n^2 - k^2 \quad (9)$$

$$\varepsilon_2 = 2nk \quad (10)$$

According to Figure 9, the ε_1 value of the film formed at 20 °C has the highest value, close to 30. In contrast, it has the lowest ε_2 value compared

to the films deposited at different temperatures. Such materials with high dielectric value are the best materials for use in structures such as MOS-FET in technology [39].

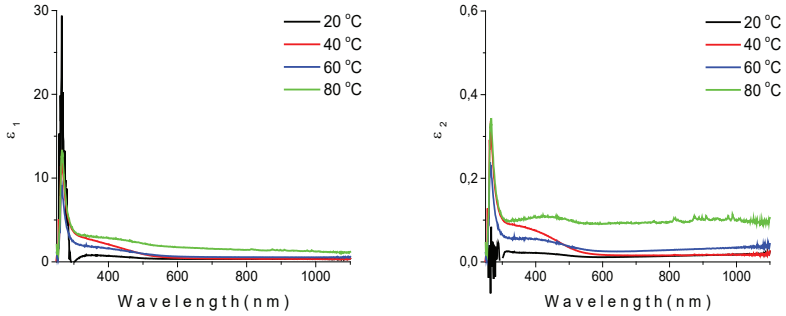

(a) *(b)*

Figure 9. Variation of **a)** Real (ε_1) and **b)** Virtual (ε_2) Dielectric coefficient of $Sn_3Sb_2S_6$ thin-film electrodes according to wavelength.

The following relation was used to obtain optic bandgap energy (Eg) of the films (11):

$$(\alpha h\upsilon) = A(h\upsilon - E_g)^n \qquad (11)$$

A is a constant, α absorption coefficient, hν the photon energy, and n is a constant equal to ½ for direct bandgap semiconductor.

The films' optical bandgaps are given in Figure 10. Optical bandgaps of the films formed at 20°C, 40°C, 60°C, and 80°C were found to be 1.97, 1.98, 1.91, and 1.85 eV, respectively.

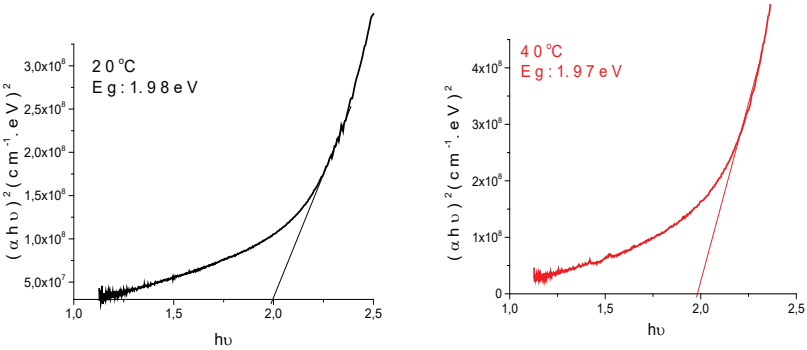

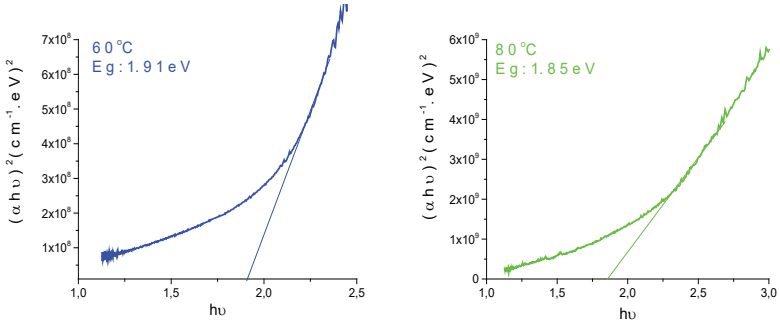

Figure 10. *E_{gap} values of $Sn_3Sb_2S_6$ thin-film electrodes.*

The reason why the optical bandgaps decrease with the increase of the deposition temperature can be understood from equation 11. The optical bandgap is inversely proportional to absorbance. Thicker films have a higher absorbance. Therefore, a decrease was observed in optical bandgaps of the produced films according to the deposition temperature [40]. Thin films with this optical bandgap can be used in solar cells.

4. CONCLUSION

$Sn_3Sb_2S_6$ thin films with cubic and spherical particles have been produced for the first time in the literature. The films were produced by the CBD method, which is low-cost and easy to perform. The films' optical, structural, and capacitor properties were analyzed. The optical properties of the film deposited at low temperature (20°C) were particularly striking. They are very suitable for LED products used to purify viruses and microbes, high-sensitivity refractive index sensors, excimer lasers, solar cells, and supercapacitors.

ACKNOWLEDGEMENT

Karabük University Scientific Research Project Unit supported this work under Project Numbers: KBÜBAP-21-DS-012. The authors would like to thank the KBU-BAP.

REFERENCES

[1] H. Dittrich, A. Stadler, D. Topa, H.J. Schimper, A. Basch, Progress in sulfosalt research, Phys.Status Solidi A-Appl. Mat. 206 (2009) 1034-1041.

[2] S.A. Manolache, A. Duta, L. Isac, M. Nanu, A. Goossens,J. Schoonman, The influence of the precursor concentration on $CuSbS_2$ thin films deposited from aqueous solutions, Thin Solid Films 515 (2007) 5957-5960.

[3] T. Wagner, M. Krbal, P. Nemec, M. Frumar, Th Wagner, M. Vlcek,V. Perina, A. Mackova, V. Hnatovitz, S.O. Kasap, $AgAsS_2$ amorphous chalcogenide films prepared by pulsed laser deposition, Appl. Phys. 79 (2004) 1563-1565.

[4] J. Gutwirth, T. Wagner, P. Nemec, S.O. Kasap, M. Frumar, Thermal and optical properties of $AgSbS_2$ thin films prepared by pulsed laser deposition (PLD), J. Non-Cryst. Solids 354 (2008) 497-502.

[5] I. Mellouki, A. Mami, N. Bennaji, Y. Fadhli, Study of doping and annealing effects on thermal properties of $Sn_xSb_2S_y$ ($1 \leq x \leq 3$, $4 \leq y \leq 6$) sulfosalts thin films by electro-pyroelectric technique, Thermochimica Acta 670 (2018) 123–127.

[6] B. Ismail, S. Mushtaq, R. A. Khan, A. M. Khan, A. Zeb, A. R. Khan, Enhanced grain growth and improved optical properties of the Sn doped thin films of Sb_2S_3 orthorhombic phase, Optik 125 (2014) 6418–6421.

[7] A. Gassoumi, M. Kanzari, Growth and post-annealing effect on the properties of the new sulfosalt $SnSb_2S_4$ thin films, Physica E 44 (2011) 71–74.

[8] D. Abdelkader, F. Chaffar Akkari, N. Khemiri, B. Gallas, F. Antoni, M. Kanzari, Structural and spectroscopic ellipsometry studies on vacuum evaporated $Sn_{2m-4}Sb_4S_{2m-2}$ (m = 2.5, 3 and 4) thin films deposited on glass and Si substrates, Journal of Alloys and Compounds 646 (2015) 1049-1057.

[9] M. Armand, J.-M. Tarascon, Building Better Batteries, Nature 451 (2008) 652–657.

[10] L.Q. Fan, Q.M. Tu, C.L. Geng, Y.L. Wang, S.J. Sun, Y.F. Huang, J.H. Wu, Improved Redox-Active Ionic Liquid-Based Ionogel Electrolyte by Introducing Carbon Nanotubes for Application in All-Solid-State Supercapacitors, Int. J. Hydrog. Energy 45 (2020) 17131–17139.

[11] Y. Gu, L.Q. Fan, J.L. Huang, C.L. Geng, J.M. Lin, M.L. Huang, Y.F. Huang, J.H. Wu, N-doped reduced graphene oxide decorated $NiSe_2$ nanoparticles for high-performance asymmetric supercapacitors, Journal of Power Sources 425 (2019) 60-68.

[12] X. Li, Y. Ma, Y. Yue, G. Li, C. Zhang, M. Cao, Y. Xiong, J. Zou, Y. Zhou, Y. Gao, A flexible Zn-ion hybrid micro-supercapacitor based on MXene anode and V_2O_5 cathode with high capacitance, Chemical Engineering Journal, 428 (2022) 130965.

[13] Y. He, D. Liu, H. Zhao, J. Wang, Y. Sui, J.Qi, Z. Chen, P. Zhang, C. Chen, D. Zhuang, Carbon-coated NiMn layered double hydroxides/Ni_3S_2 nanocomposite for high-performance supercapacitors, Journal of Energy Storage 41 (2021) 103003.

[14] X. Zhang, J. Wang, X. Ji, Y. Sui, F. Wei, J. Qi, Q. Meng, Y. Ren, Y. He, Nickel/cobalt bimetallic metal-organic frameworks ultrathin nanosheets with enhanced performance for supercapacitors, Journal of Alloys and Compounds 825 (2020) 154069.

[15] Y. He, X. Zhang, S. Wang, J. Meng, Y. Sui, F. Wei, J. Qi, Q. Meng, Y. Ren, D. Zhuang, Rubik's cube-like Ni_3S_4/CuS_2 nanocomposite for high-performance supercapacitors, Journal of Alloys and Compounds 847 (2020) 156312.

[16] X. Zhang, J. Wang, Y.Sui, F. Wei, J. Qi, Q. Meng, Y. He, D. Zhuang, Hierarchical Nickel−Cobalt Phosphide/Phosphate/Carbon Nanosheets for High-Performance Supercapacitors, ACS Appl. Nano Mater. 3 (2020) 11945–11954.

[17] J. Chen, F. Cheng, Combination of Light weight Elements and Nanostructured Materials for Batteries, Accounts Chem. Res. 42 (2009) 713–723.

[18] H. Wu, G. Yu, L. Pan, N. Liu, M.T. McDowell, Z. Bao, Y. Cui, Stable Li-ion battery anodes by in-situ polymerization of conducting hydrogel to conformally coat silicon nanoparticles, Nat. Commun. 4 (2013) 1943.

[19] Y. Zou, Y. Wang, Sn@CNT Nanostructures Rooted in Graphene with High and fast Li-Storage Capacities, ACS Nano 5 (2011) 8108–8114.

[20] M. He, K. Kravchyk, M. Walter, M.V. Kovalenko, Monodisperse Antimony Nanocrystals for High-Rate Li-ion and Na-ion Battery Anodes: Nano versus Bulk, Nano Letters 14 (2014) 1255–1262.

[21] Z. Yi, Q. Han, D. Geng, Y. Wu, Y. Cheng, L. Wang, One-pot chemical route for morphology-controllable fabrication of Sn-Sb micro/nano-structures: Advanced anode materials for lithium and sodium storage, J. Power Sources 342 (2017) 861-871.

[22] D. Lakshmi, B. Nalini, P. Sivaraj, S. Jayapandi, Electro analytical studies on indium incorporated SnS balloy anode for Li-ion batteries, J. Electroanal. Chem. 801 (2017) 459-465.

[23] G. Zhang, J. Zhu, W. Zeng, S. Hou, F. Gong, F. Li, C.C. Li, H. Duan, Tin quantum dots embedded in nitrogen-doped carbon nanofibers as excellent anode for lithium-ion batteries, Nano Energy 9 (2014) 61-70.

[24] M. He, M. Walter, K.V. Kravchyk, R. Erni, R. Widmer, M.V. Kovalenko, Monodisperse SnSb nanocrystals for Li-ion and Na-ion battery anodes: synergy and dissonance between Sn and Sb, Nanoscale 7 (2015) 455-459.

[25] X. Dong, W. Liu, X. Chen, J. Yan, N. Li, S. Shi, S. Zhang, X. Yang, Novel three dimensional hierarchical porous Sn-Ni alloys as anode for lithium-i-

on batteries with long cycle life by pulse electrodeposition, Chem. Eng. J. 350 (2018) 791-798.

[26] P. Nithyadharseni, M.V. Reddy, B. Nalini, B.V.R. Chowdari, Electrochemical investigation of SnSb nanoparticles for lithium-ion batteries, Mater. Lett. 150 (2015) 24-27.

[27] L. Zhang, L. Lu, D. Zhang, W. Hu, N. Wang, B. Xu, Y. Li, H. Zeng, Dual-buffered SnSe@CNFs as negative electrode without standing lithium storage performance, Electrochim. Acta 209 (2016)423-429.

[28] W. Fan, X. Liu, Z. Wang, P. Fei, R. Zhang, Y. Wang, C. Qin, W. Zhao, Y. Ding, Synergetic enhancement of the electronic/ionic conductivity of a Li-ion battery by fabrication of a carbon-coated nanoporous SnOxS balloy anode, Nanoscale 10 (2018) 7605-7611.

[29] H. Wang, Q. Wu, D. Cao, X. Lu, J. Wang, M.K.H. Leung, S. Cheng, L. Lu, C. Niu, Synthesis of SnSb-embedded carbon-silica fibers via electrospinning: Effect of TEOS on structural evolutions and electrochemical properties, Materials Today Energy 1-2 (2016) 24-32.

[30] X. Xia, Z. Li, H. Zhou, Y. Qiu, C. Zhang, The effect of deep cryogenic treatment on SnSb/C nanofibers anodes for Li-ion battery, Electrochim. Acta 222 (2016) 765-772.

[31] A.T. Tesfaye, Y.D. Yücel, M.K.S. Barr, L. Santinacci, F. Vacandio, F. Dumur, S. Maria, L.Monconduit, T. Djenizian, The Electrochemical Behavior of SnSb as an anode for Li-ion Batteries Studied by Electrochemical Impedance Spectroscopy and Electron Microscopy, Electrochim. Acta 256 (2017) 155-161.

[32] X. Xia, Z. Li, L. Xue, Y. Qiu, C. Zhang, X. Zhang, The electrochemical performance of SnSb/C nanofibers with different morphologies and underlying mechanism, J. Mater. Res. 32 (2017) 1184-1193.

[33] P. Antitomaso, B. Fraisse, M.T. Sougrati, F. Morato-Lallemand, S. Biscaglia, D. Aymé-Perrot, P.Girard, L. Monconduit, Ultra-fast dry microwave preparation of SnSb used as negative electrode material for Li-ion batteries, J. PowerSources 325 (2016) 346-350.

[34] A. Larbi, H. Dahman, M. Kanzari, Effect of substrate temperature on structural and optical properties of the new high absorbent $Sn_3Sb_2S_6$ thin films, Vacuum 110 (2014) 34-39.

[35] F. Meydaneri Tezel and İ. A. Kariper, Effect of pH on the structural and optical properties of polycrystalline ZnSe thin films produced by CBD method, International Journal of Modern Physics B, 33 (2019) 1950024.

[36] M.A. Keçebaş, K. Şendur, Enhancing the spectral reflectance of refractory metals by multilayer optical thin-film coatings, Journal of the Optical Society of America B, 35 (2018) 1845-1853.

[37] C.L. Tien, H.Y. Lin, S.H. Su, High Sensitivity Refractive Index Sensor by D-Shaped Fibers and Titanium Dioxide Nanofilm, Advances in Condensed Matter Physics, 6 (2018) 2303740.

[38] A. Dragamir, D.N. Nikogosyan, G. Brambilla, Increased photosensitivity of Ge-doped and Ge, Se-doped fibers under high-intensity 264 mn laser light, Electr. Lett. 39 (2003) 1437- 1438.

[39] O. Pakma, C. Özaydın, Ş. Özden, İ.A. Kariper, Ö. Güllü, Synthesis and characterization of vanadium oxide thin films on different substrates, Journal of Materials Science-Materials in Electronics, 28 (2017) 10909-10913.

[40] İ.A. Kariper, Structural, optical and porosity properties of CdI_2 thin film, Journal of Materials Research and Technology, 5 (2016) 77-83.

Chapter 5

GAS FLOW TYPES AND JET SYSTEM IN COLLISION STUDIES

Zehra Nur OZER[1]

1 Assoc.Prof.Dr. Zehra Nur OZER, Afyon Kocatepe University,Orcid no: 0000-0002-5887-4486

Gases have different pressure values in different volumes since pV = constant according to Boyle's law. At constant temperature, a given mass of gas occupies a small volume at high pressure and a large volume at low pressure. The gas flow is caused by the pressure difference. The volume A occupied by a certain mass of gas inside the pipe progresses as in Figure 1 and occupies the volume A′ near the outer part. Pressure P is constant across any cross section.

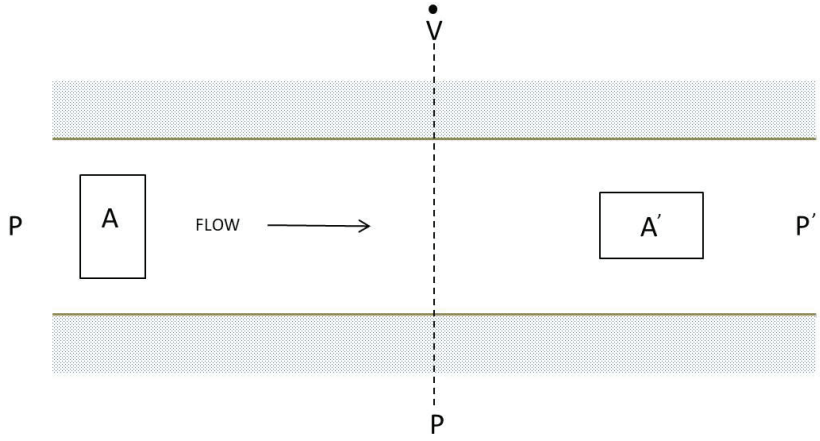

Figure 1. Gas flow in a pipe

Transmission (Q); with the pressure p, the flow rate at this pressure, that is, the gas volume per unit time, can be determined by the product $\dot{v}$.

$$Q = p.\dot{v} \qquad \text{Eq. (1)}$$

Here, since p is mbar and the volume flow rate is $\dot{v}$ liter/second, the unit of transmission is mbarliter/second. Conduction is uniform at the ends of the tube.

$$p_1.\dot{v}_1 = p_2.\dot{v}_2 \qquad \text{Eq. (2)}$$

In a vacuum system, the volumetric flow velocity $\dot{v}$ is expressed as velocity, in regions where gas enters from the vacuum chamber to the pipe as well as from the pipe to the pump. In this case, the symbol S instead of $\dot{v}$ in the formula Q = p.$\dot{v}$ used. The S^* symbol is used when examining the speed inside the pump.

In Figure 2, transmission from a vacuum chamber at p_1 pressure to a pump is shown. In the high-pressure vacuum chamber, the lower velocity S is determined by $S = Q/p_1$ while $S^* = Q/p$

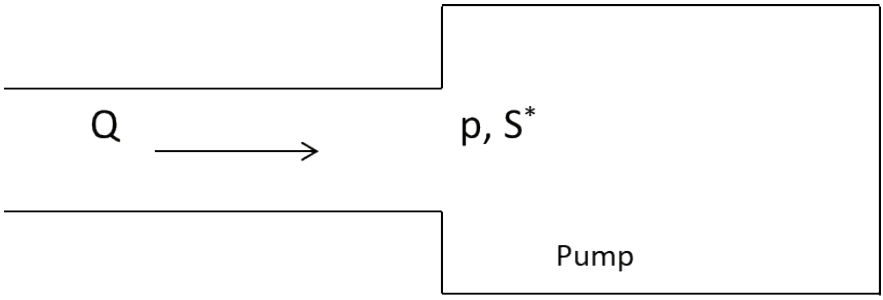

Figure 2. Conduction (from the vacuum chamber to the pump).

Conduction velocity in a pipe; (p_1-p_2) being the pressure difference between the inner and outer regions of the pipe;

$C = Q/(p_1 - p_2)$ l/s. Eq. (3)

is determined by. Here Q is the conduction between the two ends.

If a large number of pipes of different sizes with the same pressure are used, the highest transmission (Q) and therefore the greatest transmission rate (C) is obtained. Pipes can be connected to the vacuum chamber in series or parallel.

Separation of gas flows into regions in vacuum systems is done according to three different value ranges of a dimensionless parameter called Knudsen number (K_n). The Knudsen number is defined as the ratio of the mean free path of a gas molecule to the size of the pipe through which the gas flows.

Viscous Flow:

When the mean free path is small relative to the size of the tube, collisions between molecules are more effective than collisions with the wall. Therefore, the gas environment is like continuous. Regions with a small Knudsen number are called viscous flow regions.

It is given as $K_n=1/D$, where D is the diameter of the pipe. When $K_n<10^{-2}$, viscous flow is dominant. When the pressure is reduced to 10^{-2} mbar or less, the molecule-molecule collisions are more and the gas behaves like a fluid. Molecules are ejected by pushing each other. Viscous flow occurs as a result of friction forces between molecules and the effect of viscosity.

Dimensions D and L of a pipe are effective in the viscous flow range and affect the discharge time. Suppose that the pressure zone p_1 and p_2 is separated by a hole of surface area A. through hole transmission in case $p_1 > p_2$ is given as;

$$Q = \sqrt{\frac{R.T}{2\pi M}} A.(p_1 - p_2) \qquad \text{Eq. (4)}$$

Conduction velocity through a circular hole of diameter D (cm) is given as;

$C = 9{,}3.D^2$ l/s. Eq. (5)

Here, p_1 and p_2 are the internal and external pressures, respectively $p = (p_1+p_2)/2$ is the average pressure. For this equation to be valid, there must be no irregularity in the flow, the flow velocity must be constant along the pipe, the L length must not be small, and the flow velocity at the pipe wall must be zero.

Molecular Flow:

In low pressure regions where the mean free path is large relative to the pipe size, the gas flow is limited by the collisions of the molecules against the walls, and the molecules behave as if they are independent of each other. The gas flow in this region is called molecular flow and the Knudsen number is greater than 1. When the pressure is reduced to 10^{-3} mbar or less, the mean free path of the molecules becomes 6.6 cm. Molecules flow when the diameter of the pipe is 10 cm and the mean free path is smaller than the diameter of this pipe.
Molecules can be temporarily trapped on the wall surface and, when removed again, move in random directions until they are reabsorbed. The direction of the molecule removed from the vacuum wall is not related to the direction it came from.

A molecule in a long tube tends to return to the point where it started moving, and there is no way to affect the individual molecule. Gas flow is only possible by connecting a suitable pump to the end of the pipe, trapping the molecules and preventing their return (the pump can catch the molecules while they are in motion).

In a cylindrical tube, the viscous flow rate is always greater than the molecular flow. Because there is no control mechanism over the molecular flow, only the tube geometry is important. In viscous flow, the conduction velocity can be increased by pressure variation. Short and wide pipe should be preferred for high conduction rate in molecular flow.

A transmission pipe with length L, diameter D and cross section A is shown in Figure 3. Most molecules flow molecularly when the mean free path is l>>L and l>>D in a pipe with pressures P_1 and P_2 at both ends.

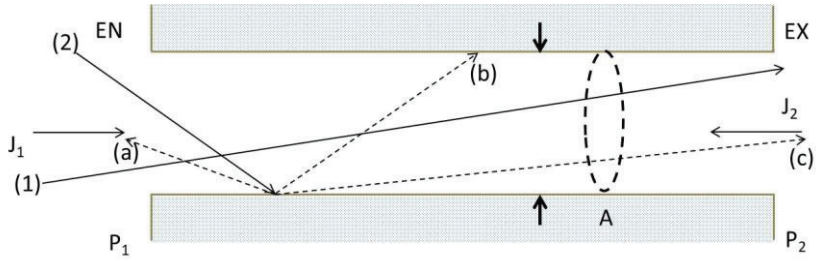

Figure 3. Molecular flow (through a pipe).

The total number of molecules passing through the EN inlet in the pipe per second is J_1.A=N. Molecules following the path indicated by (1) can pass without hitting any edge, but this event often does not happen. The molecules following the path indicated by 2) interact with the walls and move in random directions. Molecules following (2) are likely to follow paths (a), (b) and (c).

While some of the molecules will pass through the EX plane, some will return to the EN plane. The ratio of molecules exiting from the right side is denoted by the symbol W and the passed flux is determined by the expression WJ_1A. For the shorter pipe, the probability of transition W will be greater. As L increases, the probability of transition W will decrease as there will be interaction with the wall. The permeability probability of the pipe should be the same in both directions, but the J_2 flow is on the low p_2 side. So the flux passed from right to left will be WJ_2A. Net transmission is obtained by multiplying W(J_1- J_2)A by kT.

$$Q = kT(J_1 - J_2)AW \qquad \text{Eq.(6)}$$

For very long pipes (L>>D) with 1% accuracy by Knudsen

$$C_L = \frac{D^3}{6L}\sqrt{\frac{2\pi RT}{M}} \qquad \text{Eq. (7)}$$

Knudsen Flow(Transition Zone):

The region between viscous and molecular flow is called the transition zone or Knudsen flow. The mean free path and the pipe dimensions are approximately the same. In this region, both molecular and viscous flow properties are observed.

Figure 4; viscous, molecular flow, and shows the change in the transmission velocity of a pipe with a decrease in pressure in the transition zones.

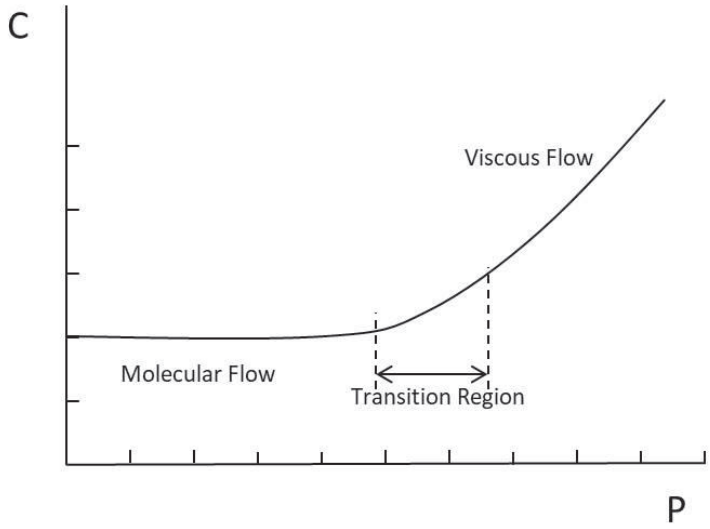

Figure 4. Transition from viscous flow to molecular flow.

JET SYSTEM FOR COLTRIMS

COLTRIMS (cold target recoil ion momentum spectroscopy) is a technique that investigates the dynamics of atom-molecule and electron-photon interaction reactions. Simply, the system consists of a cold gas jet target obtained by supersonic propagation in a vacuum, and a part that separates the momentum of ions or electrons from the gas target as a result of ionization. Target control is extremely important in the COLTRIMS system. Whenever possible, the initial momentum should be known before collision (Ozer 2007).

The general principle for atomic sources is that atoms (molecules) form a molecular or aerodynamic flow from a container to a differentially pumped region. It enables to shape a molecular light beam that intersects with another ionic or molecular light beam in the flowing gas collision circle.

Molecular (Effusive) Beam:

Atoms (molecules) will leave the gas container without any change in their velocity distribution across the slit or hole. With differential pumping, the pressure difference between the two zones will create a gas flow from the high pressure zone to the low pressure zone. If the overall pressure is low enough, the atoms or molecules will move from the high pressure region to the low pressure region without any change in their spatial and velocity distributions through the hole. This form of flow is molecular (effusive) flow.

Consider a gas container of diameter d and thickness l and a circular hole; if l~0 then d<< λ then the flow is molecular. Here λ is the mean free path of the atoms in the source. λ can be calculated for an ideal gas using kinetic theory:

$$\lambda = \frac{kT}{\sqrt{2\sigma_k P}} \quad \text{Eq.(8)}$$

Here P is the gas pressure in the weld and T is the weld temperature, k is the Boltzman Constant, σ_k is the collision cross section for atoms.

Within the solid angle dΩ, the number of atoms defined by the angle θ and flowing per unit time is given as:

$$dN = \frac{d\Omega}{4\pi} n\bar{v} A_s cos\theta \quad \text{Eq.(9)}$$

It is seen from the equation that the particles have a cosine distribution in all directions with the current. Here n is the number of atoms per unit volume in the source.

$$A_s = \pi(\frac{d}{2})^2 \quad \text{Eq. (10)}$$

is the area of the hole. v is the average particle velocity is given by (m is the mass of the particle);

$$\bar{v} = \sqrt{\frac{8kT}{\pi m}} \quad \text{Eq.(11)}$$

Integrate the equation to find the total number of particles flowing with time in all directions.

$$dN = \frac{d\Omega}{4\pi} n\bar{v} A_s cos\theta \quad \text{Eq. (12)}$$

and

$$N = \frac{1}{4} n\bar{v} A_s \quad \text{Eq. (13)}$$

is obtained.

The directionality of the flowing beam is directly proportional to the l/d factor. By increasing this ratio (giving some thickness to the hole), the directionality of molecular (effusive) flow can be increased. If l>>d, the reduction factor (ξ) is defined.

$$\xi = \frac{4d}{3l} \qquad \text{Eq.(14)}$$

and

$$N = \frac{1}{4}\xi n\bar{v}A_s = \frac{\pi d^3}{12l}n\bar{v} \qquad \text{Eq.(15)}$$

is obtained.

Two other factors that are important for limiting the size of the target are:

- Molecular flow should not only pass through a single-channel slit, but also through a 1 mm diameter strainer placed at a distance of 2.5 mm from the outlet of the pre-cooled gas cell.

- The ion beam encounters the molecular (effusive) flow at 3-4 mm of the strainer. The combination of these two factors makes it possible to limit the beam. The size of the expanded target is shaped by the intersection of the beam, and the jet can be stabilized using the focusing capabilities of the spectrometer (Freeman et al., 2012).

In order to obtain large target densities and hence large atomic beam currents, multiple gaps are arranged instead of a single gap. Each gap passes particles, thus allowing a large number of particles to pass through the source.

Capillaries are usually made of glass. Its dimensions can be between d=30μm-1 mm and l=300μm-10 mm (Abdallah, 1997). In this case, the number of flowing particles, N_{ya} being the number of gaps on the surface;

$$N = N_{ya}\frac{\pi a}{12l}n\bar{v} \qquad \text{Eq.(16)}$$

Supersonic Atomic Beam:

In this case, the dense gas is passing through a very narrow hole. It is the situation where the pressure difference between the source and target region is too great. Therefore, the boundary condition is d>>λ. It results in many atom-atom and atom-wall collisions before the particles escape

the hole. These conditions result in thermal cooling, where random motion of particles is converted into energy downstream.

The jet envelope is elongated in shape and elliptical in the direction of the gas flow. The thermal cooling and shock wave of the expanding gas combined with the strainer to show the elliptical spread of the gas provide a directional flow and a dense target. This depends on the superposition of the directional velocities of the jet and the flow rate. After a distance of l_s, the particles pass through the filter. The skimmer allows only the particles in the center (inner part) to pass through.

The role of the skimmer,

- Adding directionality to the atomic beam.
- Throwing off the slow parts of the jet envelope.
- Reducing the number of particles dispersed in the collision chamber that is, cooling the gas geometrically.

The strainer is generally conical in shape, which contributes to reducing the effect of particles dispersed across the nozzle in the gas-jet stream. Another parameter that is important in describing the supersonic gas flow is the Mach number (M). The Mach number is the ratio of the local flow velocity to the local velocity of sound;

$M=v/c$ and speed of sound can be written as $c = \sqrt{\frac{\gamma P}{\rho}} = \sqrt{\frac{\gamma kT}{m}}$ Eq.(17)

Here P is the local pressure and ρ is the local density. γ is the ratio of heat capacities. Its value is γ=5/3 for a monatomic gas and γ=7/5 for a diatomic gas. For an ideal gas P = nkT, T is the temperature and m is the atomic mass.

$$v_{jet} = u.M = c_0 \frac{M}{[1+\frac{\gamma-1}{2}M^2]^{1/2}} = \frac{M}{[1+\frac{\gamma-1}{2}M^2]^{1/2}} \sqrt{\frac{\gamma kT_0}{m}} \quad \text{Eq. (18)}$$

The directional velocity of the atom is related to the sound velocity of the source (c_0), with T_0 being the temperature of the source.

The Mach number in the hole is M=1 and therefore;

$$v_{jet} = u = \sqrt{\frac{2}{\gamma+1}} \sqrt{\frac{\gamma kT_0}{m}} \quad \text{Eq.(19)}$$

is obtained.

Also, M>>1 can be accepted to find the downstream jet velocity, and in this case;

$$v_{jet} \approx \sqrt{\frac{2}{\gamma-1}}\sqrt{\frac{\gamma k T_0}{m}} \quad \text{Eq. (20)}$$

For a monatomic gas, γ=5/3 and therefore;

$$v_{jet} \approx \sqrt{\frac{5kT_0}{m}} \quad \text{Eq. (21)}$$

The atomic density (n_s) and atomic velocity (v_s) at the mouth of the skimmer can be calculated. In this case;

$$n_s = n_o[1 + \frac{\gamma-1}{2}M_s^2]^{\frac{-1}{\gamma-1}} \quad \text{Eq.(22)}$$

$$v_s = u.M_s = c_0 \frac{M}{[1+\frac{\gamma-1}{2}M_s^2]^{\frac{-1}{\gamma-1}}} \quad \text{Eq.(23)}$$

Here n_0 and c_0 are the atomic density of the source (Nozzle circle) and the speed of sound. M_s is the Mach number at the mouth of the strainer and u is the velocity of the atoms coming out of the hole. As the current beam passing through the filter, As the area of the mouth of the filter; $j = n_s.v_s.A_s$

and the Mach number is defined as; $M_s \approx b.\sqrt{\frac{l_s}{d}}$;here b is a constant that can be determined experimentally (b=2.75).

Maximum intensity to be achieved in the beam source:

1- The rate of diffusion (flux) across the slit—this slit must be narrow enough to reach the free molecular flux—(Grey and Kantrowitz, 1951).
2- It is limited by the inconvenience of geometry factors encountered in obtaining aligned beams from random initial velocities.

The nozzle converts the initial and random transition energy of the gas into directed mass motion. Mass motion has a directive effect that improves both flow rate and geometric factors. Flow rate through the slot; is proportional to the slit area and the number of molecules per unit volume behind the slit.

Experimentally, it has been observed that if the mean free path of the gas is less than the slit width, the flow changes from the molecular flow process to a so-called cloud pattern (Kontrowitz, Grey, 1951). This reduces the beam intensity and the maximum intensity is achieved for the slit width equal to the mean free path of the gas. Initial slit and

collimation provide directed mass movement at the nozzle weld. This increases the density and can be defined as the scattering of molecules passing through a point in the first slit into a hemisphere (Harvey et al. 1950). The radius of this hemisphere can be expressed as the distance between two slits in a molecular source.

In the nozzle type sources; if the mass velocity is made greater than the molecular velocity (Mach number greater than 1 can be considered), the molecules will diffuse in the hemisphere. The radius of this hemisphere is smaller than the distance between the two slits. This factor is roughly equal to the molecular velocity to mass ratio. This causes an increase in density.

In conventional molecular beam welding, they propagate along the molecular slit following the Maxwell velocity distribution and there is no mass movement.

$$Hız\ dağılımı = \frac{u.\exp\left(-\frac{mu^2}{2kT}\right).du}{\int_0^{\infty} u.exp.(-mu^2 72kT).du} \quad \text{Eq.(24)}$$

If particle velocities in the slit plane are v and w, molecules flowing with velocity u will reach a small region on the slit plane.

The fact that the molecular velocity in the beam is partially "monochromatic" is an expected advantage of nozzle type sources. By the monochromatic beam, mechanical rate selectors can be used without reducing the beam density to unfavorable values. In this way, the molecular beam; useful for achieving the same transfer rates and high density.

In conventional molecular beam welding, the distribution of transfer rates is defined as;

$$u^3 \exp(-\frac{mu^2}{2kT}) \quad \text{Eq.(25)}$$

In a nozzle type beam, if the effect of velocity u on the probability of the molecule to pass through the slit is neglected compared to the dominant effect of mass flow velocity,

$$\exp[-m(u-U^2)/2kT_1 \quad \text{Eq.(26)}$$

The temperature before the slit T_1 is represented using the Mach number as:

$$\frac{T_1}{T_0}\frac{1}{1+(RM^2/2C_v} \quad \text{Eq.(27)}$$

(T_0= temperature of the nozzle source, R: Gas constant)

It is seen that the molecules coming from the nozzle mostly have the same velocity and have a higher average velocity for the same gas source temperatures (Grey et al., 1951).

In boundary states, at high Mach numbers, all thermal energy will be converted to energy in the direction of mass motion. The internal molecular energy in the beam will decrease due to isentropic diffusion occurring in the hole in the gas supply. At high Mach numbers the temperature is very low for emanations. For the case of decrease in internal molecular energy behind the rapid temperature drop in the hole; the total number of collisions in the hole is calculated.

Number of collisions: $\int \frac{\bar{c}}{\lambda} dt = \frac{2}{\lambda_0} (\frac{2}{\pi\gamma})^{1/2} \int \frac{dx}{M[1+(\frac{RM^2}{2C_v})]^{\frac{C_v}{R}}}$ Eq.(28)

c : Average molecular velocity, U, M and λ: Average length of free path along the central flux (x), N_0: Number of molecules in the hole.

For the nozzle design, the distance from throat to first slot is 0.0857 times L_1. For this, $L_1 = 3600\lambda_0$ and the number of collisions is approximately 415. Therefore, the rotational energy will be tuned by diffusion and the vibrational energy can be tuned depending on the size of the hole and the resting times of the molecules.

In conventional molecular beams, the width of the first slit is limited by the mean free path. If this experimental rule is adopted for nozzle welding, the flux through the first slot is greater than that of a conventional molecular weld through the first slot.

Molecular velocities are driven in the slit. If the effects of random velocities on the flux rate are neglected, the number of molecules passing through the first slit per second is:

$$S_1 N_1 U_1 = S_1 N_1 M a_1 = S_1 N_1 a_0 \frac{M}{[1+\left|\frac{RM^2}{2C_v}\right|]^{1/2}} \quad \text{Eq.(29)}$$

The geometry of the slit is a fundamental design problem. Molecules entering the slit in the vacuum part and hitting the slit walls can be pumped quickly enough depending on the distribution. If the dispersion angle θ_i is large enough, some of the molecules will have enough transverse velocity components to hit the wall.

$$\theta_i > sin^{-1} \frac{\bar{c}}{u} = sin^{-1} \frac{2(\frac{2}{\pi\gamma})^{1/2}}{M} \quad \text{here} \quad \gamma = 1.4 \quad \text{Eq.(30)}$$

A large enough θ_i is necessary for high pumping speed. The current diverting at the bore should not be large enough to affect the supersonic current upstream from a normal shock. Nozzle-type sources current increases as the Mach number increases. On the other hand, the volume controlled by the nozzle flow pump also increases with the Mach number.

The pumping problem can be reduced by placing the following for the first slit:

1- Mach numbers should be as low as possible.
2- The nozzle should be as small as possible and the boundary layers along these nozzle walls should be consistent with the state of formation while not obstructing the flow in the first slot.

The size of the boundary layers will have a significant effect on the wave pattern in the hole and will also cause uncertainty in the Mach numbers. The dispersion angle is increased for the thickening of the boundary layers (Turner et al. 2004).

Adjustment of the Mach numbers can be made by moving the bore throat axially away from or closer to the slot. During the approximation, while the Mach number decreases; increases during removal.

Mass flow through the hole is traditionally calculated when the flow velocity at the throat of the hole is equal to the local velocity of sound. This current is $0.578\rho_0 a_0 S_{th}$ for $\gamma=1.4$ and

$$\rho_{th} a_{th} S_{th} = \rho_0 a_0 S_{th} \left[\frac{1}{1+\left(\frac{R}{2C_v}\right)}\right]^{C_v/R+1/2} \quad \text{Eq.(31)}$$

where S_{th}: is the area of the throat.

COLTRIMS is a technique that investigates the dynamics of atom-molecule and electron-photon interaction reactions. Simply, the system consists of a cold gas jet target obtained by supersonic propagation in a vacuum, and a part that separates the momentum of ions or electrons from the gas target as a result of ionization.

Target control is extremely important in the COLTRIMS system. Whenever possible, the initial momentum should be known before collision (Ozer 2007). For this purpose, the jet system has been developed. The gas jet consists of a nozzle attached to the end of a cold nozzle. The gas passes through a copper tube and is cooled before being allowed to diffuse into the nozzle. The gas flow is formed in the zone of

silence. In this region, all gas molecules move at the same speed without interacting, and the temperature of the gas in this region is reduced to only a few kelvins. The value of this temperature depends on the gas application pressure and the pressure in the diffusion chamber. The strainer placed in a suitable position removes the gas from the quiescent zone. For gas to exit this zone, the strainer creates a unidirectional high velocity gas jet.

The jet is explained by the movable tube placed on the spectrometer and having an ion measuring instrument at the tip. This tube has the ability to move in and out of the jet. If a different pumping chamber is used as a jet unloader, the pumping power in the main chamber will be reduced and the gas charge of the jet will accumulate entirely in the main chamber.

As ways to reduce the target gas density; the diameter of the hole, the pressure exerted and the seeding can be listed. In this way, gas flow and jet density could be reduced up to a certain factor value at constant pressure. The pressure exerted affects the length of the silence zone and the velocity ratio. It will be a good solution in cases where the probability of ionization is less than that of the target gas (Zeidler et al. 2005). As a gas, the best solution was found in Helium. Because helium has a very high ionization potential and also a very low boiling point. Precooling also increases the density of the jet. Its effects are increased gas flow through the nozzle, low jet velocity and low temperature (Staudte 2005).

Molecular beam researchers placed a wall in front of the propagation with a small skimmer to widen the center beam (Miller et al. 1988, Eder et al. 2013). This situation can be simplified by considering an ideal skimmer placed in the isentropic (adiabatic) region, called the zone of silence (Figure 5). For continuous flow, sufficient pressure value is set so that it will not be effective at the boundaries of the jet. The gas flow starts with a negligible velocity (P_0, T_0) and accelerates towards the weld exit due to the decrease in pressure (P_0- P_b) as the area decreases. The flow can reach the speed of sound. This means that the average speed is equal to the local speed of sound, or Mach number 1.

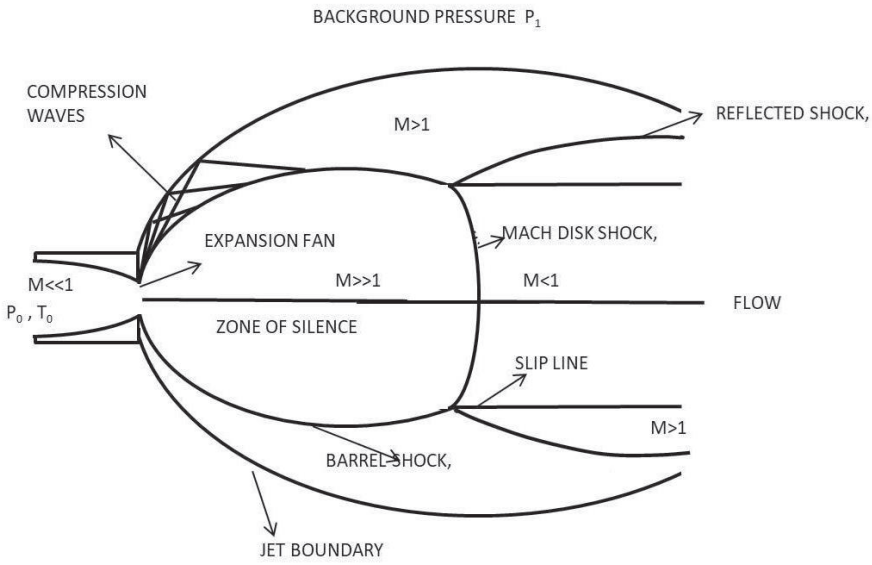

Figure 5. Jet spread under continuous conditions (Scheoffler 2002).

All the properties of the jet depend on the definition of flow in fluid mechanics. These can be expressed as the collision frequency, equilibrium temperature and the length of the assembly, which are sufficiently high density and suitable for the definition of density.

REFERENCES

Erengil Z.N., (2007), Master's Thesis, Geometrik Olarak Soğutulmuş Geri Tepen İyon Spektrometresi Simülasyonu Ve Kurulumu, Afyon Kocatepe University.

Freeman, C. M., Moridis, G. J., Michael, G. E., Blasingame, T. A. (2012, April). Measurement, modeling, and diagnostics of flowing gas composition changes in shale gas wells. In SPE Latin America and Caribbean petroleum engineering conference. OnePetro.

Abdallah A. M.,(1997), Single Ionization In Highly Charged Ion-Atom Collisions At Low Intermediate Impact Velocities, Dissertation of Phd, Kansas State University, Manhattan, Kansas.

Kantrowitz, A., Grey, J. (1951). A high intensity source for the molecular beam. Part I. Theoretical. Review of Scientific Instruments, 22(5), 328-332.

Harvey, R. B., Keidel, F. A., Bauer, S. H. (1950). Some effects of nozzle design on the diffraction of electrons by gases. Journal of Applied Physics, 21(9), 860-874.

Grey, R. E., Krull, H. G., Sargent, A. F. (1951). Altitude Investigation of 16 Flame-Holder and Fuel-System Configurations in Tail-Pipe Burner (No. NACA-RM-E51E03).

Turner, S. E., Lam, L. C., Faghri, M., Gregory, O. J. (2004). Experimental investigation of gas flow in microchannels. J. Heat Transfer, 126(5), 753-763.

Staudte, A. (2005). Subfemtosecond electron dynamics of H2 in strong fields. IKF and Goethe Universität Frankfurt, Diss.

Zeidler, D., Staudte, A., Bardon, A. B., Villeneuve, D. M., Dörner, R., Corkum, P. B. (2005). Controlling attosecond double ionization dynamics via molecular alignment. Physical review letters, 95(20), 203003.

Schöffler, M. S. (2002). Entwicklung und Aufbau eines Abbildungssystems zur Messung von Elektronen jenseits niedriger Energien (Doctoral dissertation, Univ.-Bibliothek Frankfurt am Main).
Eder, S. D., Samelin, B., Bracco, G., Ansperger, K., Holst, B. (2013). A free jet (supersonic), molecular beam source with automatized, 50 nm precision nozzle-skimmer positioning. Review of Scientific Instruments, 84(9), 093303.

Miller, A. C., Whiting, R., Wilcox, D. B. (1989). An evaluation of a skimmer dredge for collecting freshwater mussels. Journal of Freshwater Ecology, 5(2), 151-154.

Chapter 6

CONVERSION OF WASTEWATER SLUDGE INTO COMMERCIALLY VALUABLE PRODUCTS

F. Olcay TOPAÇ[1]

1 Prof.Dr. F. Olcay Topaç, Bursa Uludag University, Department of Environmental Engineering, ORCID: 0000-0002-6364-4087, olcaytopac@uludag.edu.tr

Introduction

Wastewater sludges are semi-solid materials released as a waste stream in wastewater treatment plants and are considered as a waste group that poses a great risk for the environment. It has been emphasized in many studies that wastewater sludge disposal under inappropriate conditions and poor sludge management approaches unfortunately create environmental pollution problems and threaten human health (Rorat et al., 2019).

Waste sludge components and their environmental effects require these wastes to be disposed of after being processed with appropriate methods. Although there are numerous proposed and/or applied methods for waste sludge disposal, approaches that ensure the sustainable use of wastewater sludge attract attention from both an economic and ecological perspective. Considering the applications within the framework of this approach, it is seen that wastewater sludges with certain characteristics are generally applied to agricultural lands as organic fertilizers. With its use in agriculture, plant nutrients in the waste sludge are added to their natural cycle in the soil, the fertilizer need of the growing plants is met and economic gain is achieved in agricultural production (Delibacak and Ongun, 2016; Samara et al., 2017; Otieno et al., 2019; Santacoloma-Londono et al., 2020). However, in recent years, various concerns have arisen concerning the agricultural utilization of waste sludge. Although the application of this biowaste that contains huge amounts of organic matter and nutrients to the soil is evaluated as beneficial, several organic and inorganic pollutants and pathogenic organisms that can be found in the sludge pose a serious risk in terms of soil quality and environmental health.

More recently, sludge-borne 'emergent pollutants', which may include pharmaceuticals, personal care products, hormones and other xenobiotics, have attracted the attention of researchers because of the health risks they pose. It was stated in a study that approximately 65% of the micropollutants in the wastewater are transferred to the sludge phase during activated sludge process (Barret et al., 2012). A similar study confirmed that nearly all active pharmaceuticals found in influent water were also detected in wastewater sludge (Martin et al., 2012). Moreover, sludge digestion processes are unfortunately not effective in most cases in removing the micropollutants accumulated in the sludge. It has been stated in many studies that micropollutants with hydrophobic properties degrade very slowly under anaerobic conditions and accumulate accordingly (Gonzales et al., 2010). Gonzalez-Gil et al. (2016) examined the effect of anaerobic treatment on some organic micropollutants and found that ibuprofen and triclosan were only slightly affected. Similarly, a pilot-scale study was conducted by Phan et al.,(2018) to examine the degradation of trace organic pollutants in the primary sludge during anaerobic digestion.

Their results apparently showed that the anaerobic digestion process is insufficient for the removal of trace organic pollutants with the value of logD>1.5. The study also revealed that the sorption onto the solid phase appears to be a hindering factor for the biodegradation of these organic pollutants. Considering that a significant portion of digested sludge is used for agricultural purposes, it is obvious that micropollutants originating from sludge may cause a great hazard to the soil environment and growing plants. In other words, as a result of waste sludge application to agricultural areas, the unsafe components in the sludge may spread in the soil environment and threaten human health by negatively affecting food safety. All those concerns caused by the application of sludge to agricultural lands led to various studies to reveal alternative reuse options for waste sludge.

Recovery of nutrients as well as other materials from waste sludge is considered as a rational approach that eliminates the potential adverse impacts associated with its direct use in agricultural areas. The main objective of this chapter is to ensure an overview regarding the actual information on the production of commercially valuable products from wastewater sludges.

Nutrient Recovery

Nitrogen and phosphorus are considered to be two important components of sewage sludge that can be recycled technically and economically (Tyagi and Lo, 2013). However, phosphorus in particular is becoming the most important nutrient due to depleted resources. Given the estimations that only 50 to 100 years of phosphorus reserves remain in the world, recovering this valuable resource to meet the claims is of paramount importance for the goals of sustainable development (Cordell et al. 2011).

Anaerobic digestion is a frequently applied practice that enables the production of biogas, a renewable energy source, from wastewater sludge, black water, animal manures and various agricultural wastes. In order to ensure a weight reduction in the mass of digestate, dewatering processes are applied and as a result, the organic slurry is separated into a liquid fraction and solid cake. The liquid fraction of the digestate contains nutrients such as phosphorus and nitrogen in abundance and is considered a suitable waste fraction for the application of nutrient recovery technologies. Currently, most of the phosphorus recovery processes use precipitation/crystallization procedures to seperate phosphate compounds where struvite precipitation was one of the most well-known technologies.

Struvite precipitation technology is a frequently used technology for the recovery of phosphorus in waste streams. Struvite is a white orthorhombic crystal compound constitutes phosphate (PO_4), ammonium (NH_4) and magnesium (Mg) with the chemical formula of $MgNH_4PO_4.6H_2O$ (Cornel

and Schaum, 2009). Many factors influence the efficiency of the struvite precipitation process, such as molar ratio of NH_4, PO_4 and Mg in the liquid stream, and pH. The pH should be in the range of 7.6–10.5 to support the formation of struvite. In addition, the Mg:P:N molar ratio in the liquid stream must be adjusted to a stoichiometric value of 1:1:1 for successful nucleation of struvite crystals (Siciliano et al., 2020). Gonzales-Morales et al. (2021) conducted experiments using batch reactors to precipitate phosphorus as struvite in the supernatant produced during dewatering of digested sludge. The results of the study carried out under controlled pH and temperature conditions showed that the optimum temperature and pH for the formation of high-purity (>70%) struvite crystals were 25 °C and 9, respectively.

On the other hand, various studies have been conducted in which bio-based processes have been developed to recover phosphorus in nutrient-rich wastewater and related streams. The potentials of *Brevibacterium antiquum* to form biostruvite in dewatering effluent of waste sludge were investigated in a study done by Simoes et al. (2020). The results of their study showed that *B. antiquum* used condensed and organic phosphorus fractions found in the waste stream and successfully formed biostruvite. In addition, it was emphasized in the study that the tested biostruvite formation method offers a higher potential compared to conventional struvite precipitation methods.

In addition, thermochemical methods and/or acid leaching methods can be used to recover phosphorus in waste streams and to produce phosphorus fertilizers or various phosphorus-containing industrial raw materials (Donatello, and Cheeseman, 2013). Lee et al. (2018) used different acids and alkalis to dissolve phosphorus in the dewatered sludge cake and achieved a maximum phosphorus solubility in the range of 55-71% using H_2SO_4. In a similar study by Semerci et al. (2021), acidic and alkaline leaching methods were evaluated for the recovery of phosphorus from sludge and sludge incineration ash, and it was concluded that strongly acidic conditions (HCl) were superior for P leaching.

Biochar Production

Pyrolysis is a thermal process and allows organic matter to decompose in an oxygen deficient atmosphere. It is recognized as a second generation, relatively simple and cheap alternative bioenergy production technology and is used to convert biomass into valuable products like syngas, bio-oil and solid remnants (Racek et al., 2020; Thangarajan et al.,2016). Although obtaining liquid and gaseous fuels from sludge is seen as the apparent advantage of pyrolysis, solid residues (biochar) released as a result of the process may also have many useful practices. Biochar is a

technical statement used for “the porous carbonaceous solid produced by the thermochemical conversion of organic materials in an oxygen depleted atmosphere that has physicochemical properties suitable for safe and long-term storage of carbon in the environment” (Shackley et al., 2012). Biochar is a perfect soil conditioner and has recently attracted attention as a multifunctional material that has been successfully used in areas such as pollutant immobilization, carbon sequestration, greenhouse gas reduction, soil and water retention (Callegari and Capodaglio, 2018). Sousa and Figueiredo (2016) applied different doses of sludge-based biochar into the soil and investigated its effects on soil fertility. In addition, the effect of the application on the agronomic growth of the radish *Raphanus sativus* L. (*Brassicae*) was evaluated by the pot experiments. The results showed that biochar can supply sufficient nutrients to the plants and increased the productivity of radish in a short time. In another study, the long-term impacts of sludge-based biochars on soil characteristics were examined and the residual effect of biochar application on corn yield was evaluated (Fachini et al., 2021). The results indicated that biochars produced from sludge remarkably increased the nutrient content of the soil and enhanced the uptake of nutrients, especially phosphorus, by maize. It was also observed that the phosphorus content in soils with biochar was five times higher than those in control and NPK-treated soils.

Aside from its benefit in agricultural production, many studies have emphasized that biochar has a perfect ability to remove various contaminants like heavy metals, organic compounds and other pollutants from waste streams. In a study conducted by Dos Reis et al. (2016), biochar was obtained by treating the sewage sludge with HCl after pyrolysis at 500 °C. The results demonstrated that the sorption capacity of the obtained biochar for hydroquinone, an aromatic organic compound, was very high (1218.3 $mg.g^{-1}$). In a similar research, Fan et al. (2021) studied the adsorption behavior of metal-loaded sludge-based biochars for three antibiotics (tetracycline, sulfamethoxazole and amoxicillin) found in wastewater. The results showed that the effective mechanisms for the adsorbtion of antibiotics to biochars derived from sludge are predominantly Van der Waals forces, H-bonding and pore filling. Yang et al. (2019) used sludge-based biochar and α-Fe2O3 and FeOOH to prepare chemically modified biochars for evaluating the effectiveness of Ni adsorption from liquid solutions. At the end of the trials, the adsorption capacity of the modified biochar for Ni(II) was found as 35.50 $mg.g^{-1}$. In addition, it was stated that the effective mechanisms in the adsorption of heavy metals by biochar are ion exchange among the functional groups in biochar and metal ions, and surface interaction through complexation (Lu et al., 2012). Considering all these studies emphasizing the beneficial use of sludge-based biochar,

it is possible that this material will be used more widely in the future, thus supporting the sustainable use of sludge as a valuable resource.

Extracellular Polymeric Substances

Today, biopolymers generated from renewable resources are becoming appealing due to the increasing environmental concerns caused by the widespread use of plastics and are recently the focal point of extensive study on the subject (Kreyenschulte et al., 2014). In particular, extracellular polymeric substances (EPS) are of greater commercial profits compared to intracellular polymers such as glycogen and polyphosphate (Feng et al., 2020). EPS are complex organic macromolecules which are secreted by biofilm forming bacteria during cell metabolism and they are characyterized as a slimy, glue-like substance enhancing the formation of a matrix that plays an important role in cell adhesion phenomena. Although the predominant components of EPS are polysaccharides and proteins, other macromolecules such as lipids, nucleic acids and humic substances may also be found in the biopolymeric matrix. In addition, it was emphasized in recent studies that complex glycoconjugates such as glycosaminoglycans were detected in EPS (Felz et al., 2020).

Today, EPS recovered from sludge is seen as a potential resource and will gain more importance in the future with the conversion of wastewater treatment plants to more functional biorefineries. EPS accounts for a large part of the dry weight of sludge and can be used in various fields as biomaterials, medical reagents, industrial sizing agents and rheological modification additives (Feng et al., 2021).

In a recent study, EPS were extracted from aerobic granular and activated sludge and the effectiveness of these biopolymers as flame retardant materials was evaluated. For this purpose, a burning test was applied to evaluate the flammability of the flax fabric coated with EPS. The results showed that EPS extracted from sludge can be used successfully to generate flame retardant material and this application has great potential to support circular economy (Kim et al., 2020). Lin et al. (2015) extracted a biomaterial from aerobic granular sludge and investigated the potential of using this polysaccharide-containing material as a surface coating chemical. For this purpose, the composition, morphological features, molecular weight, amphiphilic and film-forming properties of the biomaterial were examined. The results indicated that the investigated polysaccharide-based biomaterial showed amphiphilic properties due to its carbohydrate and lipid content, and it could readily form a film on a hydrophilic surface such as paper and increase the water resistance of the surface.

Moreover, EPS obtained from sludge has the potential to be used as a cost-effective and efficient biosorbent in various water/wastewater

treatment industries. Numerous reports show that sludge-derived EPS can be used successfully for the elimination of heavy metal ions from water. Guibaud et al. (2012) extracted EPS from anaerobic granular sludge obtained from 3 different sources with the help of cationic exchange resin and investigated the effects of pH on Cd and Pb binding capacity of the obtained biomaterials. The obtained outcomes indicated that, in general, Pb had a higher affinity for EPS compared to Cd. In addition, it was emphasized that both organic and inorganic fractions in the particulate form of EPS played a role in heavy metal adsorption.

Protein Recovery

The organic matter of waste activated sludge consists of various complex components in the form of proteins, polysaccharides and lipids, and the ratio of proteins in these substances is estimated to be around 40% (Tanaka et al., 1997). Considering this high ratio, protein recovery from waste activated sludge can be considered as a potential application for the conversion of a waste material into a useful and commercially valuable product. It seems possible that the recovered proteins can be used in the production of many commercial products such as wood glue, fire extinguisher, animal feed and corrosion inhibitor. In a study by Hwang et al. (2008), the potential of using waste sludge-based protein as animal feed was assessed. The study results indicated that the nutrient content of the recovered biomaterial was similar to commercial animal feed. In addition, rat toxicity test was applied to determine the possible toxic effects of the obtained material and it was concluded that the recovered protein did not have any detrimental effects on mortality, body weight changes, the incidence of clinical signs, and necropsy findings.

In another study by Pervaiz and Sain (2011), kraft paper mill waste sludge was used as a source of biomass and the protein in the sludge was extracted after alkaline disintegration and precipitation steps. Then, the use of the extracted protein as a wood adhesive was assessed. The adhesion performance of the recovered biomaterial containing 30% crude protein was evaluated by comparing it with phenol formaldehyde resin and soy protein isolate. The results regarding the shear strength of bonded wood composites clearly showed that it is technically possible to use recovered sludge proteins as an eco-friendly wood adhesive. Go et al., (2019) evaluated the potential of using extracellular polymeric materials from waste sludge as corrosion inhibitors and concluded that sludge-based biomaterials have similar performance with commercial products on the market. It has also been stated that the corrosion inhibitor obtained from sludge can be defined as a green product with its features such as being renewable, biodegradable, non-toxic and free of heavy metals.

Protein recovery from waste sludge includes various steps such as pretreatment, filtration, precipitation, separation, etc. (Figure 1). The most important step in recovering proteins from sludge is probably to apply physical, thermal, chemical, biological processes or their combinations to destroy the sludge flocs and bacterial cells. Song et al. (2019) applied thermal alkali hydrolysis pretreatment at 80°C for 90 minutes to dissolve the proteins in the sludge and reached a solubility value of 67.59%. In the study, it was also stated that 9.44% of soluble proteins were lost due to conversion to ammonium and nitrate nitrogen. Xiao and Zhou (2020) evaluated the alkaline pretreatment at pH 12, ultrasound application (1 W.mL-1) and thermal (80 oC) hydrolysis as sludge protein solubilization methods. According to the results, it was concluded that the alkaline pretreatment method is more effective in the release of both high molecular weight (> 20 kDa) and low molecular weight (<20 kDa) proteins. In another study Garcia et al. (2017) investigated the efficiency of wet oxidation and thermal hydrolysis processes in the recovery of sludge protein. The results showed that sludge hydrolyzed by hydrothermal methods has the potential to be a renewable resource for protein recovery. The maximum protein concentrations obtained by wet oxidation and thermal hydrolysis methods were 7.7 g/l and 7.2 g/l, respectively. It was also determined that the most effective method to separate the proteins from the hydrothermally treated sludge was the addition of ammonium sulfate. Gao et al. (2019) applied a combined thermal pretreatment and enzymatic hydrolysis procedure to extract protein from excess sludge, and an extraction rate of 52.8% was achieved. The optimum conditions determined for the applied method are as follows: 3 hours thermal treatment at 100 °C, enzymolysis pH of 11, protease dose of 3000 U/g dry sludge, 3 hours enzymatic hydrolysis at 55 °C.

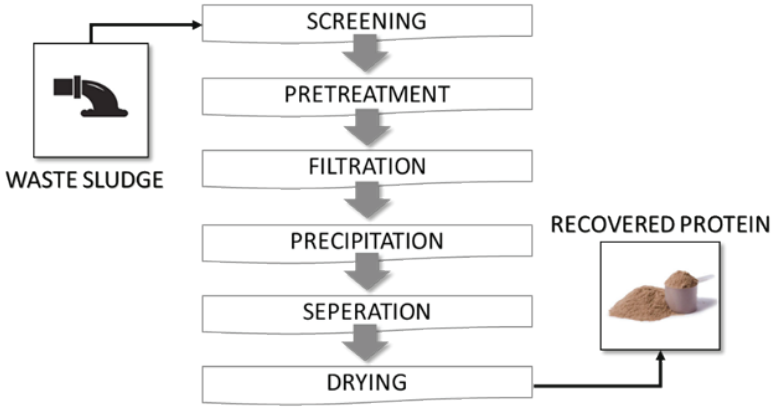

Figure 1. Basic processes applied in protein recovery from waste sludge

Industrial Enzyme Extraction

Enzymes are basically proteins produced by living organisms and responsible for catalyzing chemical reactions inside the cell. These biocatalysts accelerate biochemical reactions by reducing activation energy barriers and increasing the proper orientation collision of molecules. Offering many advantages over inorganic catalysts, enzymes work under milder reaction conditions, have better product selectivity, and lower environmental and physiological toxicities (Berg et al., 2002; Choi et al., 2015). Enzymes can be used in many industrial areas (Figure 2). While the food and beverage, pharmaceutical, biofuel and detergent industries benefit from the catalyst properties of enzymes on a commercial scale, the use of enzymes in industries such as fine chemical manufacturing and natural gas conversion has come to the fore in recent years (Chapman et al., 2018). Economic evaluations for various industries show that enzymes constitute 30-40% of the production cost required for the preparation of the culture medium (Raheem et al., 2018; Vaithyanathan and Cabana, 2021).

Recent studies show that waste biological sludge can be evaluated as a potential biomass for industrial enzyme extraction. Most of the hydrolytic enzymes in sludge flocs are either found in EPS matrix or bound to the cell wall. Therefore, the first step in enzyme extraction from waste sludge is to disrupt the sludge flocs and harvest the bacterial polymers. For this purpose, many extraction methods such as physical disruption, chemical addition or combined methods are applied to the sludge. Liu and Smith (2019) defined a procedure containing ultrasound treatment and surfactan addition for releasing protease and cellulase from waste sludge. The maximum protease and cellulase recovery from the sludge was found as 63% and 100%respectively, with a frequency of 20 kHz, a power density of 872 W/L, sonication time of 10 min and surfactant addition of 1% v/v TX100. Nabarlatz et al. (2012) applied a method including ultrasonication, extraction, dialysis and lyophilization steps for enzyme recovery from waste sludge and obtained 23 units of lipase per gram lyophilized sludge.

The studies related to enzyme recovery have been demonstrated that enzyme extraction following sludge floc disruption is technically feasible in bench-scale experiments. However, for specific industrial applications, purification and concentration procedures need to be standardized and optimized for a higher degree of purity.

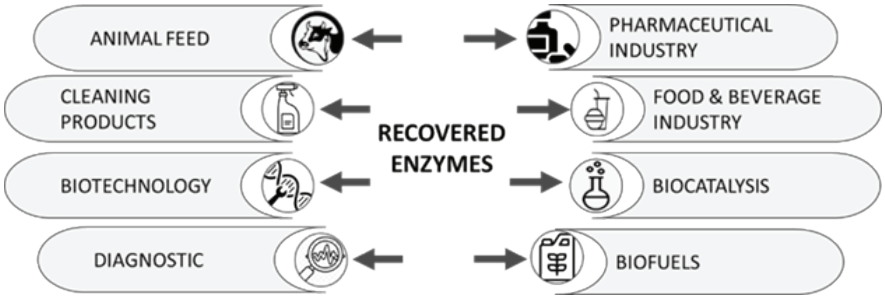

Figure 2. Industrial applications of enzymes

Biopesticide Production

Biopesticides are biologically-derived agents and are considered the best alternative to synthetic pesticides due to their advantageous properties. Those eco-friendly substances are highly effective and specific against their target. Thus the use of biopesticides in pest control programs significantly increased worldwide. Recently, many biopesticides are produced from microorganisms (bacteria, fungi, virus or protozoan) and plants, and derived from animals (pheromones, hormones, insectspecific toxins, etc.), and used across the world in the control of agricultural pests (Nawaz et al, 2016).

Bacillus thuringiensis, bacteriophages and *Trichoderma spp*. are the main species utilized as biocontrol agents. Almost 90% of the experimental studies on biopesticide production in the literature includes the use of *B. thuringiensis* (Bt) strain, which is known to produce d-endotoxin during sporulation (Melo et al., 2016). *Bacillus thuringiensis*-based biopesticides, which are considered the most popular biopesticides, are used in forest cultivation, agricultural production and public health services all over the world. However, the greatest barrier to commercial production of *Bacillus thuringiensis*-based biopesticides is the huge cost of raw material requirement for inoculation (Raheem et al., 2018). In order to overcome this challenge, waste biological sludge can be used as a culture medium, enabling the manufacture of value-added biopesticides.

Waste activated sludge offers a low-cost culture medium alternative for the production of *Bacillus thuringiensis* and the reuse of waste sludge in agricultural areas and forests for pest control seems to be acceptable in terms of the waste management hierarchy (Tyagi et al., 2009). According to Mohammedi et al. (2006) isolated 12 strains of Bacillus thuringiensis (Bt), ten from sludge and two from dead Tortricidae larvae, and evaluated their insecticidal activity. The results obtained by the PCR method showed that all 12 bacterial strains contained the Cry IA gene and five had the

Cry IC gene, both of which encode the active toxin against *Lepidoptera* species. Furthermore, bioassays using *Choristoneura fumiferana* larvae clearly demonstrated the apparent insecticidal activity of these strains against *Lepidoptera* species. As a result of the study, it was noted that Bt strains isolated from waste sludge could be used to provide a more effective approach for the manufacture of biopesticides.

Volatile Fatty Acid Recovery

Biological nutrient removal is one of the most common and cost-effective method for removing total nitrogen and total phosphorus from waste streams through the microbial activities, and the process is becoming an increasing challenge for wastewater treatment plants due to increasing discharge standards. However the lack of a sufficient carbon source in influent is the major drawback of the process (Wu et al., 2010). Volatile fatty acids (VFAs) such as acetic acids and propionic acids have been found to be the most appropriate carbon source for nutrient removal (Chen et al., 2004; Shen and Zhou, 2016). VFAs are valuable chemicals produced during anaerobic digestion process of waste materials. Until now, the main goal of anaerobic digestion processes is converting the organic fraction of waste sludge into noncellular end products such as biogas (Athanasoulia et al., 2012; Demirbaş et al., 2016; Grosser and Neczaj, 2016). Studies on the recovery of volatile fatty acids from waste sludge and the use of the obtained green product as an external organic carbon source for nutrient removal apparently show that waste sludge can be used as a sustainable resource in wastewater treatment facilities (Liu et al., 2016; Tong and Chen, 2007; Xiong et al., 2012).

VFAs production is of great interest, especially because it offers a greater value than biogas and has a wider range of industrial uses (Atasoy et al., 2018). Numerous laboratory-scale studies in the literature indicated that the generation of VFAs from fermentation of waste sludge is a rational way, and alkaline conditions remarkably improve this process. Liu et al. (2012) investigated the VFAs generation by acidogenic fermentation of waste sludge, their synthesis pathways and the bacterial community involved in this process under different pH conditions. The results showed that pH affects the overall VFAs production yield and the individual VFA percentage. The total VFAs yield at pH 9.0 was recorded as 10.70 times the yield at pH 3.0. Similarly, Gracia et al. (2020) conducted anaerobic digestion trials to assess the VFAs production potential of waste activated sludge. It was concluded that VFAs can be produced at a concentration of 372 to 1600 mg COD/L under alkaline conditions. It was also emphasized in the study that VFAs extracted from waste sludge could be used as an external carbon source for biopolymer synthesis in the future. In another study, alkali fermentation process was applied to sludge and pilot-scale

generation of VFAs was evaluated. In the study, the effects of using the obtained fermentation liquor as a C source on the nutrient removal process were also investigated. By adding VFAs-rich fermentation liquor to the nutrient process, nutrient removal kinetics were improved and higher removal efficiencies were achieved in comparison to the use of acetic acid (Longo et al., 2015). As a result of a study in which the acidogenic and methanogenic activities of agro-industrial wastes obtained from different sources were determined, it was found that the economic gain of VFA production from residues were three times higher than methane production (Perimenis et al., 2018). A more extensive evaluation of the process economy was carried out by comparing VFA production and biogas production from waste sludge in a full-scale plant. As a result of the calculations, the net profit of VFA and biogas was reported as 9.12 USD/m3 and 3.71 USD/m3, respectively (Liu et al., 2018).

All these studies reveal the potential of using sludge-derived VFA as an alternative carbon source in biological nutrient removal processes. Although methane as the end product of anaerobic digestion is the main focus in the literature, production of VFAs from waste sludge expected to receive higher industrial attention in the future.

Polyhydroxyalkanoic Acids (PHAs) Production

Polyhydroxyalkanoic acids (PHAs) are intracellular granules commonly found in prokaryotes and have properties that enable them to be used as biobased plastics. Environmental concerns caused by plastic pollution have accelerated the studies on the use of PHAs as a raw material for bioplastic generation. PHAs, which are the most biodegredable polymers, minimize the impact on the environment and create a closed cradle-to-cradle cycle. In addition, being produced from a renewable source is another advantage of PHAs production. However, the high expenses of the synthetic substrate and the fermentation process used in the production of PHAs are the major barriers to large-scale commercial production (Reddy et al., 2003). The market price of PHA polymers and petroleum-based polymers is 0.8–1.5 €/kg and 5 €/kg, respectively, with a 6-fold difference (van den Oever et al., 2017). Therefore, there is a great need to develop organisms that produce optimum PHA by cheaper methods.

The use of mixed microbial cultures in PHA production processes offers many advantages compared to pure cultures. Mixed cultures can consume different carbon sources such as agricultural or industrial wastes. In addition, the operating and maintenance costs of mixed culture production are lower since sterilization is not performed and there are few control parameters. Because of these advantages, the use of mixed microbial consortia for PHAs generation has gained priority. Recently, many studies

have been made on the use of waste biological sludge for PHAs generation (Raheem et al., 2018; Munir and Jamel, 2020). In addition, some bacterial species found in activated sludge show PHAs accumulating performance for use as a source of energy and carbon under certan conditions (Yang et al., 2013). The average PHAs content in waste activated sludge has been found as 0.3 to 22.7 mg PHA/g WAS (Tian et al., 2009; Crutchik et al., 2020). The combined use of mixed microbial cultures and several waste materials as carbon sources provides energy saving and material cost reduction solutions in PHA production processes.

The steps followed in the production of PHA from waste sludge are shown in Figure 3. In the PHA production process from waste sludge, acidogenic bacteria form volatile fatty acids such as acetic and propionic acids. Regimes of feast and famine are applied to the microbial community to increase the strains that accumulate PHA in the sludge. Thus, the resulting VFAs can be converted into PHA by microorganisms in the presence of a growth limiting component or excess carbon as an energy source (Salehizadeh and Van Loosdrecht, 2004).

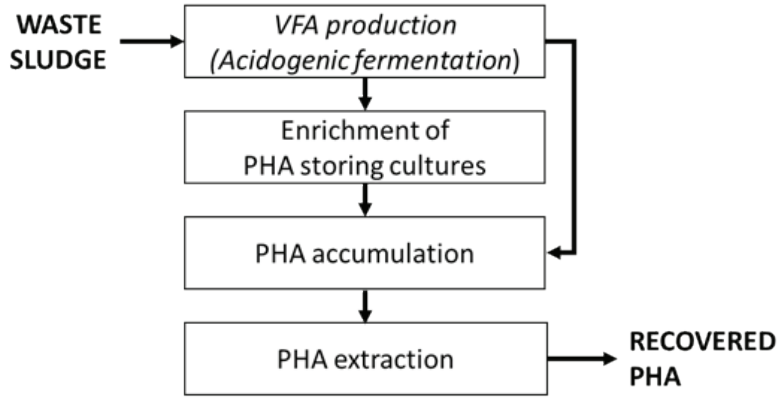

Figure 3. The steps followed in the production of PHA from waste sludge

In the study by Mengmeng et al., (2009), the usability of sludge-derived VFAs as a C source was evaluated to synthesize PHA. The results indicated that the VFAs generation yield was 258.65 mgTOC/gVSS under high temperature (60 °C) and alkaline conditions (PH=11). In addition, acetic acid was found to be the most predominant type among VFAs obtained from sludge. The maximum PHA content obtained by using sludge-derived volatile fatty acids as C source was 56.5% of the dry cell. The overall evaluation of the study indicated that VFAs extracted from waste activated sludge were a suitable C source for PHAs generation. In a study by Crutchik et al. (2020), the economic feasibility of PHA production

in two different wastewater treatment plants was investigated. One of the examined wastewater treatment plants is a large facility with an anaerobic sludge digestion unit, and the other is a small plant where sludge is only dewatered. The feasibility calculations showed that the minimum cost of PHA in large and small wastewater treatment plants is US$1.26/kg PHA-crude, respectively, when using a PHA production process consisting of enrichment and accumulation steps.

Conclusion

The management of wastewater sludge, which is released in large quantities from wastewater treatment plants, is a serious concern for wastewater industry and local governments due to both socio-economic and environmental considerations. The use of traditional sludge disposal methods, such as landfill, incineration, land application or ocean disposal, is limited by stringent regulations and pressure from the environmental authorities as well as the general public. Ensuring effective and sustainable management of waste sludge is precisely one of the problematic challenges for wastewater treatment professionals.

Considering the legal obligations and circular economy concepts, the use of wastewater sludge for resource and energy recovery is considered to be the most logical approach. With the view that sludge is accepted as a resource rather than a waste, practices and studies aimed at the recovery of various precious components such as nutrients, protein, carbon, EPS and enzymes from sludge have gained priority. The recovery studies of biomaterials from waste sludge and future planning to boost the circular economy should not be evaluated only in terms of the current economic value of the recovered products in the market. Because, in most cases, the disposal of sludge by conventional methods is more profitable than the recovery of materials. However, the economic damage caused by pollution associated with various sludge disposal routes and rising prices due to pressure on non-renewable resources will completely change this perspective in the future. The use of sludge-based biomaterials not only reduces greenhouse gas emissions, but also eliminates environmental pollution caused by the disposal of mismanaged waste. Biomaterial recovery from waste sludge provides a series of services such as protection of water quality, increase of performance in waste treatment plants, improvement of food safety and social equality, which can not be easily converted into cash but are very important for society and the environment. Value-added bio-products to be obtained by processing waste sludge as a valuable resource will play a leading role in the circular economy in the future as sustainable green product alternatives.

Referanslar

Atasoy, M., Owusu-Agyeman, I., Plaza, E. & Cetecioglu Z. (2018). Bio-based volatile fatty acid production and recovery from waste streams: Current status and future challenges. *Bioresource Technology, 268*, 773-786. doi:10.1016/j.biortech.2018.07.042.

Athanasoulia, E., Melidis, P. & Aivasidis, A. (2012). Optimization of biogas production from waste activated sludge through serial digestion. *Renewable Energy, 47*, 147-151. doi:10.1016/j.renene.2012.04.038.

Barret, M., Delgadillo-Mirquez, L., Trably, E., Delgénès, N., Braun, F., Cea Barcia, G., Steyer, J. P. & Patureao, D. (2012) Anaerobic removal of trace organic contaminants in sewage sludge: 15 years of experience. *Pedosphere, 22,* 508-517. doi:10.1016/S1002-0160(12)60035-6.

Berg, J.M., Tymoczko, J.L. & Stryer, L. (2002). *Biochemistry*, 5th edn. W. H. Freeman Publishing, New York.

Callegari, A. & Capodaglio, A. G. (2018). Properties and beneficial uses of (bio) chars, with special attention to products from sewage sludge pyrolysis. *Resources, 7,* 20. doi:10.3390/resources7010020.

Chapman, J., Ismail, A. E., & Dinu, C. Z. (2018). Industrial applications of enzymes: Recent advances, techniques, and outlooks. *Catalysts, 8*, 238. doi:10.3390/catal8060238.

Chen, Y., Randall, A. A. & Mc Cue, T. (2004). The efficiency of enhanced biological phosphorus removal from real wastewater affected by different ratios of acetic to propionic acid. *Water Research, 38*, 27–36, doi: 10.1016/j.watres.2003.08.025.

Choi, J. M., Han, S. S. & Kim, H. S. (2015). Industrial applications of enzyme biocatalysis: Current status and future aspects. *Biotechnology Advances, 33*(7), 1443-1454. doi:10.1016/j.biotechadv.2015.02.014.

Cordell, D., Rosemarin, A., Schröder, J. J. & Smit, A. L. (2011). Towards global phosphorus security: A systems framework for phosphorus recovery and reuse options. *Chemosphere, 84*(6), 747–758. doi: 10.1016/j.chemosphere.2011.02.032.

Cornel, P. & Schaum, C. (2009). Phosphorus recovery from wastewater: Needs, technologies and costs. *Water Science and Technology, 59*, 1069– 1076, doi:10.2166/wst.2009.045.

Crutchik, D., Franchi, O., Caminos, L., Jeison, D., Belmonte, M., Pedrouso, A., Val del Rio, A., Mosquera-Corral, A. & Camposi J. L. (2020). Polyhydroxyalkanoates (PHAs) production: A feasible economic option for the treatment of sewage sludge in municipal wastewater treatment plants? *Water, 12*(4), 1118. doi:10.3390/w12041118.

Delibacak, S. & Ongun, A. R. (2016). Influence of treated sewage sludge applications on corn and succeeding wheat yield and on some properties of sandy clay soil. *Turkish Journal of Field Crops, 21*(1), 1-9. doi:10.17557/tjfc.88475.

Demirbaş, A., Taylan, O. & Kaya, D. (2016). Biogas production from municipal sewage sludge (MSS). *Energy Sources, Part A: Recovery, Utilization, and Environmental Effects, 38*, 20, 3027-3033. doi:10.1080/15567036.2015.1124944.

Donatello, S. & Cheeseman, C. R. (2013). Recycling and recovery routes for incinerated sewage sludge ash (ISSA): A review. *Waste Management, 33*, 2328– 2340. doi:10.1016/j.wasman.2013.05.024.

dos Reis, G. S., Adebayo, M. A., Sampaio, C. H., Lima, E. C., Thue, P. S., de Brum, I. A. S., Dias, S. L. P. & Pavan, F. A. (2016). Removal of phenolic compounds from aqueous solutions using sludge-based activated carbons prepared by conventional heating and microwave-assisted pyrolysis. *Water, Air, & Soil Pollution, 228*, 33. doi:10.1007/s11270-016-3202-7.

Fachini, J., Coser, T. R., Araujo, A. S. D., Vale, A. T. d., Jindo, K. & Figueiredo, C. C. d. (2021). One year residual effect of sewage sludge biochar as a soil amendment for maize in a brazilian oxisol. *Sustainability, 13*, 2226. doi:10.3390/su13042226.

Fan, X., Qian, Z., Liu, J., Geng, N., Hou, J. & Li, D. (2021). Investigation on the adsorption of antibiotics from water by metal loaded sewage sludge biochar. *Water Science and Technology, 83*(3), 739–750. doi:10.2166/wst.2020.578.

Felz, S., Neu, T. R., van Loosdrecht, M. C. M. & Lin, Y. (2020). Aerobic granular sludge contains hyaluronic acid-like and sulfated glycosaminoglycans-like polymers. *Water Research, 169*, 115291. doi:10.1016/j.watres.2019.115291.

Feng, C., Lotti, T., Canziani, R., Lin, Y., Tagliabue, C. & Malpei, F. (2021). Extracellular biopolymers recovered as raw biomaterials from waste granular sludge and potential applications: A critical review, *Science of The Total Environment, 753*, 142051. doi:10.1016/j.scitotenv.2020.142051.

Feng, C., Welles, L., Zhang, X., Pronk, M., de Graaff, D. & van Loosdrecht M. (2020). Stress-induced assays for polyphosphate quantification by uncoupling acetic acid uptake and anaerobic phosphorus release. *Water Research, 169*, 115228. doi:10.1016/j.watres.2019.115228.

Gao, J. L., Wang, Y. C., Yan, Y. X. & Yue, Q. C. (2019). Extraction of protein from excess sludge by thermal pretreatment assisted enzymatic hydrolysis. *IOP Conf. Series: Earth and Environmental Science, 344*, 012084. doi:10.1088/1755-1315/344/1/012084.

Garcia, M., Urrea, J. L., Collado, S., Oulego, P. & Díaz, M. (2017). Protein recovery from solubilized sludge by hydrothermal treatments. *Waste Management 67*, 278–287. doi:10.1016/j.wasman.2017.05.051.

Guibaud, G., Bhatia, D., d'Abzac, P., Bourven, I., Bordas, F., van Hullebusch, E., Lens, P. N. L. (2012). Cd(II) and Pb(II) sorption by extracellular polymeric substances (EPS) extracted from anaerobic granular biofilms: Evidence of a pH sorption-edge, *Journal of the Taiwan Institute of Chemical Engineers, 43*(3), 444-449. doi:10.1016/j.jtice.2011.12.007.

Go, L. C., Holmes, W., Depan, D. & Hernandez, R. (2019). Evaluation of extracellular polymeric substances extracted from waste activated sludge as a renewable corrosion inhibitor. *PeerJ, 7*, e7193, doi:10.7717/peerj.7193.

Gonzales, M. M., Martin, J., Santos, J. L., Aparicio, I. & Alonso, E. (2010). Occurrence and risk assessment of nonylphenol and nonylphenol ethoxylates in sewage sludge from different conventional treatment processes. *Science of the Total Environment, 408*(3), 563-570. doi: 10.1016/j.scitotenv.2009.10.027.

Gonzales-Morales, C., Fernandez, B., Molina, F. J., Naranjo-Fernandez, D., Matamoros-Veloza, A. & Camargo-Valero, M. (2021). Influence of pH and temperature on struvite purity and recovery from anaerobic digestate. *Sustainability, 13*(19), 10730. doi:10.3390/su131910730.

Gonzalez-Gil, L., Papa, M., Feretti, D., Ceretti, E., Mazzoleni, G., Steimberg, N., Pedrazzani, R., Bertanza, G., Lema, J. M. & Carballa, M. (2016). Is anaerobic digestion effective for the removal of organic micropollutants and biological activities from sewage sludge? *Water Research, 102*, 211-220. doi:10.1016/j.watres.2016.06.025.

Gracia, J., Mosquera, J., Montenegro, C., Acevedo, P. & Cabeza, I. (2020). Volatile fatty acids production from fermentation of waste activated sludges. *Chemical Engineering Transactions, 79*, 217-222. doi:10.3303/CET2079037.

Grosser, A. & Neczaj, E. (2016). Enhancement of biogas production from sewage sludge by addition of grease trap sludges. *Energy Conversion and Management, 125*, 301-308. doi:10.1016/j.enconman.2016.05.089.

Hwang, J., Zhang, L., Seo, S., Lee, Y. W. & Jahng, D. (2008). Protein recovery from excess sludge for its use as animal feed. *Bioresource Technology, 99*(18), 8949-8954. doi:10.1016/j.biortech.2008.05.001.

Kim, N. K., Mao, N., Lin, R., Bhattacharyya, D., van Loosdrecht, M. C. & Lin Y. (2020). Flame retardant property of flax fabrics coated by extracellular polymeric substances recovered from both activated sludge and aerobic granular sludges. *Water Research, 170*, 115344. doi:10.1016/j.watres.2019.115344.

Kreyenschulte, D., Krull, R. & Margaritis A. (2014). Recent advances in microbial biopolymer production and purification. *Critical Reviews in Biotechnology, 34*(1), 1-15. doi:10.3109/07388551.2012.743501.

Lee, C. G., Alvarez, P. J. J., Kim, H. G., Jeong, S., Lee, S., Lee, K. B., Lee, S. H. & Choi, J. W. (2018). Phosphorous recovery from sewage sludge using

calcium silicate hydrates. *Chemosphere, 193*, 1087-1093, doi:10.1016/j.chemosphere.2017.11.129.

Lin, Y. M., Nierop, K. G. J., Girbal-Neuhauser, E., Adriaanse, M. & van Loosdrecht, M. C. M. (2015) Sustainable polysaccharide-based biomaterial recovered from waste aerobic granular sludge as a surface coating material. *Sustainable Materials and Technologies, 4*, 24-29. doi:10.1016/j.susmat.2015.06.002.

Liu, F., Tian, Y., Ding, Y. & Li, Z. (2016). The use of fermentation liquid of wastewater primary sedimentation sludge as supplemental carbon source for denitrification based on enhanced anaerobic fermentation, *Bioresource Technology, 219*, 6-13. doi:10.1016/j.biortech.2016.07.030.

Liu, H., Wang, J., Liu, X. L., Fu, B., Chen, J. & Yu, H. Q. (2012). Acidogenic fermentation of proteinaceous sewage sludge: Effect of pH. *Water Research, 46*, 799-807. doi:10.1016/j.watres.2011.11.047.

Liu, H., Han, P., Liu, H., Zhou, G., Fu, B. & Zheng, Z. (2018). Full-scale production of VFAs from sewage sludge by anaerobic alkaline fermentation to improve biological nutrients removal in domestic wastewater. *Bioresource Technology, 260*, 105-114. doi:10.1016/j.biortech.2018.03.105.

Liu, Z. & Smith, S. R. (2021). Enzyme recovery from biological wastewater treatment. *Waste and Biomass Valorization*, 12, 4185–4211. doi:10.100 7/s12649-020-01251-7.

Liu, Z. & Smith, S. R. (2020). Enzyme activity of waste activated sludge extracts. *Water Science and Technology, 80*(10), 1861-1869. doi:10.2166/wst.2020.002.

Longo, S., Katsou, E., Malamis, S., Frison, N., Renzi, D. & Fatone, F. (2015). Recovery of volatile fatty acids from fermentation of sewage sludge in municipal wastewater treatment plants. *Bioresource Technology, 175*, 436-444. doi:10.1016/j.biortech.2014.09.107.

Lu, H., Zhang, W., Yang, Y., Huang, X., Wang, S. & Qiu, R. (2012). Relative distribution of Pb2+ sorption mechanisms by sludge-derived biochar. *Water Research, 46*(3), 854-862. doi:10.1016/j.watres.2011.11.058.

Martin, J., Camacho-Muñoz, D., Santos, J.L., Aparicio, I. & Alonso, E. (2012). Occurrence of pharmaceutical compounds in wastewater and sludge from wastewater treatment plants: removal and ecotoxicological impact of wastewater discharges and sludge disposal. *Journal of Hazardous Materials, 239-240*, 40-47. doi:10.1016/j.jhazmat.2012.04.068.

Melo, A. L. A, Soccol, V. T. & Soccol, C. R. (2016). Bacillus thuringiensis: mechanism of action, resistance, and new applications: A review. *Journal: Critical Reviews in Biotechnology, 36*(2), 317-326. doi:10.3109/07388551.2014.960793.

Mengmeng, C., Hong, C., Qingliang, Z., Shirley, S. N. & Jie, R. (2009). Optimal production of polyhydroxyalkanoates (PHA) in activated sludge fed by

volatile fatty acids (VFAs) generated from alkaline excess sludge fermentation, *Bioresource Technology,100*(3), 1399-1405. doi:10.1016/j.biortech.2008.09.014.

Mohammedi, S., Bala Subramanian, S., Yan, S., Tyagi, R. D. & Valéro, J. R. (2006). Molecular screening of Bacillus thuringiensis strains from wastewater sludge for biopesticide production. *Process Biochemistry, 41*(4), 829-835. doi:10.1016/j.procbio.2005.10.023.

Munir, S. & Jamil, N. (2020). Polyhydroxyalkanoate (PHA) production in open mixed cultures using waste activated sludge as biomass. *Archives of Microbiology, 202*, 1907-1913. doi:10.1007/s00203-020-01912-0.

Nabarlatz, D., Stüber, F., Font, J., Fortuny, A., Fabregat, A. & Bengoa, C. (2012). Extraction and purification of hydrolytic enzymes from activated sludge. *Resources Conservation and Recycling, 59*, 9-13. doi:10.1016/j.resconrec.2011.06.017.

Nawaz, M., Mabubu, J. I. & Hua, H. (2016). Current status and advancement of biopesticides: Microbial and botanical pesticides. *Journal of Entomology and Zoology Studies, 4*(2), 241-246.

Otieno, P. C., Nyalala, S. & Wolukau, J. (2019). Suitability of biosolids from university sewage ponds as a substrate for crop production. *African Journal of Agricultural Research, 14*(35), 2062-2074. doi:10.5897/AJAR2019.14231.

Perimenis, A., Nicolay, T., Leclercq, M. & Gerin, P. A. (2018). Comparison of the acidogenic and methanogenic potential of agroindustrial residues. *Waste Management, 72*, 178-185. doi:10.1016/j.wasman.2017.11.033.

Pervaiz, M. & Sain, M. (2011). Protein extraction from secondary sludge of paper mill wastewater and its utilization as a wood adhesive. *BioResources, 6*(2), 961-970.

Phan, H. V., Wickham, J., Xie, S., McDonald, J. A., Khan, S. J. Ngo, H. H. Guo, W. & Nghiem, L. D. (2018). The fate of trace organic contaminants during anaerobic digestion of primary sludge: A pilot scale study. *Bioresource Technology, 256*, 384-390. doi:10.1016/j.biortech.2018.02.040.

Racek, J., Sevcik, J., Chorazy, T., Kucerik J. & Hlavinek P. 2020. Biochar – recovery material from pyrolysis of sewage sludge: A review. *Waste and Biomass Valorization, 11*, 3677-3709. doi:10.1007/s12649-019-00679-w.

Raheem, A., Sikarwar, V. S., He, J., Dastyar, W., Dionysiou, D. D., Wang, W. & Zhao, M. (2018). Opportunities and challenges in sustainable treatment and resource reuse of sewage sludge: A review. *Chemical Engineering Journal, 337*, 616-641. doi: 10.1016/j.cej.2017.12.149.

Reddy, C. S. K., Ghai, R. & Rashmi-Kalia, V. C. (2003). Polyhydroxyalkanoates: An overview. *Bioresource Technology, 87*(2), 137-146. doi:10.1016/S0960-8524(02)00212-2.

Rorat, A., Courtois, P., Vandenbulcke, F., & Lemiere, S. (2019). Sanitary and environmental aspects of sewage sludge management. *Industrial and Municipal Sludge*, 155–180. doi:10.1016/B978-0-12-815907-1.00008-8.

Salehizadeh, H. & Van Loosdrecht, M. C. M. (2004). Production of polyhydroxyalkanoates by mixed culture: Recent trends and biotechnological importance. *Biotechnology Advances, 22*, 261–279. doi:10.1016/j.biotechadv.2003.09.003.

Samara, E., Matsi, T. & Balidakis, A. (2017). Soil application of sewage sludge stabilized with steelmaking slag and its effect on soil properties and wheat growth. *Waste Managementi 68*, 378–387. doi:10.1016/j.wasman.2017.06.016.

Santacoloma-Londono, S., Buitrago-González, M. E, Colorado-Molina, K., Suárez-Pineda, I., Martínez-Martina, M. A., & Villegas-Méndez, L. C. (2020). Agricultural use of biosolids generated in wastewater treatment of a food industry. *Revista Facultad de Ingeniería, 29*(54), e10666. doi:10.19053/01211129.v29.n54.2020.10666.

Semerci, N., Ahadi, S. & Coşgun, S. (2021). Comparison of dried sludge and sludge ash for phosphorus recovery with acidic and alkaline leaching. *Water and Environment Journal, 35*(1), 359-370. doi:10.1111/wej.12633.

Shackley, S., Carter, S., Knowles, T., Middelink, E., Haefele, S., Sohi, S., Cross, A. & Haszeldine, S. (2012). Sustainable gasification-biochar systems? A case-study of rice-husk gasification in Cambodia, Part 1: Context, chemical properties, environmental and health and safety issues. *Energy, 42*, 49-58. doi:10.1016/j.enpol.2011.11.026.

Shen, N. & Zhou, Y. (2016). Enhanced biological phosphorus removal with different carbon sources. *Applied Microbiology and Biotechnology, 100*, 4735-45. doi: 10.1007/s00253-016-7518-4.

Siciliano, A., Limonti, C., Curcio, G. M. & Molinari, R. (2020). Advances in struvite precipitation technologies for nutrients removal and recovery from aqueous waste and wastewater. *Sustainability, 12*, 7538. doi:10.3390/su12187538.

Simoes, F., Colston, R., Rosa-Fernandes, C., Vale, P., Stephenson, T. & Soares A. (2020). Predicting the potential of sludge dewatering liquors to recover nutrients as struvite biominerals. *Environmental Science and Ecotechnology, 3*, 100052. doi:10.1016/j.ese.2020.100052.

Song, X., Shi, Z., Li, X., Wang, X. & Ren, Y. (2019).Fate of proteins of waste activated sludge during thermal alkali pretreatment in terms of sludge protein recovery. *Frontiers of Environmental Science & Engineering, 13*(2), 25. doi:10.1007/s11783-019-1114-7.

Sousa, A. A. T. C. & Figueiredo, C. C. (2016). Sewage sludge biochar: Effects on soil fertility and growth of radish. *Biological Agriculture & Horticulture*

An International Journal for Sustainable Production Systems, 32, 2, 127-138. doi:10.1080/01448765.2015.1093545.

Tanaka, S., Kobayashi, T., Kamiyama, K. & Bildan, M. L. N. S. (1997). Effects of thermochemical pretreatment on the anaerobic digestion of waste activated sludge. *Water Science and Technology, 35*(8): 209–215.

Thangarajan, R., Bolan, N., Mandal, S., Kunhikrishnan, A., Choppala, G., Karunanithi, R. & Qi, F. (2016). Biochar for Inorganic Contaminant Management in Soil. In: Wong, M.H., Ok, Y.S. (eds.) *Biochar: Production, Characterization and Applications*, pp. 46–65. CRC Press Taylor and Francis Group, Boca Raton.

Tian, P., Shang, L., Ren, H., Mi, Y., Fan, D. & Jiang, M. (2009). Biosynthesis of polyhydroxyalkanoates: Current research and development. *African Journal of Biotechnology, 8*, 709–714.

Tong, J. & Chen, Y. (2007). Enhanced biological phosphorus removal driven by short-chain fatty acids produced from waste activated sludge alkaline fermentation. *Environmental Science and Technology*, 41(20), 7126-7130. doi:10.1021/es071002n.

Tyagi, V. K. & Lo, S.L. (2013). Sludge: A waste or renewable source for energy and resources recovery? *Renewable and Sustainable Energy Reviews*, 25, 708–728. doi:10.1016/j.rser.2013.05.029.

Tyagi, R. D., Surampalli, R. Y. & Yan, S. (2009). *Sustainable Sludge Management: Production of Value Added Products*, American Society of Civil Engineers, Reston, VA, USA.

Vaithyanathan, V. K. & Cabana H. (2021). Integrated biotechnology management of biosolids: Sustainable ways to produce value-added products. Frontiers in *Water, 3*,729679. doi: 10.3389/frwa.2021.729679.

van den Oever, M., Molenveld, K., van der Zee, M., & Bos, H. (2017). *Bio-based and biodegradable plastics-Facts and figures: Focus on food packaging in the Netherlands*.Wageningen Food & Biobased Research, No. 1722. doi:10.18174/408350.

Wu, C. Y., Peng, Y. Z., Li, X. L. & Wang, S. Y. (2010). Effect of carbon source on biological nitrogen and phosphorus removal in an anaerobic-anoxic-oxic (A2O) process. *Journal of Environmental Engineering,136*, 1248–54. doi:10.1061/(ASCE)EE.1943-7870.0000262.

Xiao, K. & Zhou, Y. (2020). Protein recovery from sludge: A review. *Journal of Cleaner Production, 249*, 119373. doi:10.1016/j.jclepro.2019.119373.

Xiong, H., Chen, J., Wang, H. & Shi, H. (2012). Influences of volatile solid concentration, temperature and solid retention time for the hydrolysis of waste activated sludge to recover volatile fatty acids. *Bioresource Technology*, 119, 285-292. doi:10.1016/j.biortech.2012.05.126.

Yang, L., He, L., Xue, J., Wu, L., Ma, Y., Li, H., Peng, P., Li, M. & Zhang, Z. (2019). Highly efficient nickel (II) removal by sewage sludge biochar supported α-Fe2O3 and α-FeOOH: Sorption characteristics and mechanisms. *PLoS ONE 14*(6), e0218114. doi:10.1371/journal.pone.0218114.

Yang, C., Zhang, W., Liu, R., Zhang, C., Gong, T., Li, Q., Wang, S. & Song, C. (2013). Analysis of polyhydroxyalkanoate (PHA) synthase gene and PHA-producing bacteria in activated sludge that produces PHA containing 3-hydroxydodecanoate. *FEMS Microbiology Letters, 346*(1), 56–64. doi:10.1111/1574-6968.12201.

Yu, G., He, P., Shao, L. & Zhu, Y. (2009). Enzyme extraction by ultrasound from sludge flocs. *Journal of Environmental Sciences, 21*(2), 204-210. doi:10.1016/S1001-0742(08)62252-4.

Chapter 7

INCREASING CLASSIFICATION ACCURACY THROUGH MAX VOTING METHOD IN IRIS RECOGNITION WITH SUPPORT VECTOR MACHINE AND HAMMING DISTANCE

Hakan TEMİZ[1]

1 Hakan Temiz, Department of Control and Automation Borçka Acarlar Vocational High School, Artvin Coruh University, Borçka, Artvin, 08400, Turkiye, htemiz@artvin.edu.tr, Orcid ID: 0000-0002-1351-7565

1. INTRODUCTION

Today, the need and importance of security has dramatically increased. For this purpose, various biometric methods such as face recognition, gait recognition, posture recognition, and fingerprint recognition are being developed intensively. One of these methods is iris recognition. Iris recognition, based on the principle of uniqueness of iris patterns, are methods and techniques used for automatic recognition of individuals through these patterns (Nguyen, Fookes, Ross, & Sridharan, 2017).

The iris pattern of each eye differs from person to person and from eye to eye (left or right). The statistical uniqueness of iris patterns has made the iris recognition method one of the leading methods in identification methods. It also has a very strong mathematical advantage that its variability between different individuals is very high (J. Daugman, 2009). The iris pattern is formed six months after birth and stabilizes one year later, remaining the same for life. Iris patterns are so unique that they differ from each other even in identical twins. Furthermore, it is nearly not affected by environmental factors. Therefore, the lifetime invariance of the iris has made its use in authentication attractive. In fact, the results are so good that according to one report, more than 1 billion people's iris images have been digitally recorded (Nguyen et al., 2017). The high success rate in iris recognition provides very important clues about how important a role it can play in large-scale identity recognition systems in the future.

The structure and parts of a typical eye are described in Figure 1. The iris is the patterned region consisting of a contractible thin membrane between the transparent layer of the eye and the pupil.

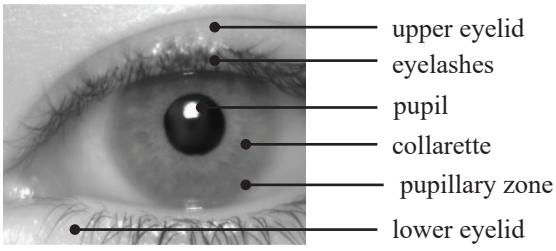

Figure 1 Parts of an eye (Rai & Yadav, 2014)

The first thing to do for identification with the iris image is to detect the iris region and extract this information from the digital image. After the iris region is determined, there is a need to purify the noises on this area. The upper and lower eyelids covering the iris region, the upper and lower

eyelashes that cause the same region to be covered, various light and ambient effects can be given as examples of these noises. The next step is to normalize the iris image. With the normalization process, the iris image, which has different sizes, is adjusted to a fixed size due to factors such as the distance at which the image is taken, the differences in size due to the natural structure of the eye, and the convergence / divergence factor in the imaging device. In addition, insufficient factors such as the negative effects of eyelashes covering the iris pattern are minimized. The normalized image is subjected to a series of feature extraction techniques to improve the performance of the classifiers. The final iris information obtained after the feature extraction process is enrolled in a database for later use in the authentication process. During authentication, the iris information of the person to be identified is obtained by going through similar stages up to the feature extraction stage, as explained above. Then, this information is compared with the iris information stored in the database. The goal of the comparison is to identify the person to find out who she/he is, as a result of authentication.

In this study, identification was performed using support vector machine classifier based on Hamming distance in authentication with iris information. In order to increase the accuracy of the classifier, the max voting method was used. With the max voting method, the identity information obtained from the sample iris image of an individual whose identity is being tried to be verified is compared with the information obtained from sample images of the individuals registered in the database before. Afterwards, the identity found with the highest number of voting among the predictions obtained as a result of all comparisons is determined as the right identity. With the max voting method, the classifier performance, which is normally 79.51% at highest, has been increased up to 94.26% classification accuracy.

This study is organized as follows. In the second part, information on the proposed and applied methods in iris-based identification, as well as information for commonly used datasets are given briefly. In the third chapter, the method applied in this study and the findings from the experiments are explained in detail. In the fourth chapter, a brief information about this study and its results is given and some opinions on various issues related to iris recognition are discussed.

2. RELATED WORKS

Various studies on iris pattern-based authentication have been carried out for years. One of them is Daugman (J. Daugman, 2004). Daugman proposed a method for detecting the limbic border and pupillary border. After the determination of the iris region, the iris image was transformed into a Cartesian coordinate system, thanks to a dimensionless pseudo-

coordinate system. Feature extraction was performed using a two-dimensional (2D) complex Gabor filter. He used the Hamming distance in the matching phase for identification. The authors also proposed other methods such as discrete cosine transform (DCT) (Monro, Rakshit, & Zhang, 2007) and discrete Fourier transform (DFT) (Miyazawa, Ito, Aoki, Kobayashi, & Nakajima, 2008). Masek (Masek & others, 2003) segmented the iris using the intelligent edge recognition technique and the Hough transform. Dewangan and Siddhiqui (kumar Dewangan & Siddhiqui, 2012) used a one-dimensional (1D) Gabor filter for feature extraction and matched it with the Hamming distance. For defining iris pattern, many other methods introducing some type of coding and expansions scheme have been proposed such as sparse coding (Pillai, Patel, Chellappa, & Ratha, 2011), hierarchical visual code block (Sun, Zhang, Tan, & Wang, 2013), and Taylor expansion (Bastys, Kranauskas, & Krüger, 2011) (Bastys, Kranauskas, & Masiulis, 2009).

Deep learning (DL) algorithms have performed considerably better than other algorithms in object recognition, pattern recognition, computer vision, medical image processing and many other research problems. Researchers have achieved very successful results by taking advantage of the superior performance of DL algorithms in iris pattern recognition, as well. One of the most well-known DL algorithms is the convolutional neural networks (CNNs). CNNs are algorithms that have a structure that includes many convolution filters in their layers. In CNNs, each layer transmits its output to the next layer, and as a result of processing the data in each layer, from the input of the network to the last layer that produces the output, output is produced depending on the problem it is adapted to. As a result of the superior performance (learning) of CNNs, they have been adapted as an alternative feature extractor in many problems. On the other hand, the fact that DL algorithms can produce good results with rich data and the scarcity of samples in iris recognition data sets stand out as a limiting factor in the use of DL algorithms (Nguyen et al., 2017). However, it is clear that DL algorithms will perform much more successfully in parallel with the enrichment of data sets.

In order to evaluate the performance of DL algorithms in iris pattern recognition, Nguyen et al. (Nguyen et al., 2017) made comparisons on algorithms with well-known DL models. In the study, the CNNs were especially emphasized. For this purpose, AlexNet (Krizhevsky, Sutskever, & Geoffrey E., 2012), which is the model that won the ILSVRC 2012 competition; GoogleNet and Inception (Szegedy et al., 2015) winner model of the ILSVRC 2014 competition, and the runner-up model VGG-19 (Simonyan & Zisserman, 2014); ResNet (He, Zhang, Ren, & Sun, n.d.) which is the winner the ILSVRC 2015 competition, and DenseNet (Huang, Liu, Van Der Maaten, & Weinberger, 2017), which

has a densely connected blocks structure, were included in the comparison.

Transfer learning refers to the training of DL models trained in a particular domain to be retrained with versions trained in another problem domain. The authors retrained the aforementioned models on iris recognition with the transfer learning method. The performances of the algorithms were tested on the ND-CrossSensor-Iris-2013 (Bowyer & Flynn, 2016) dataset and the CASIA-Iris-Thousand ("CASIA Image database," n.d.) dataset. The authors found that the transfer learning of prominent models is very promising.

In recent years, many other CNNs have been proposed for the iris recognition problem. DeepIris (Liu, Zhang, Li, Sun, & Tan, 2016) which has nine layers, is one of them. Gangwar and Joshi proposed a much more advanced model, DeepIrisNet (Gangwar & Joshi, 2016). The researchers tested the models on both iris images taken with optical light and iris images taken with near infrared. The DualSANet (Yang, Xu, & Fei, 2021) model is a proposed CNN algorithm for multilevel spatial feature extraction. It has an encoder-decoder structure within itself. Another model with encoder-decoder structure is UniNet (Zhao & Kumar, 2017). UniNet consists of two infrastructures: FeatNet and MaskNet. While FeatNet extracts the features of the iris region with its encoder-decoder structure; MaskNet extracts its features from the region outside the iris pattern.

In addition to these, recent developments in video recording technology have made it possible to capture very high resolution iris images in the visible spectrum using low cost camera technologies that can be used for identification within the same domain or in different spectra (such as optical or infrared). However, most large-scale galleries of iris images were obtained in the lower resolution near-infrared (NIR) area. Therefore, cross-spectral and cross-resolution iris matching is one of the important issues that have been emphasized in recent years (Wang & Kumar, 2019), (Nalla & Kumar, 2016).

Generative Adversarial Networks (GANs) (Goodfellow et al., 2020) are among the DL algorithms that often perform better than CNNs. He has achieved remarkable successes especially in image processing and computer vision. The GANs also have been used in iris recognition in the recent years and it has been observed that they had produced very good results as it applies to other research areas. Mostofa et al. (Mostofa, Mohamadi, Dawson, & Nasrabadi, 2021) produced cGAN with conditional URA and cpGAN with paired URA, inspired by DCGAN, a well-known URA model (Radford, Metz, & Chintala, 2016).

2.1. Datasets

Many databases have been created over time to be used in iris recognition. The first of these is the CASIA ("CASIA Image database," n.d.) dataset. This dataset was developed over time and presented to researchers again under the name of different versions. Its latest version, CASIA-IirisV4, was created in 2010. The UBIRIS.v2 (Proenca, Filipe, Santos, Oliveira, & Alexandre, 2010) dataset is another one built on the study of iris recognition from a distance. UTIRIS (University of Tehran Iris Image Repository, n.d.) is another dataset developed by the University of Tehran. The dataset has 10 iris images of 79 individuals, 5 for each eye. The Q-FIRE (Johnson, Lopez-Meyer, Sazonova, Hua, & Schuckers, 2010) dataset contains videos of the face and iris obtained at distances ranging from approximately 1.5m to 7.5m. The ND-IRIS-0405 (Bowyer & Flynn, 2016) and ND-CrossSensor-Iris-2013 (Bowyer & Flynn, 2016) datasets are other datasets composed by the University of Notre Dame Computer Vision Lab. ND-Iris-Template-Aging-2008-2010, Multiple Biometric Grand Challenge (MBGC) version 1 data collection, ND-TimeLapseIris-2012, ND-CrossSensor-Iris-2012 Data Set, ND-CrossSensor-Iris-2013. This laboratory also has many other datasets such as NDIris3D, Notre Dame Photometric Stereo Iris Dataset (Wacv 2019), ND Cosmetic Contact Lenses 2013 Data Set, and The Gender from Iris Dataset (ND-GFI). Apart from the general datasets mentioned, there are hundreds of other datasets. For more detailed information on other datasets, the article by Omelina et al. (Omelina, Goga, Pavlovicova, Oravec, & Jansen, 2021).

3. METOD

The iris recognition process generally consists of iris region detection, normalization, feature extraction and matching stages. In this study, firstly, the iris region was extracted from the digital image. For this purpose, the zigzag area is isolated (segmentation) from other parts of the eye through the Hough transform, and then eyelid detection and eyelash detection is performed. After these treatments, the image of the iris region is sampled and normalized for further processes such as feature extraction. Extracted features are then stored in a database for future use in identification of individuals based on iris pattern. The iris pattern information obtained from extracted features and collected in the database for authentication is compared with the iris pattern information of the eye of the person being identified. If a match is found, the identity is authenticated, otherwise rejected. The operation of the system is presented in

Figure 2.

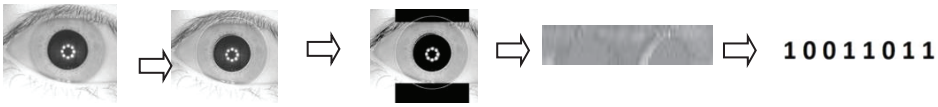

Iris image *segmentation* *eyelid detection* *normalization*

a. Enrollment

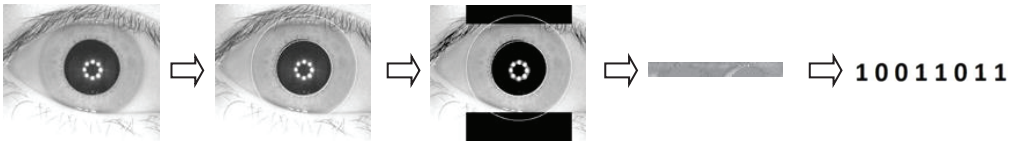

Iris image *segmentation* *eyelid detection* *normalization*

b. Identification

Figure 2 Iris recognition method flowchart *(Rai & Yadav, 2014)*

Image quality is very important in the segmentation phase. Conditions such as insufficient illumination, light reflections on the eye, insufficient contrast, etc., affect the algorithms' performance in determination of the pupil and zigzag area. As these conditions worsen, the performance of iris identification degrades. Thanks to the fact that the images in the CASIA ("CASIA Image database," n.d.) database were successfully acquired, there are no problems such as low contrast and light reflection. For this reason, iris region partitioning can be performed very successfully. On the other hand, the same cannot be said for the images in the UTIRIS (University of Tehran Iris Image Repository, n.d.) database. Segmentation cannot be done properly due to inadequate conditions such as reflections on the images and low contrast in some images. One other reason is that the iris images are very dark colored (e.g., dark brown) due to the genetic structure of Iranian people. Most of them have very dark eyes.

The following sections provide information on these processes.

3.1. Iris Region Detection

The first step in iris recognition is the detection of the iris region and the extracting the information from this region. For this purpose, first, the pupil region is found by Hough transform. Then, the zigzag patterned region of the iris region is found, and finally, the eyelashes and eyelid that appear on this region are detected. The execution of these operations is performed after the RGB image is converted to a grayscale image.

3.1.1. Hough Transform

This technique is used to identify simple geometric objects (line, circle, etc.) on the image. The circular Hough transform was used to determine the radius of the iris and pupil, and the points on the circle. The points on the circle with radius r and center $(x_c,\ y_c)$ are found with the help of the following formulas:

$$x = x_c + r * \cos(\theta) \quad (1)$$

$$y = y_c + r * \sin(\theta) \quad (2)$$

The Hough transform is a costly computational method since it exploits all the points in an image. On the other hand, it provides quite successful results in finding the center and radii of the pupil and zigzag area.

Hough transform briefly works like this. The algorithm tries to find out a triplet $(x_c,\ y_c,\ r)$ to describe each circle while angle θ is sweeping the full unit circle of radius r. For simplification of the parametric description of the circle, the radius is kept as limited to a number of radii or a constant. Before applying the Hough transform, any edge detection algorithm is applied to find all edges in the image. For all edge points $(x_i,\ y_i) = 1, 2, \ldots, n$, that found the edge detection algorithm, the Hough transform can be written as

$$H(x_c, y_c, r) = \sum_{i=1}^{n} h(x_i, y_i, x_c, y_c, r) \quad (3)$$

$$h(x_i, y_i, x_c, y_c, r) = f(x) = \begin{cases} 1, & if\ g(x_i, y_i, x_c, y_c, r) = 0 \\ 0, & otherwise \end{cases} \quad (4)$$

where, $g(x_i, y_i, x_c, y_c, r) = \left(x_i^2 - x_c^2\right) + \left(y_i^2 - y_c^2\right) - r^2$. Then, the coordinates $(x_c,\ y_c,$ r) that the highest for H $(x_c,\ y_c,$ r) become the coordinates of the center and radius of the circle.

3.1.2. Detection of Zigzag Pattern Region

The zigzag region of the iris is the main part used for feature extraction. While this part is limited to the pupil from the inside, it is limited to the transparent region of the eye on the outside. In finding the outside contour, the same method used in finding the pupil can be used. In usual, the pupil and this outer contour are very closed to be concentric. A part of this section can be closed with eyelids and eyelashes depending on the eye and eyebrow structure. Therefore, the next step is to find the area covered by the eyelids and eyelashes.

3.1.3. Eyelid Detection

Eyelids prevent a certain part of the zigzag zone from being seen. The area covered by the eyelids is searched within the pupil and zigzag area. The following formula is used to determine the area covered by the eyelashes (Rai & Yadav, 2014):

Width of search = Radius of zigzag area – radius of pupil (5)

In Figure 3, the areas covered by the eyelids are shown as black areas. An area as wide as the diameter of the iris and as high as the distance between the radius of the iris and the radius of the pupil is considered as a noisy region and is indicated by black color. Parabolic Hough transform is applied for detection of eyelids. The outer contour of the actually existing zigzag zone is shown with dashed lines in the figure.

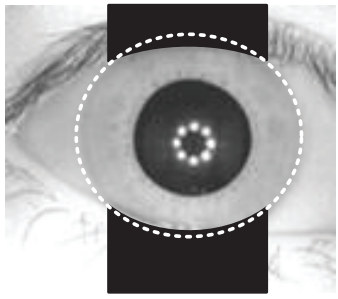

Figure 3. Eyelid detection.

3.2. Normalization

The next step after the iris region is determined and partitioned is to ensure that this region has a fixed size dimensions. For this purpose, methods such as the homogeneous rubber sheet method proposed by Daugman (J. G. Daugman, 1993) are used. This method is depicted in Figure 4. In this method, the data on the points of the iris region on the directions taken at certain angular intervals by taking the center of the

pupil as a reference, are converted into a matrix in the form of rows and columns. The centers of the pupil and iris are not exactly concentric in most cases. The offset of the centers is exaggerated in Figure 4 for clarity.

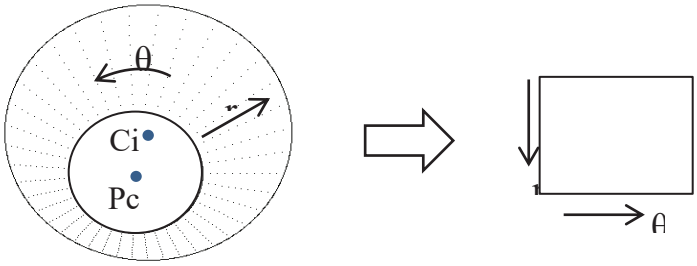

Figure 4. Daugman's Homogeneous Rubber Sheet method. Ci: center of iris, Pc: pupil center.

Figure 5 shows the normalization process of an example iris image. (a) shows the original version of the image. In (b), the radii of the pupil and iris were determined on the image and drawn circularly with white lines. The white dots in the iris region indicate the intervals on the angular directions at certain radii intervals between the pupil and the iris area. The information collected from these points are transformed into row and column matrix in (c). Each row of the matrix stores the information gathered from the points represented as dots on each circle in the iris region.

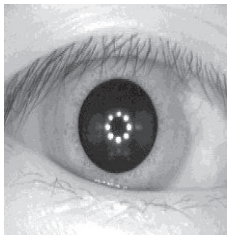

(a) original image

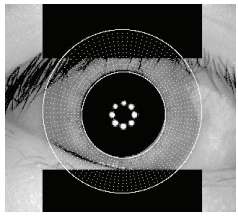

(b) sampling iris pattern with certain angular and radial intervals

(c) sampling matrix of iris region

Figure 5. Normalization in the segmentation phase of a sample iris image

3.3. Eyelash Removal

Typically, the zigzag pattern is likely to be covered by the eyelashes at the top or bottom of the eye. Unfortunately, the pattern information is lost in the closed areas. For this reason, the effect of eyelashes is tried to be eliminated by using pixel information in neighboring sections that are not covered by eyelashes in areas that are likely to be covered by eyelashes. An intensity threshold value is used within a certain window range (for example, 5x5) to determine whether a region is covered by cilia. Values greater than given threshold mean that the area is covered with eyelashes. In this case, the average of the pixels in the selected window neighborhood is assigned to the pixels covered by cilias.

3.4. Feature Extraction and Matching

The main techniques used in feature extraction are image filtering kernels such as Gabor filtering (J. G. Daugman, 1993), random transformation (Zhou & Kumar, 2010), bar operators (Balas & Sinha, 2003), and binary statistical image features (Raja, Raghavendra, & Busch, 2014) methods are used. In this study, 1D Log Gabor wave is used for feature extraction. The data of the circular iris region, which is converted into a matrix in the normalization stage, is subjected to a 1D Log Gabor filter. All rows of the matrix are processed as a one-dimensional signal in the form of a one-dimensional vector. As a result of the operation, a new matrix consisting of zeros and ones is produced. The obtained matrix and training data are recorded in the database. If it is to be used for authentication, e.g., classification, it is matched with images in the database.

For matching, Hamming distance and support vector machine (SVM) classifier are used. The estimation result of the classifier is matched with each training data in the dataset, and the estimation results obtained from these matches are provided to find the most probable result with the max voting method.

3.5. Dataset

The study was performed on the CASIA (“CASIA Image database,” n.d.) image database. A total of 854 images, seven different images of the eyes of 122 different people, were processed from the database. Out of 7 images of each individual, four is used for training, whereas 3 is preserved for testing. In addition to the CASIA database, studies have also been carried out on the Tehran University image database, UTIRIS (University of Tehran Iris Image Repository, n.d.). However, as it is discussed in the following sections, in the experiments, UTIRIS dataset has been found insufficient for iris recognition.

Only the individuals with at least seven different iris images in the CASIA dataset were chosen. The naming structure of the images in the CASIA database is given in Figure 6. The first four images of each 122 individuals in total, were used as training data and the remaining three images were used as the test data for testing purposes.

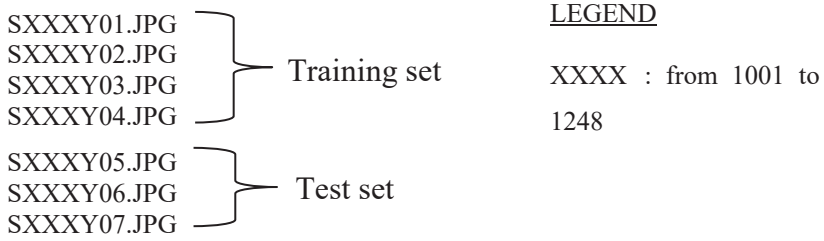

Figure 6. Naming style of images in CASIA database and their separation as training and test sets

3.6. Support Vector Machine

SVMs are one of most prominent machine learning algorithms. It is a data driven method for solving classification problems. It has already been shown to yield lower prediction error compared to classifiers based on other methods, especially given the large number of features for sample identification (Byvatov & Schneider, 2003). An SVM tries to find a hypothetical hyperplane that separating the classes as best as possible. A simple illustration for an SVM is shown in Figure 7.

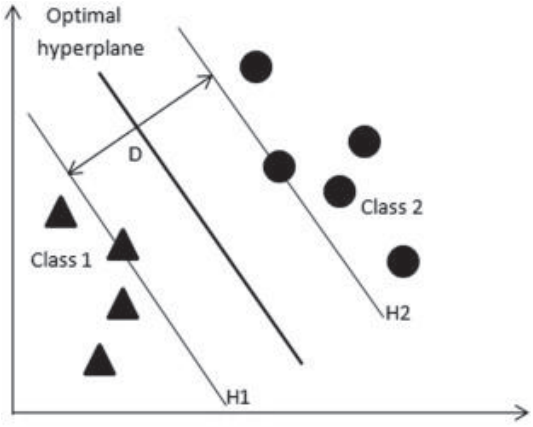

Figure 7. An illustration for an SVM classifier (Meyer, Leisch, & Hornik, 2003)

However, Ali et al. (Ali, Salami, & others, 2008) emphasized that the SVMs have excellent accuracy in terms of non-false acceptance rate, whereas good in terms of non-false rejection.

3.7. Findings

In this study, Hamming distance was used for computing the distances between iris samples during the classification. Classification is done with SVM. 1B Gabor filter is used for feature extraction. The SVM classifier is exploited to determine to which individual each test image belongs to. For this purpose, each image in the test set (last three image of each individual) is compared to each image in the training set (first four images of each individual). The first two and the last two results of comparison are given in Table 1 with detailed summary information. Entire findings can be seen from the Appendix.

Each sub column in the middle column of the table represents a prediction the classifier from the process of benchmarking for a particular matching of certain test image with certain training image. The comparisons are done across every individuals for a particular match of test image and training image (e.g., image no 5 from test set and image no 1 from training set). Each row belongs to an individual, and represents the prediction results obtained by comparing the images of that individual with the images of the remaining individuals. If the SVM classifier correctly identifies the individual (true positive), a check mark is placed. Otherwise, the sample number of falsely predicted individual (false positive) is written. For example, the classifier correctly identified the individual with sample number 1 (first row in the table) from the comparison of images “5 vs 1”, “5 vs 2”, “5 vs 4”, “7 vs 2”, and “7 vs 3”. Contrarily, it is identified her or him as the individuals 21, 73, 114, 114, 64, 2, and 2 from the comparisons of images “5 vs 3”, “6 vs 1”, “6 vs 2”, “6 vs 3”, “6 vs 4”, “7 vs 1” and “7 vs 4”, respectively. So, out of 12 comparisons, it identified the individual as individual 1 for 5 times, individual 114 for 2 times, individual 2 for 2 times, and individuals 21, 73 and 64 for 1 times. This fashion of comparison is repeated for all individuals.

According to the max voting method, each prediction of the classifier is counted, and the most frequent prediction is considered as the right individual. For example, for the individual 1, the 5 out of 12 predictions indicate that he or she is really the individual 1. In this way, according to max voting algorithm given iris images are assumed to belong to individual 1, which is actually the right individual. This approach is applied to other records (individuals) as well, increasing the prediction accuracy of the classifier.

Table 1. Comparison results of the individual benchmarking and the max voting. Only the first and the last two records are given. Please, refer to the Appendix for whole results.

Individuals	Estimated Individuals in Benchmarks (Numbers 1 to 4 indicate the training images, whereas 5 to 7 indicate test images)												Proposed Method
	5 vs 1	5 vs 2	5 vs 3	5 vs 4	6 vs 1	6 vs 2	6 vs 3	6 vs 4	7 vs 1	7 vs 2	7 vs 3	7 vs 4	
1	✓	✓	21	✓	73	114	114	64	2	✓	✓	2	✓
2	✓	✓	32	✓	94	18	18	✓	35	75	86	58	✓
...	...	...	...	...	...	...	...	...	...	...	...	...	...
...	...	...	...	...	...	...	...	...	...	...	...	...	...
121	104	17	✓	35	86	114	114	79	✓	114	114	✓	121, 114
122	✓	✓	✓	✓	✓	35	✓	✓	✓	✓	✓	✓	✓
Number of Corrects	83	79	88	97	72	69	83	86	75	83	79	88	**115**
Accuracy (%)	68.03	64.75	72.13	79.51	59.02	56.56	68.03	70.49	61.48	68.03	64.75	72.13	**94.26**

At the bottom of the table, the total correct number of identification (false positive) and accuracy in percent for each comparison are given. The lowest number of correct identification is 69 (56.56% accuracy), obtained for the column "6 vs 2", whereas the highest number of accuracy, 97 (79.51% accuracy), is obtained for the column "5 vs 4". The results of the proposed method are shown in a separate column on the right most column of the table. The proposed method classifies each sample by taking into account the most repeated number of the individuals amongst 12 comparisons. The 115 out of 122 samples are correctly identified by the proposed max voting method. However, the remaining 7 samples are not clearly identified as the truth individuals. The proposed method could not determine the correct result for Samples 17, 27, 38, 43, 77, 95 and 121.

There is uncertainty in determining individuals for samples 38, 43, 95, and 121 since they are found as the candidate individual for the same number of times. For example, in the identification of individual 38, the classifier predicted it as individuals 34, 38, and 107 for two times and as some of others for ones in the remaining comparisons. Each of these three individuals share the equal probability to be chosen as correct individual, even though the correct value is 38. In such cases, every most predicted individual with equal number of prediction is written in the table together with the others (e.g., max voting results for individual 121). If we consider the four of this uncertain (with equal number of repeated prediction) cases as correct identification, the accuracy in percent could

be assumed as to rise up to 97.54%. Worst cases are happened to individuals with numbers 17, 27 and 77. Apart from these extreme cases, all other individuals were determined correctly. The number of iris images correctly classified increased to 115, which indicates the 94.26% of accuracy, by introducing the max voting method.

4. DISCUSSION AND CONCLUSION

In this study, max voting approach is applied to outcomes of SVM classifier introducing hamming distance for computing distances between samples in order to identify individuals based on iris pattern recognition. Iris recognition is one of popular applications in identifying identity because the pattern of the iris differs from person to person and is unique. The zigzag region of the iris is selected for feature extraction. Pupil and iris region were determined by Hough transform method. In addition, regions with eyelids are detected and masked during feature extraction. After the 1D Gabor filter is applied on the obtained features, classification is made with the Hamming distance.

The prediction results of the SVM classifier were obtained by comparing each of the 3 samples in the test data with the 4 samples in the training data of CASIA iris database. The most probable candidate of individual is determined by counting the number of predictions. The highest number of predicted individual is considered as the right one. As a results of the matching, a table with 122 rows and 12 columns was formed by comparing all three test data with all four training data.

Various accuracy rates ranging from 56.56% to 79.51% were obtained from the distinct comparisons of iris images across the CASIA dataset. With max voting algorithm in which the highest number of predicted individual is taken as the most right individual, the identification accuracy is increased from 79.51% to 94.26%. However, successful results could not be obtained in the UTIRIS database because the images were not as convenient as in the CASIA database. This shows how important it is for the images to be suitable for processing for iris recognition.

Numerous studies have been conducted in the literature on iris pattern-based identification methods, and as a result of extreme efforts, quite successful results have been achieved. Many various types of algorithms and methods are currently used for this purpose. Despite the successful results achieved, there are still problematic parts. One of them is the formation of bitmaps of images. There is still a huge difference between the human brain's interpretation of the image and the computer's interpretation. Humans can recognize all objects in the image in a very short time and associate them with other objects and events. But for

computers, the situation is much more different than this. Methods to distinguish and comprehend each of the objects in the image, and to associate them with other objects are not yet available or not at the expected level. For example, when we look at Figure 7, we can easily distinguish that it belongs to a human eye, pupil, iris, eyelids, eyelashes, right or left eye. On the other side, it is not yet much possible for computers to make similar decisions and inferences in the way we do.

Correct positioning and sizing of the iris region depends on several factors. Examples of these factors are negative effects such as the contrast value of the picture, light reflection, and insufficient illumination. Although such situations have not been encountered in the CASIA dataset, it is not possible to say the same for the UTIRIS dataset. For example, in Figure 8, the determination of the pupil is given in a sample image taken from the UTIRIS database. As can be seen, due to the bright spot inside the pupil, the pupil circumference could not be accurately determined. According to the contour line found, the lower right part of the pupil was correctly detected, but the upper left part was detected incorrectly.

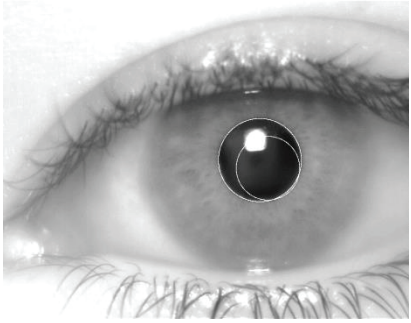

Figure 8. An example of misdetection of the pupil in an image in the UTIRIS database

Similarly, false segmentation and detection problems arises for almost all images in the UTIRIS database. On the other hand, the availability of the CASIA database ensures successful results. The CASIA database is one of well-tailored databases for iris recognition. Therefore, it is very suitable to achieve successful results. In practice, however, it is not always easy to create purposeful data. As can be seen from UTIRIS dataset, many factors affecting the image acquisition process should be considered in order to perform iris recognition in a healthy and accurate manner, and thus, iris images should be taken in this direction. The type of eye, e.g., iris region with very dark color, directly affecting the performance of iris recognition task. Thus, more adaptive techniques

should be developed for such circumstances. One of good candidate for such techniques is to obtain near infrared images for exceptional conditions of eyes.

REFERENCES

Ali, H., Salami, M. J. E., & others. (2008). Iris recognition system by using support vector machines. In *2008 International Conference on Computer and Communication Engineering* (pp. 516–521).

Balas, B. J., & Sinha, P. (2003). STICKS: Image-representation via non-local comparisons. *Journal of Vision*, *3*(9), 12.

Bastys, A., Kranauskas, J., & Krüger, V. (2011). Iris recognition by fusing different representations of multi-scale Taylor expansion. *Computer Vision and Image Understanding*, *115*(6), 804–816.

Bastys, A., Kranauskas, J., & Masiulis, R. (2009). Iris recognition by local extremum points of multiscale Taylor expansion. *Pattern Recognition*, *42*(9), 1869–1877.

Bowyer, K. W., & Flynn, P. J. (2016). The ND-IRIS-0405 iris image dataset. *ArXiv Preprint ArXiv:1606.04853*.

Byvatov, E., & Schneider, G. (2003). Support vector machine applications in bioinformatics. *Applied Bioinformatics*, *2*(2), 67—77. Retrieved from http://europepmc.org/abstract/MED/15130823

CASIA Image database. (n.d.). Retrieved from http://www.cbsr.ia.ac.cn/english/IrisDatabase.asp

Daugman, J. (2004). How Iris Recognition Works. *IEEE Transactions on Circuits and Systems for Video Technology*, *14*(1). https://doi.org/10.1109/TCSVT.2003.818350

Daugman, J. (2009). How iris recognition works. In *The essential guide to image processing* (pp. 715–739). Elsevier.

Daugman, J. G. (1993). High confidence visual recognition of persons by a test of statistical independence. *IEEE Transactions on Pattern Analysis and Machine Intelligence*, *15*(11), 1148–1161. https://doi.org/10.1109/34.244676

Gangwar, A., & Joshi, A. (2016). DeepIrisNet: Deep iris representation with applications in iris recognition and cross-sensor iris recognition. In *2016 IEEE international conference on image processing (ICIP)* (pp. 2301–2305).

Goodfellow, I., Pouget-Abadie, J., Mirza, M., Xu, B., Warde-Farley, D., Ozair, S., … Bengio, Y. (2020). Generative adversarial networks. *Communications of the ACM*, *63*(11), 139–144.

He, K., Zhang, X., Ren, S., & Sun, J. (n.d.). *Deep Residual Learning for Image*

Recognition. Retrieved from http://image-net.org/challenges/LSVRC/2015/

Huang, G., Liu, Z., Van Der Maaten, L., & Weinberger, K. Q. (2017). Densely connected convolutional networks. In *Proceedings of the IEEE conference on computer vision and pattern recognition* (pp. 4700–4708).

Johnson, P. A., Lopez-Meyer, P., Sazonova, N., Hua, F., & Schuckers, S. (2010). Quality in face and iris research ensemble (Q-FIRE). In *2010 Fourth IEEE International Conference on Biometrics: Theory, Applications and Systems (BTAS)* (pp. 1–6). https://doi.org/10.1109/BTAS.2010.5634513

Krizhevsky, A., Sutskever, I., & Geoffrey E., H. (2012). ImageNet Classification with Deep Convolutional Neural Networks. *Advances in Neural Information Processing Systems 25 (NIPS2012)*, 1–9. https://doi.org/10.1109/5.726791

kumar Dewangan, A., & Siddhiqui, M. A. (2012). Human identification and verification using iris recognition by calculating hamming distance. *International Journal of Soft Computing and Engineering(IJSCE)*, *2*(2).

Liu, N., Zhang, M., Li, H., Sun, Z., & Tan, T. (2016). DeepIris: Learning pairwise filter bank for heterogeneous iris verification. *Pattern Recognition Letters*, *82*, 154–161.

Masek, L., & others. (2003). *Recognition of human iris patterns for biometric identification*. Citeseer.

Meyer, D., Leisch, F., & Hornik, K. (2003). The support vector machine under test. *Neurocomputing*, *55*(1), 169–186. https://doi.org/https://doi.org/10.1016/S0925-2312(03)00431-4

Miyazawa, K., Ito, K., Aoki, T., Kobayashi, K., & Nakajima, H. (2008). An effective approach for iris recognition using phase-based image matching. *IEEE Transactions on Pattern Analysis and Machine Intelligence*, *30*(10), 1741–1756.

Monro, D. M., Rakshit, S., & Zhang, D. (2007). DCT-based iris recognition. *IEEE Transactions on Pattern Analysis and Machine Intelligence*, *29*(4), 586–595.

Mostofa, M., Mohamadi, S., Dawson, J., & Nasrabadi, N. M. (2021). Deep GAN-Based Cross-Spectral Cross-Resolution Iris Recognition. *IEEE Transactions on Biometrics, Behavior, and Identity Science*, *3*(4), 443–463. https://doi.org/10.1109/TBIOM.2021.3102736

Nalla, P. R., & Kumar, A. (2016). Toward more accurate iris recognition using cross-spectral matching. *IEEE Transactions on Image Processing*, *26*(1), 208–221.

Nguyen, K., Fookes, C., Ross, A., & Sridharan, S. (2017). Iris Recognition with Off-the-Shelf CNN Features: A Deep Learning Perspective. *IEEE Access*, *6*. https://doi.org/10.1109/ACCESS.2017.2784352

Omelina, L., Goga, J., Pavlovicova, J., Oravec, M., & Jansen, B. (2021). A survey of iris datasets. *Image and Vision Computing*, *108*, 104109.

https://doi.org/https://doi.org/10.1016/j.imavis.2021.104109

Pillai, J. K., Patel, V. M., Chellappa, R., & Ratha, N. K. (2011). Secure and robust iris recognition using random projections and sparse representations. *IEEE Transactions on Pattern Analysis and Machine Intelligence*, *33*(9), 1877–1893.

Proenca, H., Filipe, S., Santos, R., Oliveira, J., & Alexandre, L. A. (2010). The {UBIRIS.v2}: A Database of Visible Wavelength Images Captured On-The-Move and At-A-Distance. *IEEE Trans. PAMI*, *32*(8), 1529–1535. https://doi.org/10.1109/TPAMI.2009.66

Radford, A., Metz, L., & Chintala, S. (2016). Unsupervised representation learning with deep convolutional generative adversarial networks. In *4th International Conference on Learning Representations, ICLR 2016 - Conference Track Proceedings*. Retrieved from https://arxiv.org/pdf/1511.06434.pdf%C3

Rai, H., & Yadav, A. (2014). Iris recognition using combined support vector machine and Hamming distance approach. *Expert Systems with Applications*, *41*(2), 588–593. https://doi.org/https://doi.org/10.1016/j.eswa.2013.07.083

Raja, K. B., Raghavendra, R., & Busch, C. (2014). Binarized statistical features for improved iris and periocular recognition in visible spectrum. In *2nd International Workshop on Biometrics and Forensics* (pp. 1–6).

Simonyan, K., & Zisserman, A. (2014). Very Deep Convolutional Networks for Large-Scale Image Recognition. Retrieved from https://arxiv.org/abs/1409.1556

Sun, Z., Zhang, H., Tan, T., & Wang, J. (2013). Iris image classification based on hierarchical visual codebook. *IEEE Transactions on Pattern Analysis and Machine Intelligence*, *36*(6), 1120–1133.

Szegedy, C., Liu, W., Jia, Y., Sermanet, P., Reed, S., Anguelov, D., … Rabinovich, A. (2015). Going deeper with convolutions. In *Proceedings of the IEEE conference on computer vision and pattern recognition* (pp. 1–9).

University of Tehran Iris Image Repository. (n.d.). UTIRIS. Retrieved from https://utiris.wordpress.com/2014/03/04/university-of-tehran-iris-image-repository/

Wang, K., & Kumar, A. (2019). Cross-spectral iris recognition using CNN and supervised discrete hashing. *Pattern Recognition*, *86*, 85–98.

Yang, K., Xu, Z., & Fei, J. (2021). DualSANet: Dual Spatial Attention Network for Iris Recognition. In *Proceedings of the IEEE/CVF Winter Conference on Applications of Computer Vision* (pp. 889–897).

Zhao, Z., & Kumar, A. (2017). Towards more accurate iris recognition using deeply learned spatially corresponding features. In *Proceedings of the IEEE international conference on computer vision* (pp. 3809–3818).

Zhou, Y., & Kumar, A. (2010). Personal identification from iris images using

localized radon transform. In *2010 20th International Conference on Pattern Recognition* (pp. 2840–2843).

Appendix: Comparison Results

Individuals	Estimated Individuals in Benchmarks (Numbers 1 to 4 indicate the training images, whereas 5 to 7 indicate test images)												Proposed Method
	5 vs 1	5 vs 2	5 vs 3	5 vs 4	6 vs 1	6 vs 2	6 vs 3	6 vs 4	7 vs 1	7 vs 2	7 vs 3	7 vs 4	
1	✓	✓	21	✓	73	114	114	64	2	✓	✓	2	✓
2	✓	✓	32	✓	94	18	18	✓	35	75	86	58	✓
3	✓	✓	52	✓	✓	✓	11	✓	✓	✓	100	✓	✓
4	94	✓	86	58	✓	89	✓	106	✓	89	13	106	✓
5	86	114	✓	64	✓	✓	✓	✓	✓	✓	✓	✓	✓
6	61	✓	✓	✓	✓	✓	✓	106	✓	✓	✓	30	✓
7	✓	55	56	✓	✓	57	25	✓	✓	✓	✓	✓	✓
8	✓	✓	✓	✓	✓	✓	✓	✓	✓	✓	✓	✓	✓
9	13	✓	✓	32	✓	✓	✓	✓	✓	✓	✓	✓	✓
10	✓	✓	✓	✓	✓	✓	✓	✓	✓	✓	✓	✓	✓
11	64	65	✓	✓	115	115	✓	✓	5	✓	111	✓	✓
12	✓	✓	✓	✓	114	103	30	107	2	✓	✓	✓	✓
13	86	✓	70	92	86	✓	✓	35	29	103	✓	107	✓
14	✓	✓	✓	✓	✓	✓	✓	✓	✓	✓	✓	✓	✓
15	105	✓	✓	✓	110	✓	✓	✓	65	122	11	65	✓
16	✓	✓	✓	✓	✓	✓	✓	✓	✓	✓	✓	✓	✓
17	✓	75	1	73	78	18	115	115	64	18	✓	18	18
18	✓	✓	1	✓	✓	✓	1	✓	✓	✓	16	✓	✓
19	✓	✓	✓	✓	✓	✓	✓	✓	✓	✓	✓	✓	✓
20	✓	✓	✓	✓	✓	✓	✓	✓	✓	94	112	114	✓
21	✓	112	✓	✓	✓	112	✓	✓	✓	81	✓	✓	✓
22	✓	67	✓	✓	✓	95	✓	✓	111	32	26	36	✓
23	✓	✓	✓	✓	✓	✓	✓	✓	✓	✓	✓	✓	✓
24	✓	✓	✓	✓	48	✓	✓	✓	85	42	30	106	✓
25	57	✓	✓	✓	✓	91	22	30	35	✓	6	30	✓
26	✓	76	✓	✓	✓	30	✓	30	✓	✓	✓	✓	✓
27	121	114	13	43	61	43	43	43	6	42	35	30	43
28	✓	88	✓	✓	✓	88	✓	✓	✓	✓	✓	✓	✓
29	85	✓	✓	✓	6	✓	✓	✓	✓	✓	64	✓	✓
30	102	42	35	✓	102	42	✓	✓	98	75	✓	107	✓
31	✓	✓	✓	✓	✓	✓	✓	✓	✓	✓	✓	✓	✓
32	✓	✓	✓	✓	✓	✓	✓	✓	✓	✓	✓	✓	✓
33	✓	✓	✓	✓	✓	✓	✓	✓	✓	✓	✓	✓	✓
34	✓	✓	✓	✓	✓	✓	✓	✓	✓	✓	82	82	✓
35	106	✓	✓	✓	✓	42	✓	✓	114	✓	✓	✓	✓
36	✓	✓	✓	✓	✓	✓	✓	✓	✓	✓	✓	✓	✓
37	114	✓	30	84	61	42	✓	22	✓	✓	✓	✓	✓
38	34	✓	34	34	36	57	42	30	✓	107	108	107	34,38,107
39	39	44	✓	✓	✓	6	✓	✓	✓	44	✓	✓	✓
40	✓	95	✓	✓	✓	6	✓	✓	✓	6	✓	✓	✓
41	✓	✓	✓	✓	✓	6	✓	✓	✓	3	✓	✓	✓
42	✓	32	✓	✓	✓	✓	✓	30	✓	✓	✓	✓	✓
43	85	75	✓	✓	85	89	86	58	85	42	✓	59	43,85
44	✓	✓	✓	✓	5	✓	✓	✓	85	✓	✓	✓	✓
45	✓	✓	✓	✓	✓	✓	✓	✓	✓	✓	✓	✓	✓
46	✓	✓	✓	✓	✓	61	✓	✓	35	61	104	30	✓
47	✓	✓	✓	✓	✓	✓	✓	✓	✓	✓	✓	✓	✓
48	✓	✓	✓	✓	102	42	✓	✓	✓	✓	✓	✓	✓
49	✓	6	5	✓	✓	103	30	113	✓	84	93	113	✓

50	✓	✓	✓	✓	40	✓	✓	✓	✓	✓	✓	✓	✓
51	✓	70	✓	✓	48	55	75	75	70	✓	75	✓	✓
52	✓	✓	✓	✓	✓	✓	✓	✓	✓	✓	✓	✓	✓
53	✓	✓	✓	✓	✓	✓	✓	✓	✓	✓	✓	✓	✓
54	✓	1	✓	✓	✓	✓	✓	✓	118	✓	✓	✓	✓
55	13	✓	✓	✓	✓	✓	✓	✓	✓	✓	✓	✓	✓
56	✓	✓	6	✓	67	✓	✓	✓	✓	✓	✓	✓	✓
57	✓	✓	✓	7	✓	✓	25	7	✓	✓	25	117	✓
58	85	42	13	✓	35	75	35	✓	62	67	13	✓	✓
59	86	✓	✓	✓	✓	✓	✓	✓	97	✓	✓	✓	✓
60	✓	✓	✓	✓	✓	✓	✓	✓	✓	✓	✓	✓	✓
61	✓	✓	✓	30	✓	✓	✓	✓	✓	✓	✓	✓	✓
62	✓	67	61	✓	88	61	✓	✓	✓	✓	✓	✓	✓
63	118	88	✓	✓	6	✓	✓	90	118	44	32	44	✓
64	✓	✓	✓	✓	16	43	✓	✓	✓	✓	69	✓	✓
65	✓	✓	✓	✓	✓	✓	✓	✓	✓	✓	✓	✓	✓
66	✓	33	✓	✓	✓	✓	✓	✓	✓	✓	✓	✓	✓

Appendix: Comparison Results (Continue)

Individuals	Estimated Individuals in Benchmarks (Numbers 1 to 4 indicate the training images, whereas 5 to 7 indicate test images)												Proposed Method
	5 vs 1	5 vs 2	5 vs 3	5 vs 4	6 vs 1	6 vs 2	6 vs 3	6 vs 4	7 vs 1	7 vs 2	7 vs 3	7 vs 4	
67	✓	✓	✓	✓	69	36	✓	95	✓	✓	✓	✓	✓
68	4	67	✓	32	29	✓	✓	35	4	13	✓	48	✓
69	✓	✓	✓	✓	✓	✓	✓	✓	✓	✓	✓	✓	✓
70	25	✓	✓	✓	✓	✓	18	✓	98	84	✓	✓	✓
71	✓	✓	✓	✓	✓	✓	✓	✓	31	94	✓	✓	✓
72	✓	✓	✓	✓	✓	✓	✓	✓	✓	79	✓	✓	✓
73	✓	✓	✓	✓	✓	61	✓	75	✓	✓	94	✓	✓
74	✓	✓	70	51	45	45	✓	✓	✓	✓	✓	✓	✓
75	✓	62	✓	✓	✓	25	✓	✓	73	✓	22	✓	✓
76	✓	✓	39	42	✓	✓	✓	56	102	✓	✓	✓	✓
77	118	71	✓	101	91	24	45	85	6	✓	91	91	91
78	✓	✓	✓	✓	116	✓	✓	✓	✓	✓	✓	✓	✓
79	✓	✓	92	✓	121	43	114	✓	116	95	80	✓	✓
80	86	✓	✓	✓	✓	✓	66	✓	60	✓	69	51	✓
81	✓	✓	✓	✓	✓	✓	✓	✓	11	✓	✓	✓	✓
82	✓	✓	✓	✓	✓	✓	✓	✓	✓	✓	✓	✓	✓
83	✓	✓	✓	✓	49	103	18	107	✓	5	✓	✓	✓
84	61	✓	✓	✓	✓	✓	✓	✓	102	✓	✓	✓	✓
85	31	84	84	✓	58	✓	3	68	58	✓	30	68	✓
86	62	✓	61	✓	62	✓	70	✓	✓	95	39	✓	✓
87	✓	✓	45	✓	85	5	24	✓	✓	✓	74	74	✓
88	✓	✓	✓	✓	✓	8	✓	✓	✓	✓	✓	✓	✓
89	85	84	25	30	38	109	70	✓	✓	✓	13	106	✓
90	✓	✓	✓	✓	118	✓	✓	✓	118	✓	✓	✓	✓
91	✓	✓	✓	✓	✓	84	✓	✓	✓	75	✓	✓	✓
92	81	✓	✓	✓	✓	✓	✓	✓	26	✓	✓	✓	✓
93	✓	6	80	✓	✓	84	22	30	61	95	39	30	✓
94	✓	45	39	✓	✓	✓	✓	✓	✓	✓	✓	✓	✓
95	17	5	5	5	20	1	34	1	48	✓	48	94	5,1
96	✓	✓	✓	✓	✓	✓	✓	✓	✓	✓	✓	✓	✓

97	✓	9	13	✓	✓	95	13	100	✓	35	103	43	✓
98	✓	75	115	49	31	✓	114	49	9	✓	45	9	✓
99	✓	✓	✓	✓	✓	✓	✓	✓	20	✓	99	✓	✓
100	85	103	13	107	✓	✓	✓	✓	85	103	13	107	✓
101	✓	✓	✓	✓	✓	114	✓	✓	101	4	✓	✓	✓
102	✓	✓	109	✓	109	✓	✓	✓	✓	49	109	✓	✓
103	✓	4	✓	✓	114	118	93	43	✓	30	✓	✓	✓
104	✓	84	✓	✓	86	✓	13	✓	86	✓	13	✓	✓
105	114	43	18	✓	6	94	103	✓	57	✓	73	25	✓
106	76	✓	✓	56	40	✓	✓	✓	✓	✓	✓	✓	✓
107	52	✓	✓	✓	106	✓	✓	✓	✓	✓	✓	✓	✓
108	✓	✓	69	87	48	53	48	38	116	95	6	✓	✓
109	✓	✓	✓	✓	✓	✓	✓	✓	✓	✓	✓	✓	✓
110	✓	15	✓	✓	60	✓	✓	96	89	✓	✓	✓	✓
111	115	✓	✓	✓	✓	✓	✓	✓	✓	✓	✓	✓	✓
112	✓	✓	✓	103	94	✓	21	✓	✓	✓	✓	✓	✓
113	115	✓	✓	111	✓	19	65	13	96	122	20	122	✓
114	64	91	✓	✓	2	✓	64	✓	119	1	21	✓	✓
115	✓	✓	✓	✓	✓	✓	✓	✓	✓	✓	✓	✓	✓
116	✓	6	6	✓	✓	66	24	✓	✓	✓	✓	✓	✓
117	102	48	✓	102	✓	45	✓	96	✓	✓	✓	✓	✓
118	✓	104	✓	✓	114	✓	93	107	85	89	✓	4	✓
119	✓	40	✓	✓	✓	4	✓	✓	✓	✓	✓	✓	✓
120	114	118	114	99	51	43	64	105	✓	✓	81	✓	✓
121	104	17	✓	35	86	114	114	79	✓	114	114	✓	121,114
122	✓	✓	✓	✓	✓	35	✓	✓	✓	✓	✓	✓	✓
Number of Correct	83	79	88	97	72	69	83	86	75	83	79	88	**115**
Accuracy (%)	68,03	64,75	72,13	79,51	59,02	56,56	68,03	70,49	61,48	68,03	64,75	72,13	**94,26**